Rapid Prototyping Tissue Models of Mammary Duct Epithelium

-Submitted in partial fulfillment of the requirements for the degree of-

Doctor of Philosophy in Biomedical Engineering

Thomas James Hinton
B.S., Biomedical Engineering, Purdue University
M.S., Biomedical Engineering, Carnegie Mellon University

Carnegie Mellon University Pittsburgh PA
April 2017

Copyright Notice

Abstract

Ductal Carcinoma in Situ (DCIS) does not have a clinically useful indicator of malignancy, and it is often benign, except in 20% of cases. Even more important, it has a cure – removal of the affected breast. DCIS patients overwhelmingly elect for invasive therapies to escape that 20% malignant chance. Overtreatment such as this costs the patients, and it highlights the need for a DCIS model capable of distinguishing the 20% in need of treatment. Some labs have taken steps toward three-dimensional, complex, and biomimetic models of mammary tissues using a variety of endogenous and synthetic gels and 3D printing. We developed FRESH (Freeform Reversible Embedding of Suspended Hydrogels) as the first method capable of 3D printing highly biomimetic shapes from endogenous gels. Utilizing FRESH, we aim to rapid prototype models of mammary duct epithelia that are biomimetic, parametric, and capable of iterative evolution. First, we investigate the principles of 3D printers modified for extruding fluids and construct a comprehensive hardware and software platform for printing gelling fluids. Second, we apply the FRESH method to 3D print collagen and alginate hydrogels, demonstrating patency of printed vascular models, topological fidelity, and the synergistic combination of hydrogel properties in multi-material prints. Finally, we rapid prototype an epithelial monolayer by seeding a 3D printed collagen manifold, and we demonstrate maintenance of the tissue's geometry across a week of culture. We provide evidence of fidelity in prints such as an epithelial tree printed at 200% scale using unmodified collagen type I, and we investigate the combination of hydrogel properties in multi-material prints by utilizing a second hydrogel (alginate) to reinforce and preserve the fidelity of this collagen tree during handling. Our approach utilizes faster (>40 mm/s), cheaper (<$2000) hardware, and it is capable of greater geometric freedom than previously established

approaches which are hindered by “overhangs”. Additionally, we demonstrate superior, 99.7% printed cell viability and material compatibility (collagen, fibrin, alginate, and Matrigel®). It is hoped that this work will enable researchers to inexpensively rapid prototype endogenous hydrogels; furthermore, through the efforts of these individuals, we hope our impact will hasten the pace of tissue engineering.

Dedication

Prarthana

You kept my head on straight. I could not have done it without you. Time and time again, I'd fret over the smallest aspects of grad student life, and you were there to highlight the reality of the situation. In no small way was I constantly amazed by the sharpness of your mind. I get that I was there for your too, but, were it not for your part, I wouldn't be as far along in life as I am. Please don't forget the transformative effect you've had on me. Sometimes yellow. Monoclinic and often gemmy. Similar to beryl. Got that one? How about opaque pink, tetrahedral, rarely lustrous.

Mom & Dad

Obviously, I owe my heartbeat to you guys. There couldn't be a kinder set of parents known. You guys saw me through all the roughest points in my life, and now I'm super lucky to look back and know you're proud. Not to mention the stellar role models you make… I know I've been dense and downright "skippy" at times, but you were there for me where I needed it most. Clichés aside, I love you guys.

Eric Hsu

You're the kindest person I know, and you're a model golden soul. Your friendship made my first few years in Pittsburgh infinitely more fun. Obviously, there's a lot more I could say here, but you should just ask me to come to wherever you are if/when you read this and share a pitcher. Then we can catch up.

Adam Feinberg

This tissue engineering thing is genuinely bigger than any one of us, and I think it's your keen understanding of significance, cause, and effect that I find so admirable. I hope to continue receiving your wisdom far into the future. Perhaps we will someday have a massive, positive impact on the world.

John, Quentin, Pedro, Arun, Eric, and April

MOST of my laughter from 2012 until 2016 was due to you guys. I can honestly say the synergy between all of you was the best I've witnessed. From John's "questioning" his uhm… personal values to Quentin's sheetstorms. From Arun's bl-bl-blood to Pedro's trouble digesting fiber and personal value as Arun's bunkmate. Let us not forget Katy Perry's contributions to Eric's wellbeing or April's kind wishes toward all stupid people. All of this is to say I wouldn't have felt a sense of belonging without you guys. The humor was magnificent, but that was just a plus. The genuinely wonderful nature of each of you was the main reward.

Steph

Our shared visions have never stopped illuminating my path forward. Thank you for the continuing inspiration and kinship. Thank you for teaching me to perceive the beauty in transient coincidence, for I would not thrive in the desert of research without it.

Hudson

Just checkin' in on ya. How are ya? There's a lot to be learned from someone as full of opinion and sheer "relevance" as you. Thanks to all that, I've found mundane happenstance to be full of irony and humor. Who knew making inconvenient mountains from molehills could be so fun? It's impossible to speak without hearing a miniature Burr critique my every word. So, to honor our shared aspirations, some wisdom from ole Billy Red-Face: "Realize that sleeping on a

futon when you're 30 is not the worst thing. You know what's worse, sleeping in a king bed next to a wife you're not really in love with but for some reason you got married, and you got a couple of kids, and you got a job you hate. You'll be laying there fantasizing about sleeping on a futon. There's no risk when you go after a dream. There's a tremendous amount of risk to playing it safe."

Lee

You're the only person I've met in bioprinting that gets the idea of "bioarchitecture". I really value this, and I hope you continue to pursue it. What this has meant to me is that I'm not alone in finding this stuff meaningful. If I'm lucky, we can continue to work on this together.

Finger

Fingaling, you're maybe the smartest dude I know. Thankfully,you're a good person who's not as funny as he thinks but then has me laughing anyway, right Luyan? Thank you for sharing your wisdom(and gripes) on getting a Ph.D., whether or not you know it. Thank you for sharing your passion for existence. I absolutely love the discussions of topology, computing, metaphysics, pop-science, quantum physics, rocketry, and Zelda; furthermore, they have proven to be priceless modifiers in my engineering heuristics. I think I have been a much better innovator with a ghostly working knowledge of all those topics. Karsai was extremely lucky to have you. Pranav too, but he knows it.

Kira

Crazy intelligent, funny, kind, generally good human unit. In all reality, you're a great friend. You have made some parts of research exceptionally fun. You're going to be an especially gifted person one day, and I'm certain you'll drive forward human knowledge. Your hard work

and perseverance have never stopped amazing me – seriously! I've also totally benefitted from having heart-to-hearts regarding my life and yours. You've kindly shared your wisdom on a few things, and it was just that – wise. Please don't ever give up being a smart person, in every sense of that term. Maybe find a way to not sarcastically move or cynically view the world? Other than that, don't stop being you.

Danny, Martin, Joon

Best group of minions possible. You guys made acquiring the data for the FRESH paper a unique kind of fun. You guys taught me more than I could have possibly taught you. Joon, you know when we developed FRESH for the first time during that summer.

Acknowledgements

To Adam, I wish to express the most profound sense of gratitude and loyalty for giving me this chance to participate in something much greater than myself. Adam has displayed hallmarks of a great leader, mixing an understated-but-brilliant vision of tissue engineering's potential with a humor and understanding that is constantly growing. Adam has treated my peers with fairness, candor, and respect. More importantly, in times of need, he has shown the ability to adapt his intimidating persona to a supporting force for recovery. I wish him the absolute best possible outcome in his endeavors. I hope he becomes the sincere genius of his kin, and I hope I get to see it happen.

The input of Profs. Campbell, Lee, and Bettinger has helped me question my bearings on several occasions, reorienting me when necessary. I think these giants have lent their perspective in so many ways that I find it hard to feel wiser if only to keep asking grander questions. Their encouragement has additionally hardened my resolve and made it much more bearable when I doubt the necessity of that we do in research.

Prof. Yu-Li Wang has, through his tireless devotion to those under his guidance, been nothing short of inspiring. I am truly lost pondering his work ethic, and I cannot fathom how he finds time to read all the necessary correspondence or respond sincerely to half of it.

It goes without saying that the BME department in all it's tiny glory has been critical to my life these past years. Altogether, Vanessa's discussions on weather and Doctor Who, Prof. Hollinger's one-liners, and Sean's short-lived but lively discussions on cars were completely unnecessary yet invaluable to the rhythm of work at PTC. Zapanta is the easiest conversationalist I've met. Maryia is easily my favorite grad program administrator – please don't leave BME,

Maryia! There is also this guy named Jacob? John? Joseph? He's a music guy. An artist. Something…with two giant monitors on his desk. Misti knows I love having her around and hearing about her animals. And Kristin, Keri, and Mike – always open-door and always willing to help me. Through these lovely individuals, I developed a feel for the culture of BME, and I have grown to love it.

In as serious of a manner as is possible with him, I was lucky to work alongside the force of irony that is Quentin Jallerat, and only through him did I learn to grasp the fundamentals of microscopy. It was the passion that Quentin gave off when discussing his imaging work that led me to respect the care and focus required to learn the basics of confocals. While I wish I could have learned more from him (except FACS), his efforts to collaborate with me were far more valuable in the long run, allowing the both of us to prosper from the invaluable data in the FRESH paper.

While it comes as a bittersweet note to many, I must say thank you to the old guard of PTC for lending me their cynical musings regarding science and engineering. In my efforts to entertain such absence of purpose and futility of effort, I have grown to understand their frustrations and their love of life outside work. More complete is my perception of human existence and the necessity of imagination in the face of disappointment. And in so many ways I have come to feel grateful for this knowledge of being "human". So, thank you, guys.

I want to also say thanks to the NIH and to the DOD for their generous support through the NIH New Innovator (DP2HL117750) and CDMRP Breast Cancer Grants (W81XWH-16-1-0018).

Table of Contents

List of Figures

List of Tables

Chapter 1 Introduction

1.1 DCIS as a Disease

Ductal Carcinoma in situ (DCIS) results from an abnormal proliferation of epithelial cells lining mammary ducts and represents a pre-cancerous condition or low-grade cancer. Among women, DCIS is the 4th most common cancer diagnosis, and it is estimated that 1 in 10 women have undiagnosed DCIS[22]. Fortunately, only 20% of DCIS cases ever turn malignant. But, most patients elect for complete removal of breasts or some form of invasive intervention to avoid the 20% risk[1,2,12]. Currently, there are no clinically effective methods for distinguishing low and high-risk DCIS; therefore, most DCIS cases are treated as worst-case early-stage invasive cancers, requiring hormonal therapy, radiation therapy, and/or mastectomy[25]. This overtreatment of a cancer that is mostly benign represents a significant portion of the annual financial burden of female breast cancer – $16.5 billion in the U.S. alone for 2010[48].

Since nearly all cases of DCIS are removed before any become invasive, there is little understanding of what factors set aside pre-invasive cases from non-invasive variants. This overtreatment is encouraged by a 96-98% ten-year survival among patients diagnosed with DCIS; moreover, mastectomy, commonly a last resort for breast cancer patients, is considered curative for DCIS[23,55]. For patients who opt out of treatment, there is no way to guarantee they fall outside the risk of malignancy. Additionally, DCIS is difficult to spot using traditional screening techniques such as mammography and ultrasound, since it can be small and similar in appearance using these imaging modalities to the surrounding ductal epithelium. A better understanding of DCIS

is required to identify risk among patients and avoid overtreatment including unnecessary mastectomies.

Normal mammary duct is lined by a layer of lumenal epithelial cells and a layer of basal, contractile myoepithelial cells. DCIS typically arises from hyperproliferation of the lumenal layer, beginning as hyperplasia. As the hyperplasia becomes DCIS, it possesses one of several different morphologies that describe its appearance and the degree of ductal closure such as cribriform (spanning the lumen but full of holes) or papillary (finger-like growths from the lumenal surface)[1]. DCIS interacts heavily with myoepithelial cells and the basal lamina they maintain, and there is evidence that the presence of myoepithelial cells in mixed cultures of epithelial cells inhibits matrix metalloproteinase (MMP) activity by the lumenal epithelium[7,13].

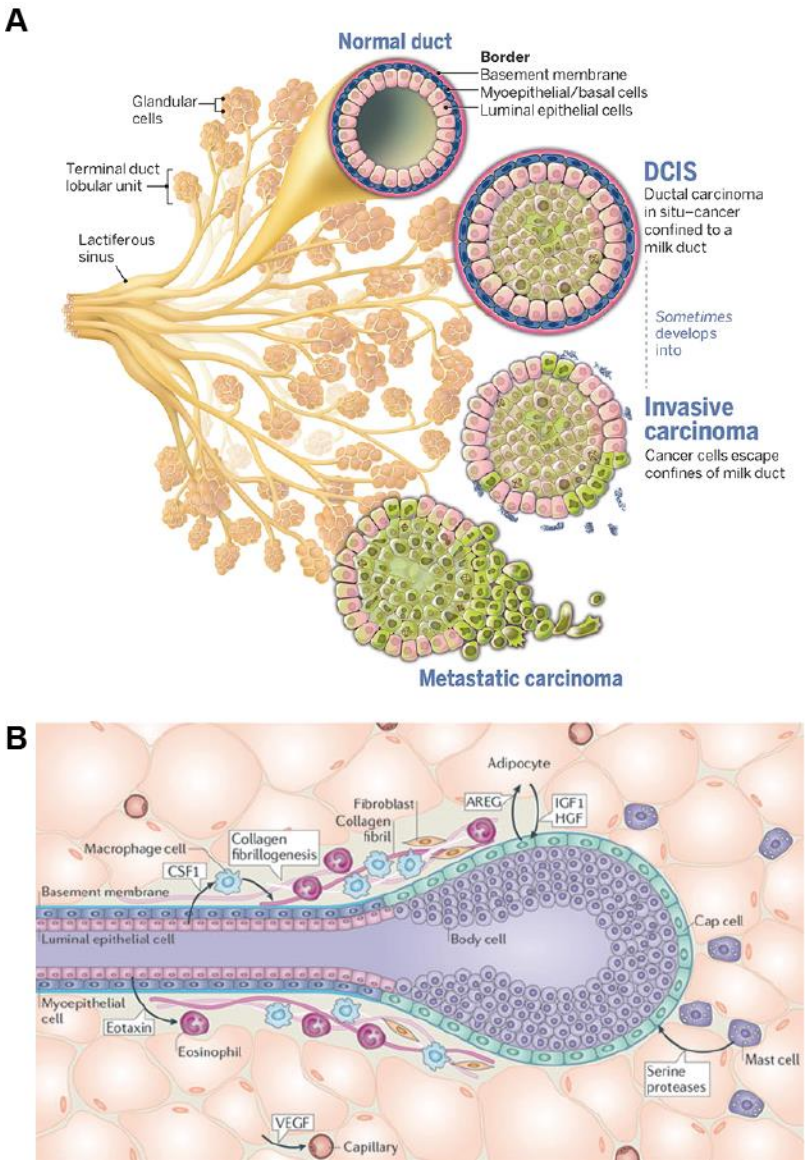

Figure 1.1 Lifecycle of DCIS and Structure of a Mammary Duct. (A) DCIS starts inside a duct with a well-defined border. Atypical hyperplasia of the epithelium results in DCIS. If the DCIS escapes the boundary of the duct, it is considered an invasive carcinoma. **(B)** The duct is a dynamic structure with many component interactions necessary to explain the full behavior of duct expansion and involution in vivo. Most DCIS arises from the more-proliferative cells found at the duct terminus, often inside an end bud in an acinus. (B) Adapted from Gjorevski et al. Integrated Morphodynamic Signaling of the Mammary Gland. *Nature Reviews: Molecular Cell Biology*. 2011, 12:581-593**.**

The transformation of DCIS to an invasive state in vivo allows ductal epithelial cells to come into direct contact with the stromal tissues surrounding the duct basement membrane. Within this complex stromal environment, there are lymphatic, ligamentous, vascular, and

nervous tissues, and the effects of each of these on the emergence of invasive DCIS are unknown. There is evidence that metalloproteinases at the site of invasion originate not only from the invading epithelial cells but also from stromal tissues[58]. Collagen fibrils maintained by fibroblasts in close proximity to DCIS microinvasions possess different alignment from the surrounding stroma, and the presence of fibroblasts in a gel encapsulating DCIS has been shown to encourage outward growths from the DCIS[63,66]. Clearly, interactions between DCIS and the surrounding tissues are involved in the progression toward invasive cancer, but few *in vitro* models incorporate the cells that surround DCIS in vivo[6,11,58,66,74].

1.2 Modeling DCIS

Except terminal end buds, ductal tissue includes two layers of epithelial cells, luminal and myoepithelial. Proliferation of the lumenal cells into the lumen of the duct is considered hyperplasia. Ductal tissues are regularly remodeled in accordance with hormonal processes, having highly proliferative states and autophagic/apoptotic involution states[71]. DCIS is thought to arise from atypical hyperplasia, when cell phenotypes within a proliferative lesion are irregular, though stimuli for this are not yet identified[13,16]. When DCIS grows past the barrier formed by the basement membrane surrounding the duct and situated at the base of the myoepithelial layer, it is considered invasive, though microinvasions are not indicative of malignancy[61]. Mice serve as the only in vivo model for studying DCIS, but the technical challenges associated with this approach present a significant barrier to widespread adoption[70]. In cases where the DCIS is implanted into the mammary fat pad of the mouse and not into the duct itself, this represents an already-invasive model which is not representative of the ductal confinement

of most DCIS. It is thus unclear if growth in the fat pad is indicative of invasiveness. Currently, there is no technique that presents primary DCIS cultures with a microenvironment consisting of endogenous ECM and cells, but combining these with carefully controlled bioassembly techniques such as 3D bioprinting could result in recapitulation of the necessary *in vitro* environment for DCIS survival and progression. Such a model would allow for drug testing and personalized medicine for most DCIS patients. In the long term, models like this would also allow identification of malignant subtypes of DCIS.

The promise of 3D tissue models derives from the fact that cells and their in vivo environment are, together, greater than the sum of the parts, displaying myriad levels of hierarchical synergy that effectively render the combination "alive". Without cells, an organ ceases to live, and without structure, cells lack the context necessary to perform a given set of actions. When grown in conditions that structurally represent in vivo environments, stem cells often adopt the behaviors of cells that would normally be found in such environments[59]. For example, a decellularized heart can be used as a template ECM in which perfused stem cells will begin to contract[59]. Regardless of the need for structure when designing a tissue, most of tissue engineering has been performed in two dimensions. Tissue modeling has found a firm believer in industries looking to offload the ethical burden of animal testing and chaperone tissue engineering into the 21'st century's vision of personalized medicine and targeted therapies, but most models that are in use, including lab-on-a-chip, are still very much two dimensional[36]. A fundamental reason for this is the difficulty in constructing complex and 3D structures from common tissue engineering materials such as collagen and alginate gels. These gels do not lend themselves to cutting-edge additive manufacturing techniques for constructing biomimetic

objects, and the results of trying to utilize them as such are often poor in geometric fidelity or biocompatibility[14,21,32,45]. Engineered tissues have yet to approach the relevance of animal models.

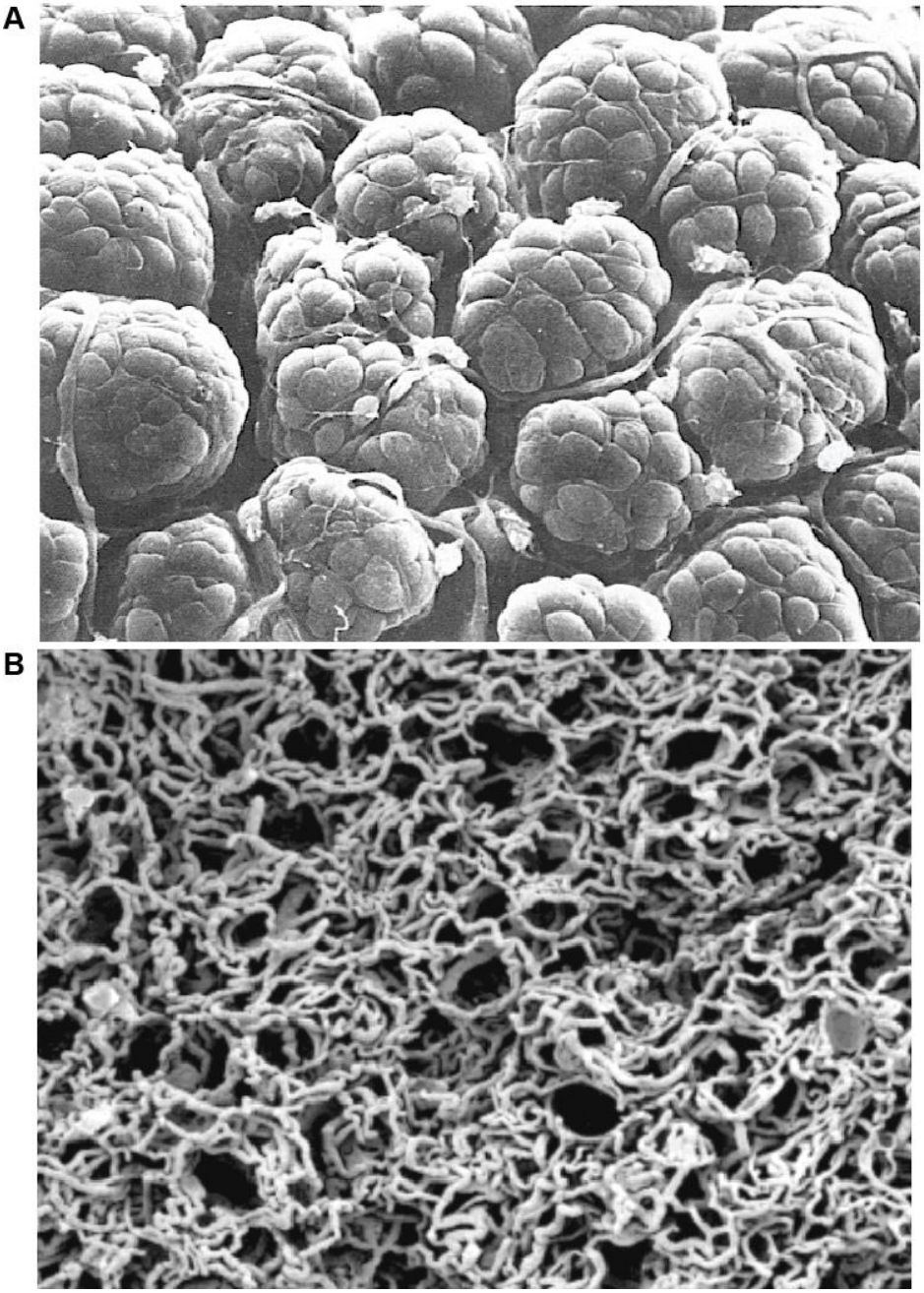

Figure 1.2 Microstructure of Mammary Acini and Associated Stroma. (A) Acini appear like berries with duct epithelium cells shown as the bulges of the berries and the web-like sulci occupied by the myoepithelial cells. **(B)** In-between and surrounding the acini is a rich capillary plexus. (A & B) adapted from Djonov et al. Vascular Remodelling During the Normal and Malignant Life Cycle of the Mammary Gland. *Microscopy Research and Technique*. 2001. 52: 182:189.

In numerous animals as well as *in vitro* models, it has been shown that cells derived from human cancers including carcinomas can be cultured into tumors that histologically mimic the parent tissue[8,40,70,72]. The best examples of these require the complex vascular and

stromal systems present in an immunodeficient animal model to completely recapitulate the cancer's growth[38]. Modeling such a cancer without a host *in vitro* requires a level of complexity comparable to mimicking an entire organism. Even though pH, nutrient concentrations, fluid shear forces, matrix properties, and cell-cell signaling are commonly associated with cell behavior, it is not known which factors inside a model organism present the requisite favorable conditions for a cancer's progression. To simplify model organism microenvironments, tissue engineers have developed a host of reductionist models utilizing a vast array of biomaterials and unique biochemistries. First among these materials is reconstituted basement membrane known under the product name Matrigel®, which contains a large assortment of proteins, growth factors, and proteoglycans. Materials such as Matrigel®, which come from animal-derived tumor cell lines, possess inherent batch-to-batch variability; therefore, there is little control over the relative levels of proteins such as Laminins, Collagens, and Fibronectins when using Matrigel®. Additionally, Matrigel®'s lack of collagen I sets it apart from connective tissues associated with invasive cancers, making it a poor model for late-stage invasive growths that are likely to encounter dense, well-organized collagen in vivo[19]. ECM derived from decellularized tissues provides a better biomimetic environment for a primary culture, assuming the ECM was sourced from the same tissue as the primary cells[67]. However, ECM chemistry is often more similar to collagen since collagen is the predominant material in most tissues[62]. Therefore, it is important to understand how lessons learned from engineering collagenous constructs can be directly translated to ECM gels. Incorporating reconstituted ECM (reclaimed from living tissues) within a construct ensures that the composition most closely mimics the parent tissue and is best suited to preserving the phenotype of any included cancer cells.

1.3 Designing and Fabricating Biomimetic Hydrogel Scaffolds

A hydrogel scaffold is typically cast inside a mold with specialized topographical features that are integral to the design of a specific *in vitro* application. Often, these features are positive mandrels around which a seeded hydrogel can compact or a fugitive material which can be removed to produce a void within the cast hydrogel[33,51]. Unfortunately, the effect of complex geometries like vasculature and laminar sheets of basement membrane in an *in vitro* model isn't well understood, because the ability to assemble biopolymers in this fashion hasn't existed until recently. Efforts to recapitulate a lumen and surrounding stroma using microfluidics have shown that it is possible to construct coaxial tubes with multiple different cell types in different ECM gels, but the behavior of included pre-malignant cells is unlike that found in vivo, with lesions being uniform instead of atypical[6,11,46,66]. The heterogeneity and complexity of in vivo tumors is likely absent due to the simplicity of the models used. Without additional levels of complexity such as laminin-rich basement membranes and branching, interconnected networks of tubes, it is impossible to guarantee that the invasive and proliferative behaviors seen in vivo can be recreated *in vitro*.

When incorporating additional cell types into a model of DCIS, the spatial arrangement of cells and ECM is often structured as a single layer of epithelium and a surrounding stroma. Tubes and membranes with layers of cells have shown that it is possible to recreate polarization and epithelial monolayer formation, but few scaffolds have demonstrated a multi-layered epithelium with an interior lumen void of cells[6,11,66]. For many types of tissue, it is possible to perfuse a channel with one cell type followed by an additional cell type to create layered arrangements of cells. Microfluidic techniques used in the generation and control of perfusable hydrogel

structures offer elevated levels of accuracy and precision when creating singular channels lined with cells. This approach has been demonstrated for ductal epithelium, but only one model has shown maintenance of distinct lumenal and myoepithelial phenotypes with some level of invasive transition[74].

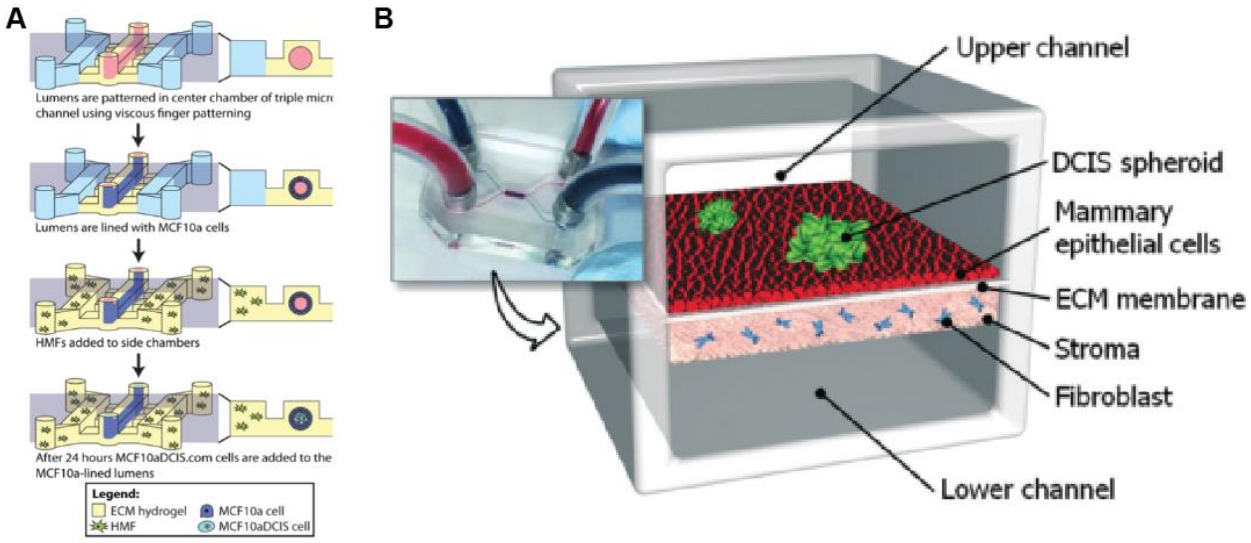

Figure 1.3 Microfluidic Models of DCIS (A) Series of nested hydrogel-based tubes can be created by using serial microfluidic perfusion setups that rely on the viscous fingering effect of a low-viscosity fluid through a high viscosity one. DCIS cell lines can be seeded in the lumen of the microfluidic setup to model DCIS progression in the presence of multiple cell and gel types. **(B)** Membrane microfluidics can be used to partition DCIS-on-epithelium from a stromal culture of fibroblasts in ECM gel. (A) Adapted from Bischel et al. *BMC Cancer*. 2015. 15: 12. (B) Adapted from Choi et al. A microengineered pathophysiological model of early-stage breast cancer. *Lab on a Chip – Miniaturisation for Chemistry and Biology*.2015. 15: 3350:3357.

When creating a more complex branching tube, it is impossible to guarantee that perfusion-seeding will result in a homogenous distribution of cells in each branch, since flow along each branch can differ[35]. This problematic idea of uneven flow splitting only becomes more apparent as bifurcations in the tube become increasingly heterogeneous with decreasing diameter. While bifurcations, fluid valves, and flexible membranes made of various elastomers and biopolymers are features of modern microfluidics, these structures remain difficult or impossible to construct within soft hydrogels and are seldom incorporated into these devices[4,10,34]. Moreover,

incorporating cells into these systems is usually accomplished with little control over spatial distribution. Limitations in microfluidic architectures stem from the requisite lithographic fabrication methods that, until the advent of 3D printing in microfluidics, were incapable of producing 3-dimensional curvatures such as helical tubes or space-filling manifolds[31]. While the use of lithographic techniques in microfluidics will remain a vital part of technologies such as lab-on-a-chip, 3D printed microfluidics will allow soft hydrogels to incorporate greater levels of complexity and spatial heterogeneity that may be essential to their function as *in vitro* models of various tissues.

1.4 Rapid Prototyping Tissue Models of Mammary Duct Epithelium

Recapitulating the structure of a tissue will entail the use of endogenous ECM, primary cells, and a highly heterogeneous 3D architecture modeled after native tissue. Since it is already straightforward to image and model a variety of tissue structures, we need only figure out a method for assembling these tissues from their ECM and cells. We developed Freeform Reversible Embedding of Suspended Hydrogels (FRESH) to tackle this challenge. FRESH demonstrated that it was possible to freeform 3D print a variety of soft biomaterials such as alginate, fibrin, Matrigel®, and collagen, with or without cells. At the length scales possible using our modified Fused Deposition Modeling (FDM) 3D printer, it's possible to extrude 150 µm strands of cells embedded in hydrogel and create even smaller voids between these strands. The software associated with these FDM printers (Slic3r) allows us to meticulously change the output of the 3d printer for different regions of a 3d print, print multiple materials, and incorporate heterogeneous porosities. Effectively, the smallest distinct solid feature is 150 µm, and the

smallest void is closest to the stepping accuracy of the 3D printer – approx. 10 - 15 µm. The number of extruders is hardware-limited to 6, and the volume of possible extruded material is limited to the current syringe pump capacity, approximately 60 mL. To put this into perspective, a scale model of a branch of the right coronary artery requires approximately 400 µL of ink and 11 minutes to print, barely testing the limits of our machine. In theory, it is possible, with the current electronics and minimal hardware modifications, to combine 6 materials (cell suspensions, collagenous ECM, and fugitive inks) in any geometric arrangement imaginable, with features down to 150 µm. However, such a complex use of FRESH bioprinting has not yet been demonstrated. Utilizing FRESH to fabricate a biomimetic mammary duct *in vitro* would set a precedent for tissue engineering that combines unmodified ECM materials and inexpensive technology to produce a fundamentally customizable model tissue for an invasive disease. The study of such a model could shed light on more than DCIS, possibly enriching the knowledge of pancreatic, prostate, and other epithelial cancers. If we can fabricate complex, perfusable, and biomimetic constructs using collagen-based materials and cells, we may be able to better model all tissues *in vitro*.

Herein, we establish a set of protocols necessary to rapidly prototype ECM gels with unprecedented complexity by combining a newly developed method for 3D printing gels, a rapidly evolving open source software and hardware ecosystem, and rapid prototyping. Starting in chapter 2, we develop the modifications necessary to modify consumer 3D printers into syringe-based printers. Chapter 3 is focused on further development and optimization of a set of techniques for additively manufacturing complex 3D structures from hydrogels. Then, in Chapter 4, we combine these platform components into a novel method for producing biomimetic

mammary duct epithelium models. We show that printed scaffolds with given geometries can be used to culture epithelia into tubular monolayers mimicking the clear division between lumen and stroma found in vivo. After optimizing the method for creating biomimetic models, we create a complete, to-scale ductal epithelial tree from collagen type I modeled on tomographic data from mouse mammary glands and demonstrate freeform parity between the print and data, demonstrating superior levels of collagen print complexity and doing so on an open source platform.

This work carves a path for those seeking to construct highly complex structures from ECM gels like collagen type I and alginate, and it sets the stage for further adoption by utilizing widely accessible software tools and hardware to meet these goals. As an example tissue model, the ductal epithelium represents a leap toward true parametric 3D culture of cells in an environment with mechanical and chemical cues, but the flexibility of its fabrication more importantly demonstrates a rapid prototyping process for ECM gels that is not limited by hardware, geometry, expense, or gel chemistry.

In addition to the innovations described herein, we outline the limitations of current platforms and extend the concept of "embedded" 3D printing toward combinations of gel systems and advanced design of systems capable of printing faster, with higher accuracy, and with open source components.

Chapter 2 Designing an Open Source Hardware and Software Platform for 3D Printing Gelling Fluids

2.1 Abstract

3D bioprinting seeks to additively manufacture fluid gels with and without cells into complex structures more suited to replicating in vivo function than cast constructs. Until recently, 3D bioprinting research has focused on repurposing stiff, non-biological materials in various forms of transformative culture to represent simplified geometries or introduce porosity in novel fashions. The preponderance of 3D printers in the recent decade, mostly attributable to the maker movement and the RepRap project, has led to the creation of many forms of fluid-based 3D printers. Most of these iterations on the idea of a syringe-based printer were suited for clay and paste printing, but none of them were designed to dispense small volumes of fluid in a precise fashion. Utilizing an extensive background andunderstanding of 3D printer design and basic rapid prototyping practices, we demonstrate the design and optimization of a bioprinter utilizing additive manufactured parts and open source tools. We illustrate the extensibility of this system toward printing multiple materials at a broad range of speeds and settings that are open to modification by users and engineers alike. From our efforts, an open source and capable bioprinter utilizing syringe-based extrusion was created and verified capable of 3D printing a variety of different fluids.

2.2 Introduction

When the patents protecting fused deposition modeling (FDM) from consumer reutilization expired, the RepRap project and the maker movement were born[37]. Fused deposition modeling is a method of additively manufacturing an object from layered patterns of extruded material, typically a thermoplastic. The RepRap project, started at the University of Bath in the UK, sought to recapitulate the fundamentals of FDM in a system that was capable of inexpensively reproducing all its necessary components excepting those that were necessarily metal or electronic. The maker movement sprang up in response to the confluence of 3D printing knowledge that followed on the heels of not only the expiration of FDM patents but also the patents protecting stereolithographic techniques. Combined, RepRap and maker efforts have driven 3D printing from an experimental hobby to a standalone manufacturing platform found across the world in thousands of businesses and laboratories.

Despite the swelling of 3D hype on the heels of the maker movement, there was little 3D printing innovation in tissue engineering beyond trying to execute various forms of FDM with thickened gel systems such as alginate or UV-treatable materials consisting of PEG. Even so, there were systems available for purchase, promising "bioprinting", "bioplotting", and other relabeled versions of FDM using these gel systems[20,32,39,45,52,62]. In some cases like EnvisionTEC's Bioplotter, the primary selling point was actually thixotropic silicone resins that were claimed to be biocompatible, and similar materials were printed on significantly less expensive Fab@Home 3D printers[44]. Most printers offering to behave as a "bioprinter" operated by pushing fluid out of a syringe onto a plate with various kinds of mechanical control over position along XYZ axes. Very little, if any, research was done on the actual control of extrusion beyond stopping and

starting extrusion using air pressure or a crude leadscrew. And yet, all of these systems utilized syringes as ink reservoirs.

Considering the variety of syringe pump designs, it is straightforward to derive a set of principles for their operation such as method of transmission, motor design, linear guide construction, electronic control, and mounting, and these principles were generally adopted by not only the Fab@Home but also the Organovo MMX system. Generally speaking, such bioprinters pushed on a fluid inside a syringe to deposit a given volume in a given spatial pattern in order to "print" the fluid in layers. However, neither of these systems offered general control over placement of fluids in a single print. Software systems that accompanied these machines were closed source and limited to a subset of oversimplified choices without access to underlying decision-making processes. Users had very little control over how the machines operated, and the software infrastructure was not open to modification.

From the very beginning of the open source RepRap project, RepRap machines relied on the open and extensible python programming language to produce standard RS-274 numerical control instruction sets (G-code). Due to the nature of these python programs (collectively called Skeinforge), the ability to control virtually every single aspect of FDM on experimental RepRap hardware quickly became the *de facto* standard of the movement. Many early adopters were actually discouraged by the level of complexity of the control software and quickly gravitated toward alternative software packages such as the perl-based Slic3r or the alternative python package Cura that offered simplified interfaces.

RepRap printers mostly featured Atmel 8-bit microcontroller IC's controlling 1.8° NEMA 17 stepper motors, one motor for each of the X, Y, Z, and extruder axes. These printers were

capable of generating very accurate (~10 µm) and precise (±15 µm) movements in all axes, and some early examples of RepRap-based machines including the Ultimaker 3D printer were capable of rendering models with complex organic forms down to 20 µm layers. While the software for controlling these machines was clunky and difficult to use, it offered a vast level of control that was not available through any other platform.

These machines relied on the same kind of extruder actuation – a NEMA 17 stepper motor with a specially designed gear that bit into a plastic filament and forced it through a heated nozzle. Virtually all syringe pumps available operate with a stepper motor, and many of them would, in theory, be a drop-in replacement for any RepRap printer extruder if the motor was geared down a sufficient amount or the firmware was altered to perform this gear reduction digitally. Not surprisingly, some examples of this kind of innovation were present from very early days of the RepRap project, but most of the extruders were for very large amounts of fluid and were poorly designed for sustained operation with small volumes of fluid.

In this chapter, we describe the modification of consumer-level RepRap-based 3D printers to functioning fluid printers. First, we outline the relevant constraints when designing a syringe pump extruder for a RepRap printer. Then we identify and alter necessary aspects of machine operation by firmware and software. To test the printer, we demonstrate FDM printing a Bingham plastic fluid, in this case, mayonnaise. Finally, we expand the printer's capability to multiple material prints with the addition of a second syringe pump extruder.

We describe a straightforward approach to produce a "bioprinter" using inexpensive hardware and open source software; moreover, our platform is directly compatible with all RepRap-supported softwares which currently dominate pro- and consumer 3D printing. These

systems are already serving as a template for bioprinting in several labs across the world, and, in terms of capability, they offer greater flexibility and speed than most commercially available solutions. Essentially, these systems will allow researchers to print more materials faster with greater accuracy, precision, and control over all aspects of fabrication.

2.3 Materials & Methods

2.3.1 Identification of key variables in designing a fluid extruder for a 3d printer

There were a few separate options available when I first considered designing a fluid extruder for 3d printing, many of them finding use in one or more 3D printers requiring either a syringe or some other bulky fluid reservoir for "ink" retention. Motorized pumps either carried the motor next to the syringe or utilized flexible coupling between the motor and the syringe to drive a leadscrew or rack and pinion to actuate a syringe plunger. Pneumatic syringe pumps typically balanced high and atmospheric pressures across solenoids and would serve high pressure to an ink reservoir to start extrusion and vent it to atmosphere to halt extrusion. Peristaltic pumps were inherently pulsatile and did not offer pulse width modulation without sophisticated mechanisms. Moineau pumps and other exotic fluid pumping mechanisms were practically impossible to create without expensive investments in machining or proprietary modules. It was decided that the most sensible decision for a fluid extruder was a simple stepper-driven syringe pump. Since the pump was going to be mounted to a 3D printer XY carriage, it was thought that keeping the center of mass of the pump near the XY carriage plane of travel would result in better overall behavior during printing and reduce instantaneous loading on the rods/bearings. Therefore, the most compact form of syringe pump, a geared one, was chosen.

This decision was somewhat serendipitous as most syringe pumps are also a geared stepper-driven system.

Pumping discrete amounts of fluid requires a system with high responsiveness in order to ensure that fluid movement upon initiation of pumping is quick and stops immediately when pumping halts. The Replistruder syringe pump was designed to host a stepper motor on its back and feature a gearing system to link the stepper motor to the leadscrew drive system. The leadscrew drive was designed as a trapped pair of nuts inside a gear. As the gear spun, the leadscrew would progress through the threads of the also-spinning nuts. In later iterations of the Replistruder, the nuts were held under compression by the body of the Replistruder. Nuts held in compression toward one another have less slack between their respective sets of threads. Essentially, the two nuts held in compression were capable of driving and back-driving the leadscrew along its axis without any slack. This precision, in turn, means that reversing the extruder drive motor would result in nearly instantaneous reversal of the leadscrew along its axis. One often unforeseen advantage of this ability to reverse driving direction within the syringe pump was implementation of the "retraction" feature of modern desktop FDM softwares, which quickly reverses the extruder before moving across the print bed in a non-extruding "travel" move. When retracting, the goal is to stop "ooze" of molten plastic from the extruder while moving to a location where extrusion is desired. In much the same manner, a syringe pump full of a fluid with microbubbles must be back-driven to stop fluid "ooze" at a given point. Therefore, our pump was designed with this ability to retract fluid in mind to allow us to account for any delay in fluid responsiveness during printing.

The gearing between the stepper motor and the leadscrew would be the next most likely system to develop slack. For connecting the motor to the leadscrew, it was possible to select pulleys with differential sets of teeth and a Kevlar-reinforced belt between them, but the relative precision of gears and belted transmissions is indistinguishable at the speed and forces seen in a syringe pump using a NEMA 17 motor. Therefore, it was designed as a set of herringbone helical gears which have the highest surface area contacting each other at any given time and cannot slip along the axes of rotation. Gears were designed with prime numbers of teeth (47 and 13) so that any 100 given rotations will never repeat contact with the same set of teeth between the two gears. The contact angles of the teeth were set to 20° with an inclination of 11° which is generally considered the lowest friction combination of parameters for a helical tooth. The gears were then scaled to fit the minimum distance between the axes of the motor and the leadscrew, which was centered on the syringe plunger.

To design the rest of the syringe pump, the syringe had to be selected. Hamilton Gastight® syringes occupy a relative monopoly in the market, and they are used across the board in various syringe pumps, chromatography, mixing, sampling, and printing systems offered by hundreds of manufacturers. Plus, they possess a 6/32 standard threading in their plungers. This means that, were we to choose them, more people would have access to them and a 6/32 threaded rod could be used as the leadscrew as well as the coupling mechanism between the syringe and the pump. Before a small syringe (and its inherently narrow plunger) was chosen to design the pump, it was realized that a larger syringe might be desirable at a later point, where larger prints may demand in excess of 5 mL of ink. Therefore, we chose a 10 mL syringe to serve as the basis for the pump, thereby establishing the minimum distance (34.65 mm) between the

axes of the gears that would allow for not only the 10 mL syringe but also syringes with volumes less than 100 µL.

Repetitive operation of the syringe pump extruder eventually causes depletion of syringe volume, which then requires refilling. It is also often the case that a syringe filled with a sensitive "ink" needs to be stored and would have to be removed from the printer and Replistruder before refrigeration. To make the process of storing or refilling a syringe easier, the syringe pump was designed with various mechanisms for easily accessing the syringe and decoupling it from the leadscrew transmission. One iteration of the Replistruder featured a spring-loaded chassis that held the entire transmission and syringe in compression but could be opened in one smooth motion, but this flexibility made the entire system relatively less responsive. To fix this problem and many others, the most recent iteration of the Replistruder was designed to quickly disconnect from the printer, leaving the motor and its gear behind and allowing the user to store the syringe and Replistruder as one sealed unit under refrigeration.

When transporting a Replistruder from printer to refrigerator and back, the handleability and stability of the pump go hand in hand. It was important to have a device that did not break between repeated loadings and jostling about in users' hands. The body of the Replistruder was designed to be composed of as few pieces as possible with as little moving parts exposed excepting those that are useful to access. Then, the syringe pump was given rounded surfaces for ergonomics and as much mass as possible along the axis of compression to ensure that the pump was as stiff as possible and would transfer any forces from the transmission efficiently to the actuation of the syringe.

Syringes were always mounted by the glass flange present at the top of the syringe's barrel. Different volume syringes had "adapters" for their flanges that each fit into the overall Replistruder assembly. For each syringe, greater than 75% of the syringe barrel was left exposed with its fluid volume demarcations visible from any angle. In the first iterations of the Replistruder, it was thought that lateral confinement of the syringe barrel was important to maintain alignment between the syringe's barrel and the axis of the leadscrew and ensure efficient operation. However, later iterations achieved perfectly sufficient alignment without this confinement. That is, later iterations shed relatively useless (lateral confinement) mass by stabilizing the syringe using higher levels of compression across the glass flange at the top of the syringe barrel. Checking for misalignment was simply accomplished by positioning the syringe plunger at the top and bottom of its stroke while in the Replistruder. In each position, the leadscrew was lowered until it just barely touched the top surface of the syringe plunger, and it could be seen how far off center the leadscrew was in reference to the plunger. In all syringes and iterations of the Replistruder, there was no visible misalignment. Additionally, it was found that the exposed syringe (with needle) represented a significant risk to users when the entire syringe-replistruder assembly was removed. To alleviate this, the bottom plate of the Replistruder which holds and pushes up against the glass flange of the syringe was extended downward and threaded so that a 15 mL centrifuge tube could be slipped over the syringe and needle and secured via a 360° rotation to the bottom plate. For larger syringes, this was changed to a 50 mL centrifuge tube with an identical thread.

Replistruders had to be 3D printable, since this was the easiest method to produce our designs without incurring large costs. To ensure each Replistruder design was printable, certain

rules were followed during design processes. For example, gears were designed with teeth large enough to print their contacting surfaces using the standard 400 µm nozzles found on our 3D printers. All parts were designed so that there were few unsupported overhanging features. Walls and thin sections in the parts were designed to be a multiple of 400 µm – 1.6, 2, or 2.4 mm to allow the printer to create these walls as solid without requiring unusually spaced patterning.

Measurement of Replistruder design efficacy was accomplished by changing "retraction" values in printing software until a value that resulted in zero "ooze" of ink from a nozzle after a print was completed was established. This value usually started around 0.2 mm and was decreased to the correct value in later iterations of the Replistruder.

2.3.2 3D Printing Replsitruders

Replistruders were printed from ABS and PLA plastics on a MakerBot Replicator 2X modified with an extrusion cooling fan. The prints were executed using MakerBot Desktop 3D printing software. Parts were printed at 70-90% rectilinear infill, 2 perimeters, and 250 µm layers. Rigid mounts that connected to mounting holes on Replistruders were fabricated and used to mount the Replistruders in place of the thermoplastic extruders on various 3D printers.

2.3.3 Construction of a Two-Extruder 3D Printer

A defunct MakerBot Replicator 2 (shown in Appendix C) with a dead motherboard was stripped of body panels, and its wiring was exposed and spliced with header cables. A RepRap Duet v0.8.5 3D Printer Motherboard was installed and connected to the endstop microswitches, the stepper motors, and the MakerBot's 19V power supply. The Duet was flashed with the latest

version of RepRap Firmware, which is an open-source object-oriented firmware blob intended for modern, 32-bit 3D printer controllers. Flashing was accomplished using Bossa.exe, a program offered by Atmel (atmel.com). Without a configuration file present onboard the controller, the firmware will operate in a default state that prevents damage to the controller. A custom configuration file for the Duet motherboard was generated to allow the controller to operate as intended in accordance to its hardware. A web interface consisting of a basic webserver with a java-based controller was included in the Duet's storage alongside its configuration files. This web interface would serve as the host for printing in place of USB host communications. The printer was then connected via Ethernet to a PC, and manual control of the printer was accomplished by accessing the Duet's webpage through a web browser such as Google Chrome. In the future, the printer can be connected to any Wi-Fi router and be accessed by phone or any computer running a basic browser. The carriage responsible for shuttling the extruder payload of the MakerBot was replaced with a custom design shown in Figure 2.1A. This new design was able to host two Replistruders.

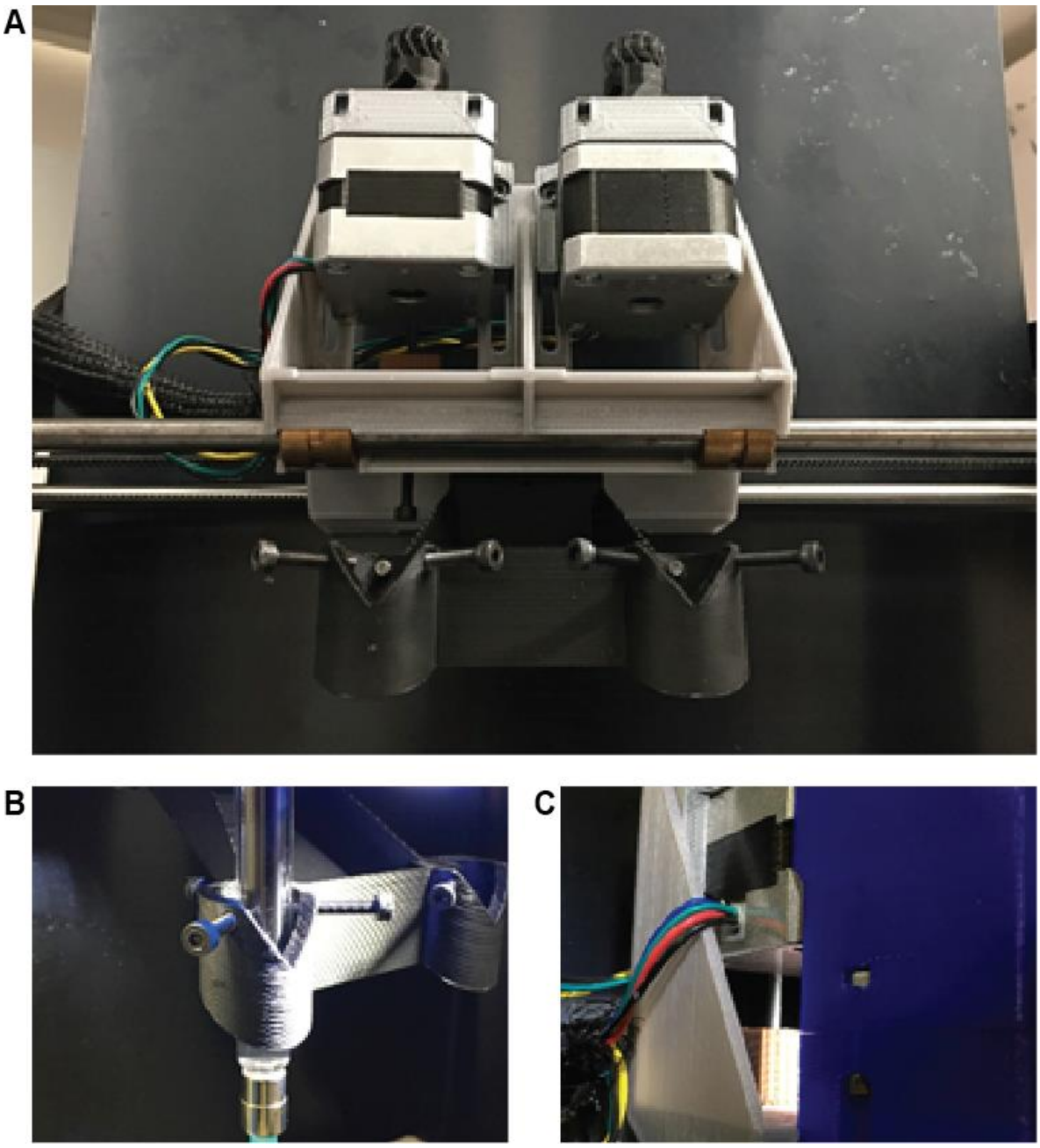

Figure 2.1. Construction of dual extruder mount with adjustment screws. (A) The dual extruder replaces the carriage used to shuttle the thermoplastic extruder. **(B)** The syringe of each extruder is adjusted in XY via three adjustment screws. **(C)** Each extruder is adjusted in Z via a single adjustment screw that pushes the motor up and down.

The custom dual extruder carriage was designed to allow each Replistruder to undergo fine adjustment in XYZ relative to the other. Each extruder was adjusted in XY via three separate screws surrounding and contacting the syringes shown in Figure 2.1B, below the point where

they project from the body of the Replistruder. Then, to account for different syringe lengths, a vertical adjustment screw for each extruder was included (Figure 2.1C). These adjustment mechanisms allowed for careful alignment of Replistruder nozzles relative to one another and proved crucial in later experiments involving multi-material prints.

2.3.4 Modification of printer firmware parameters

Several kinds of printers were used during our experiments. MakerBot Replicators were connected via USB host and flashed with v7.7 Sailfish firmware which was desired due to its open access to acceleration and jerk values for axis movements. After connecting to the printers with ReplicatorG software and flashing firmwares, acceleration values were set at 1300 mm/s^2 for X and Y, and jerk, which indicates the instantaneous turnaround in mm/s and is, in fact, a misnomer, was set to 20 mm/s for X and Y. To artificially "gear" the extruder actuations down to an appropriate value for the Replistruders, the MakerBot's steps/mm value of the extruder axis had to be altered in an XML file used by ReplicatorG to "update" machine firmware values. First, it was necessary to calculate the number of 1/16 microsteps used by the extruder's stepper motor to advance the Replistruder leadscrew by 1mm. The calculation was as follows:

$$\frac{14{,}575\ microsteps}{mm} = \frac{16\ microsteps}{1\ fullstep} * \frac{200\ full\ steps}{revolution} * \frac{47\ teeth}{13\ teeth} * \frac{32\ revolutions}{25.4\ mm\ travel}$$

The number of microstep divisions applied for every one of 200 full steps in a MakerBot motor's revolution was used to find the total number of microsteps per motor revolution – 3200. Then, the gearing ratio was used to fine how many microsteps it took to turn the leadscrew gear one

revolution – 11,569. Then, the number of revolutions required for a 1 mm vertical travel on the leadscrew was calculated – 1.25984. Finally, the total number of microsteps per 1mm of travel on the leadscrew was calculated to be 14,575. This value held for all iterations of the Replistruder and was entered into the firmwares of all printers used.

Printrbot "Simple Metal"'s were connected via Repetier Host software and instructed to change their X/Y acceleration to 1000 mm/s^2 and their X/Y jerk to 15 mm/s. Again, jerk is a misnomer and indicates instantaneous change in velocity for a given axis. These changes were executed using the Gcode commands M201, M205, and M500. Steps/mm for the extruder axis was altered to the above 14,575 value by the M92 command.

The Duet based custom printer was configured from the beginning to use 14,575 microsteps/mm on the extruder axes by inclusion of the M92 command in the configuration file onboard the controller. The configuration file is as follows

```
M111 S0                                   ; Debug off
M550 PReplicator2Bio                      ; Machine name
M551 Pnotthepassword                      ; Machine password
M540 P0xBE:0xEF:0xDE:0xAD:0xFE:0xED       ; MAC Address
;M552 P0.0.0.0                           ; Un-comment for DHCP
M552 P192.168.1.15                        ; IP address, comment for DHCP
M553 P255.255.240.0                       ; Netmask
M554 P128.237.128.1                       ; Gateway, comment for DHCP
M555 P2                                   ; Set output to look like Marlin
G21                                       ; Work in millimetres
```

```
G90                                ; Send absolute corrdinates...
M82                                ; ...and absolute extruder moves
M563 P0 D0 H1                      ; Define tool 0
G10 P0 S21 R20                     ; Set tool 0 operating and standby temperatures
M563 P1 D1 H2                      ; Define tool 1, uncomment for dual
G10 P1 X19 S-273 R-273             ; Set tool 2 operating and standby temperatures
M574 X2 Y2 Z1 S0                   ; set homing switch configuration
M208 X250 Y150 Z150                ; set axis maxima and high homing switch positions
M208 X0 Y0 Z0 S1                   ; set axis minima and low homing switch positions
M569 P0 S0                         ; Drive 0 goes backwards
M569 P1 S0                         ; Drive 1 goes backwards
M569 P2 S0                         ; Drive 2 goes backwards
M569 P3 S0                         ; Drive 3 goes backwards
M92 X88.57 Y88.57 Z400 E14575      ; Set extruder steps per mm
M201 X1300 Y1300 Z20 E500          ; Accelerations (mm/s^2)
M203 X15000 Y15000 Z100 E300       ; Maximum speeds (mm/min)
M566 X300 Y300 Z30 E0.25           ; "Jerk" velocities (mm/min)
M906 X800 Y1000 Z500 E800          ; Motor currents (mA)
```

2.3.5 Validation of Modified 3D Printer Operation

Replistruders were mounted to 3D printers via custom-designed mounts that fit each modified printer. These mounts are shown below in Figure 2.3.2. A Hamilton Gastight 2.5 mL

syringe was filled with mayonnaise, and the Replistruder-equipped printers were fed a basic printing script that would normally be used to print a 10 mm solid cube from PLA , but the file was altered to require no heating for extrusion. Also, the file did not utilize a "homing" routine at the beginning but instead, it assumed the nozzle was located at the center, bottom of the cube in Cartesian space. A 32-gauge needle was secured to the end of the Replistruder. The Replistruder was positioned so that the needle was just touching the platform. The printer then executed extrusion of the Mayonnaise in a pattern that built up a cube, layer-by-layer at a location centered where the nozzle was initially positioned.

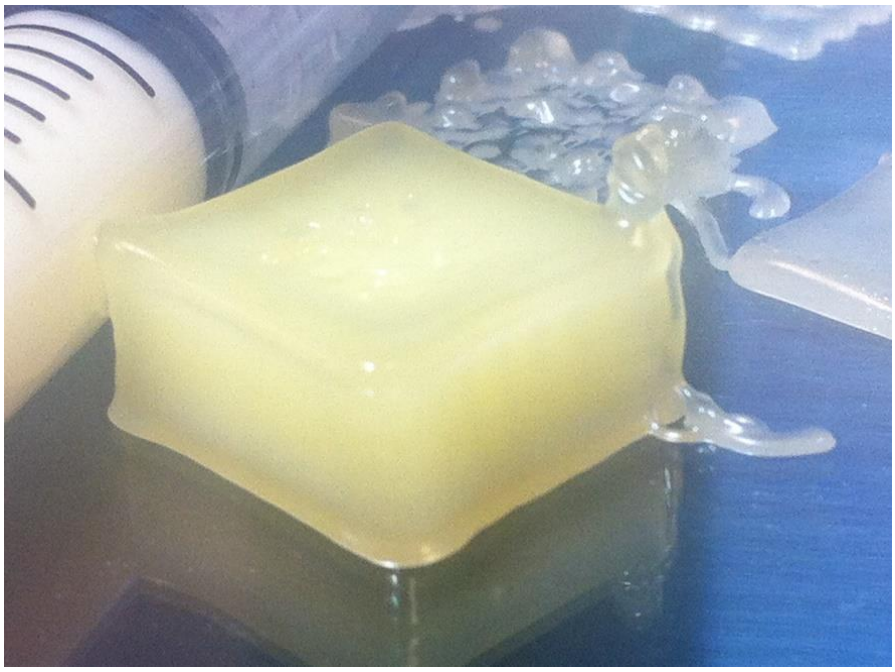

Figure 2.2 Testing FDM theory with a fluid ink - Mayonnaise. The first iteration of the Replistruder was tested by extruding mayonnaise in a calibration rectangular solid shape.

2.3.6 Calibrating a Fluid Printer with Multiple Nozzles

Having two Replistruders on a printer with a given intended distance between their nozzles was not enough to allow for dual material printing. It was necessary to align nozzles in

X, Y, and Z in order to allow the machine to swap nozzles during printing and correctly deposit the second material in relation to the first. To align nozzles, it was necessary to create a reliable system for gauging alignment. Normally, expensive optical alignment tools are required for this sort of procedure, but it was carefully figured out how such a cost could be avoided.

A laser cutter was used to engrave shallow X and Y lines in the very-flat acrylic build plate of the Duet-based custom 3D printer. Two sets of hairline crosshairs with 58.5 mm separation were engraved. This separation corresponded to the intended separation between Replistruder nozzles. These lines were orthogonal to one another and to the Z axis. The platform was then carefully adjusted on the printer to ensure it was coplanar with the X and Y gantries. This adjustment was accomplished by carefully minimizing the separation between a needle of a single Replistruder and the platform until it was approximately equal across the entire platform. Once it was verified that the travel of any given Replistruder was in a plane parallel to the platform, the platform was brought into contact with one needle of one Replistruder, arranged in the center of one of the engraved crosshairs (Figure 2.3A). The second Replistruder was then carefully adjusted in X, Y, and Z until it was also just-barely-touching the platform and centered in its crosshair (Figure 2.3B). Then, it could be assumed that both Replistruders were approximately 58.5 mm apart along the X axis and coincident in YZ. Once this alignment was complete, printing software was informed of the 58.5 mm offset between nozzles, and all multi-material prints were then-on handled automatically as two separate sets of extrusions approximately offset by 58.5mm. The result was that the printer swapped extruders for each layer including both materials, printing one then the other.

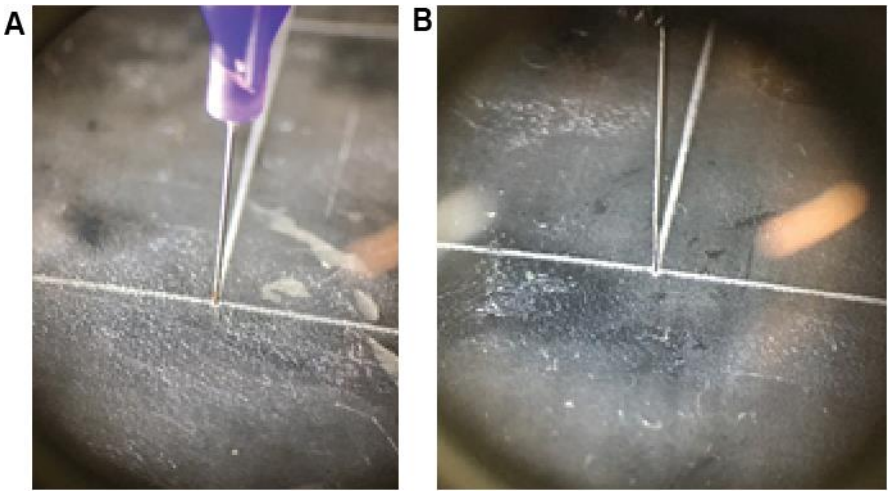

Figure 2.3 Aligning two Replistruder nozzles relative to one another. (A) The larger of two needles is aligned to the first of two crosshairs etched on an acrylic plate that is parallel to the XY plane of the 3D printer. **(B)** The second of two needles is aligned to the second crosshair.

The only required difference in dual material fluid printing is to ensure the nozzle of one extruder does not slam into the edge of a printing container when swapping with the second nozzle. This problem is very simple to fix – a lift command is inserted before extruders are swapped such that the extruder and print platform experience a vertical clearance before swapping is performed. The command is, "G91, G1 Z20, G90".

2.4 Results & Discussion

2.4.1 Design and Iteration of Replistruder v1

Replistruder v1 (shown in Figure 2.4) was a breach-loading geared syringe pump designed in 24 hours to sit on a MakerBot Replicator Dual 3D printer. It borrowed heavily from principles of tranquilizer dart guns – the entire body could hinge open, and a full syringe and needle could be loaded in. Closing the pump and engaging a cross-bolt would lock the assembly in its operating position. A keyed "coupler" was slid over the end of the leadscrew and the head of the syringe plunger, and the Replistruder was ready to operate. The leadscrew used was an M3 thread with

a 1:1 gearing with the stepper motor. This version of the syringe pump left a lot to be desired, but it did allow for consistent operation using a few different syringes. When operating at extremely low flow rates, the 1:1 gearing caused the transmission to bind or fail to turn altogether. Additionally, operating the stepper motor at such a low flow rate resulted in the motor overheating from effectively being used as a DC resistor rather than an AC inductor. This overheating was the result of the motor's coils operating under constant, direct 400-600mA of current for extended periods without switching. Estimated retraction values for effectively stopping and starting fluid flow were approximately 4 mm.

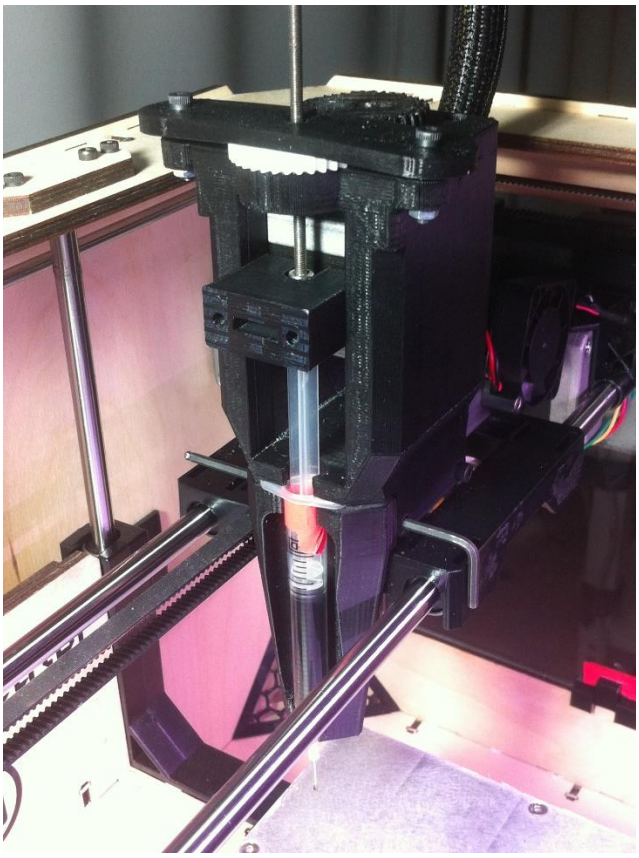

Figure 2.4 The Replistruder v1. The first iteration of the Replistruder shown above in ABS plastic, mounted on a MakerBot Replicator Dual 3D printer, utilized 3 mL plastic syringes and relied on a hinged breach-load mechanism for inserting and removing syringes full of ink. The mechanism was locked shut by a cross bolt (in this case an Allen wrench).

2.4.2 Design and Iteration of Replistruder v2

Replistruder v2 (Figure 2.5) utilized the 13:47 gearing mentioned in the methods above. The motor was also adapted with a heatsink at its back along with a fan and thermistor to ensure low temperature operation. It was possible to mount 2 of these extruders in parallel to one

another via a specialized mount, and 2 material printing was thus possible using this setup. Retraction values for this design were close to 2 mm. This version of the Replistruder was the first to factor in constant preload of the leadscrew to occupy potential slack in the transmission. The preload was accomplished by spring loading the leadscrew with two springs salvaged from abandoned inkjet printers. Also, this Replistruder utilized a "clutch" mechanism between the syringe plunger and leadscrew in order to ensure the two remained tightly coupled with no risk of the leadscrew rotating free of the syringe plunger.

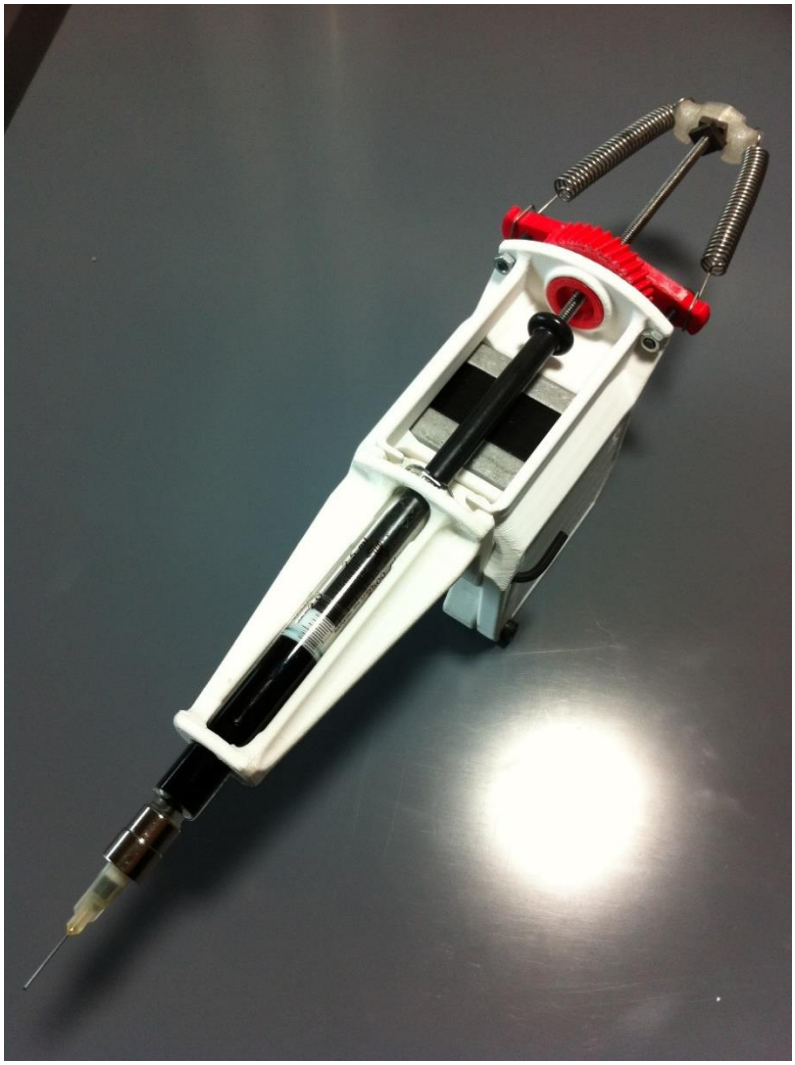

Figure 2.5 The Replistruder v2. The second iteration of the Replistruder shown above in white ABS plastic utilized 2.5 mL glass and metal syringes and relied on a hinged breach-load mechanism for inserting and removing syringes full of ink. The mechanism was locked shut by a cross bolt (in this case an allen wrench).

2.4.3 Design and Iteration of Replistruder v3

Replistruder v3 (Figure 2.6) traded the breach-loading hinged design for the overall stiffness of a monolithic, bolted set of stiff components. The pump was effectively redesigned with three goals in mind –to shed as much weight, gain as much stiffness as possible, and simultaneously maintain a low profile form factor. This version was also the first to utilize a flange-only grip on the syringe. Most of the work in the FRESH paper[30] was accomplished with this version. The retraction value for this design was approximately 0.1 mm of backward travel in order to halt extrusion using a ½-inch, 32 gauge stainless deposition tip (also known as a 150 µm nozzle) on a 2.5 mL syringe. This version of the Replistruder also featured a dual-extrusion mount allowing it to be used in pairs on the MakerBot Replicator Dual 3D printer.

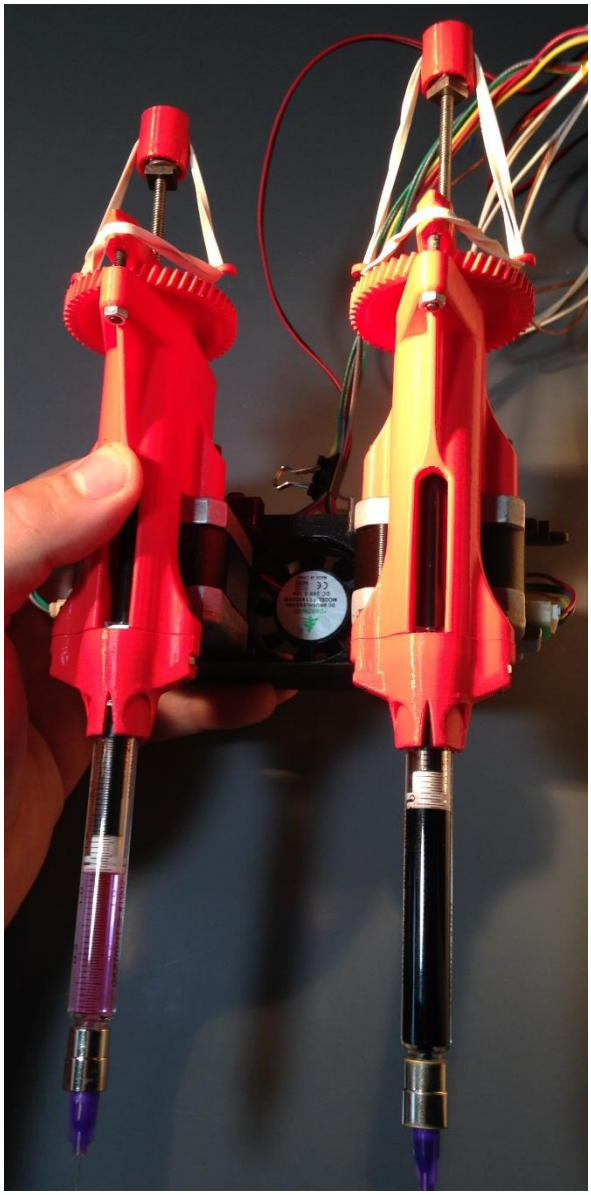

Figure 2.6 The Replistruder v3. The third iteration of the Replistruder shown above in red PLA plastic (in a dual configuration) utilized 2.5 mL glass and metal syringes and relied on bolting and unbolting portions of the pumps for inserting and removing syringes.

2.4.4 Design and Iteration of Replistruder v4

In response to operating v3, v4 (Figure 2.7A) was created in order to ease the laborious process of removing and re-installing syringes and to allow additional sizes of syringe to be used. V4 featured a simplified set of stiff core components forming the skeleton of the transmission, while a flexible exoskeletal armature could be either closed or opened around the entire core, engaging all operating components under slight compression or freeing each to rotate independently of the others, respectively. Essentially, v4's armature operated like a Keurig® machine's front handle, where opening was one direction and closing/operating was another direction. V4 was the first iteration to feature various adapters for different syringes, effectively making it a jack-of-all-trades/master-of-none design. This version of the Replistruder was also the first to use a pair of nuts on the leadscrew in order to eliminate slack in this part of the transmission. When the compression armature was in its open state, the paired nuts were free to separate, and the leadscrew was easily spun inside the large, 47-tooth gear. When the armature was closed around the Replistruder, the pair of nuts were placed in compression, and it became much more difficult to rotate the leadscrew due to the removal of slack between the nuts. V4's core was also designed with hidden internal defects to force 3D printing softwares to reinforce specific sections in a manner that is as strong as possible while maintaining overall simple form. This technique of subtly influencing overall part strength was also applied to the 47 tooth gear to create a radial spoke pattern of extrusions around the trapped pair of nuts inside. Examples of this technique are shown in Figure 2.7B & 2.7C. Finally, this design was also the first iteration to adopt a vice-based clutch coupler between the syringe plunger and leadscrew. After the leadscrew was threaded into the head of the syringe plunger, the "clutch" was tightened

down against the syringe plunger, securing the leadscrew to the plunger and eliminating any chance for decoupling. In hindsight, the tradeoff for using flexible adaptation to various syringes while maintaining a low profile and ease-of-use was the decrease in responsiveness. Retraction in this model was approximately 0.15 mm. Were it not for the pair of compressed nuts, this design would have likely been a failure, but it found use across the board in many different applications, allowing us to print a variety of inks in a variety of different syringes, glass, plastic, and metal.

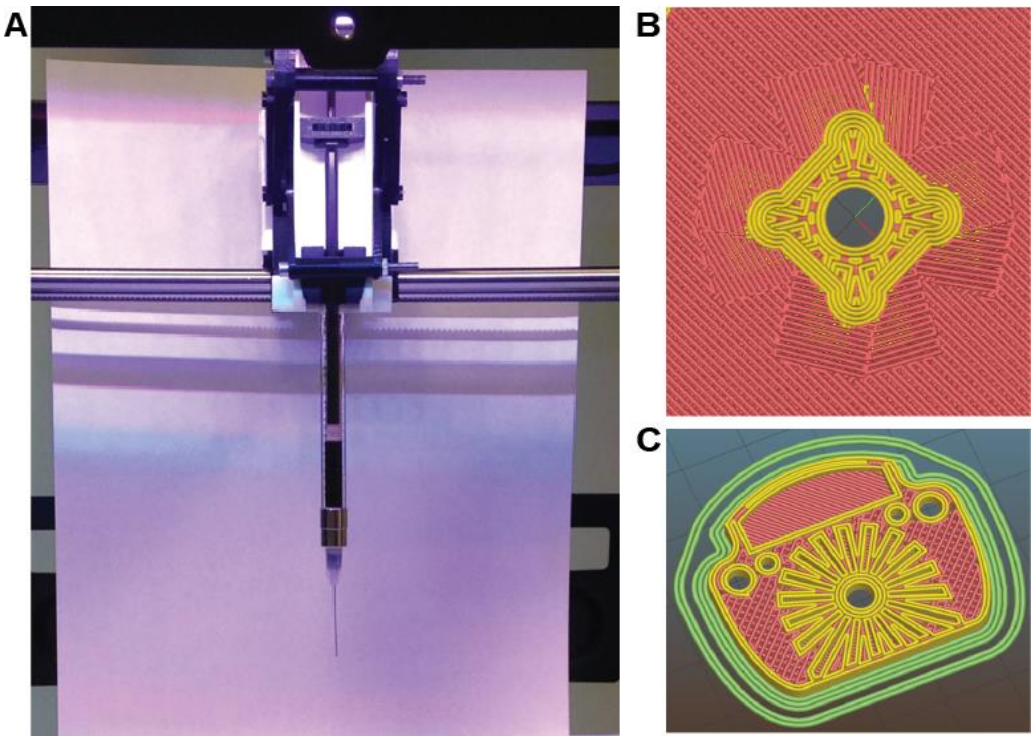

Figure 2.7 The Replistruder v4. (A) The fourth iteration of the Replistruder, shown above in white and black PLA plastic, utilized Hamilton syringes ranging from 100 µL to 10 mL and relied on a spring-loaded armature to hold the entire transmission in compression. Also, a clutch visible at the top of the syringe plunger removed the need for elastic preload on the leadscrew. **(B)** The central portion of the gear used to drive the leadscrew using a pair of nuts was designed to create strong paths in Gcode regardless of slicing program. The resulting pathing surrounding the square hole for the square nuts is shown. **(C)** The core of the Replistruder v4 was also provided with defects that would produce stronger pathing decisions in slicing software. Visible here are the paths surrounding the primary load bearing surface of the v4 core component, visible in (A) as a white plastic part.

2.4.5 Design and Iteration of Replistruder v5

Replistruder v5 was a redesign from the ground up in favor of the principles laid out in 2.3.1. The Replistruder v5 is a completely stiff iteration, weighing more than any other iteration. Rounded corners make it a pleasure to hold compared to previous designs such as the v4 and v3. The simple approach to v5 makes it easier to understand its operation while concealing design aspects that make it function particularly well compared to the other designs – approximate retraction values are near 0.05 mm, making it the most responsive design yet. For any syringe 10 mL or less in volume, a custom bottom plate holds the syringe using a vice mechanism. The entire Replistruder can be removed from the printer and placed in storage by removing two bolts accessed from the front face. To protect the user and the syringe, a centrifuge tube can be secured over the syringe and needle. The transmission is intended to require zero adjustment after assembly, making it the most hands-off Replistruder iteration yet. The total number of nuts and bolts in this design is less than any other design. Zero units have broken since this iteration was rolled out across several different printers. This lack of mechanical failure is a huge improvement over the v4 which experienced tens of armature failures.

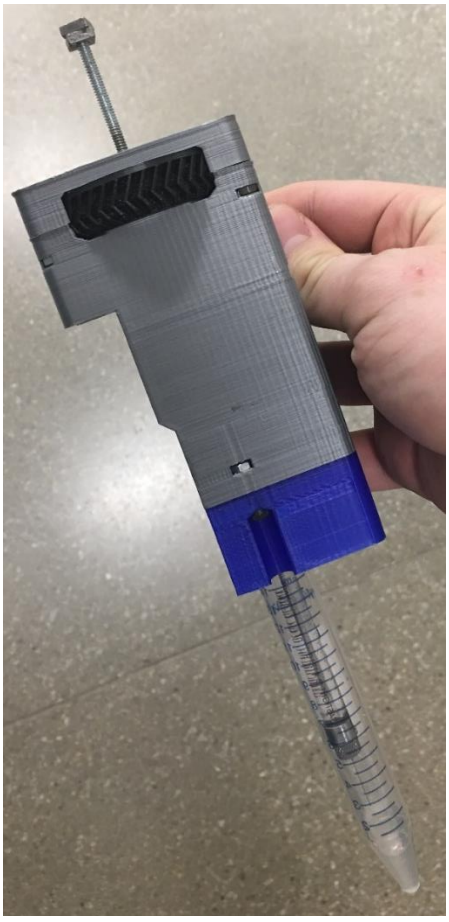

Figure 2.8 The Replistruder v5. The fifth and current iteration of the Replistruder shown above in grey and blue PLA plastic utilizes Hamilton syringes ranging from 100 µL to 10 mL and relies on bolting and unbolting components to access the syringe. A 15 mL tube is fitted over the syringe and needle during storage to protect the user and syringe. This entire syringe is stored in this configuration.

2.5 Conclusion

In this chapter, we demonstrated the creation of a 3D printable extruder designed to function as an extruder on a consumer 3D printer with subtle firmware and hardware modifications. The resulting platform utilizes open source hardware and softwares to operate in a manner closely resembling FDM and paralleling it in operational theory. In the next chapter, it is shown that the custom printer enables printing of multiple fluids through this modification. Iterations on these modifications are shown to improve the system's overall responsiveness through a subtle decrease on required retraction values. Finally, the challenges unique to this modified hardware platform are elucidated and explained. These efforts have enabled colleagues such as Andrew Lee, Andrew Hudson, Hao Jan Shue, Josh Tashman, Neeha Dev-Arun, Joon Hyung-Park, Martin Grodzicki, Songyang Li, Sara Abdollahi, Kira Pusch, and many others in labs across the world to 3D print with fluids. Their greater volume of work will always mean more than mine ever can, and it is important that I have continued to iterate upon this printing platform that enriches so many efforts.

Chapter 3 3D Printing Hydrogels with Complex Architecture Based on Tomographic Data and Parametric CAD Design

3.1 Abstract

Much of the complex biochemistry found in the extracellular matrix can be preserved after removing cells in processes such as decellularization with surfactants, and this set of chemical and physical instructions can be repurposed as a living scaffold for seeded cells. After re-seeding the decellularized tissue, the resulting construct often partially mimics the starting collection of tissues in form and function. To date, decellularized ECM represents the gold standard hydrogel for producing biomimetic, living tissue in vitro; however, it is impossible create these delicately templated substrates without sacrificing live tissue. 3D bioprinting is the closest engineering has come to developing thick hydrogel constructs with manufactured architectures; and yet, until 2015, there was no 3D bioprinting method that was compatible with the vast majority of endogenous ECM hydrogels[30]. Consequently, previous bioprinting techniques had focused on printing purely cells or post processing more-easily printed materials into ECM[15,32,51,57].

We describe in this chapter how we discovered and introduced a novel technique to 3D print unmodified ECM hydrogels. We characterized the operating parameters of the printing process on hardware described in the previous chapter. Optimization of materials and software settings is shown to lead to higher quality results, and the addition of multiple materials to the printing process proves to be a linear extension of the overall system which is already supported

by the utilized softwares. To ensure the consistent behavior of the process, the development of high-performance, non-Newtonian fluids and methods for creating these at scale is factored in. We show the successful fabrication of various 3D shapes that are classically difficult to additively manufacture. Some of the shapes demonstrate functional forms. Other shapes demonstrate levels of detail that are beyond the scope of traditional desktop FDM. All outcomes in this chapter were dependent on open source softwares and hardwares.

3.2 Introduction

Over the past decade, the additive manufacturing (AM) of biomaterials has gone from a rapid prototyping tool used in research and development and transitioned into a viable approach for the manufacturing of patient-specific medical devices. Key to this is the ability to precisely control structure and material properties in 3D and tailor these to unique anatomical and physiological criteria based on CT and MRI medical imaging data. First-in-human applications include customized polyetherketoneketone bone plates for the repair of large cranial and polycaprolactone bioresorbable tracheal splints for pediatric applications[24,65,73]. The enabling 3D printing technologies are based primarily on selective laser sintering (SLS) of metal, ceramic or thermoplastic microparticles, fused deposition modeling (FDM) of thermoplastics or photopolymerization of photosensitive polymer resins and have tremendous growth potential for surgical and medical devices and scaffolds for tissue repair[3,18,26,41,69]. However, these approaches are limited in their ability to 3D print very soft materials such as elastomers, gels, and hydrogels that are integral components of many medical devices and are required for most future applications in tissue engineering and regenerative medicine[49,54]. Specifically, biological

hydrogels composed of polysaccharides and/or proteins are a class of materials that are challenging to 3D print because they must be gelled in situ during the fabrication process and then supported so they do not collapse or deform under their own weight. While the need for support materials is common across many AM techniques, it is a particularly difficult for these soft biological hydrogels, where the elastic modulus is <100 kPa and there is a narrow range of thermal, mechanical, and chemical conditions that must be met to prevent damage to the materials and potentially integrated cells.

Current approaches for the 3D printing of biological hydrogels have achieved important advances, but are still in need of significant improvement[54]. For example, syringe-based extrusion has been used to 3D print polydimethylsiloxane (PDMS) elastomer and alginate hydrogel into multiple biological structures including the ear and aortic heart valve[20,32,45]. Other research teams have demonstrated the direct bioprinting of fibrin, gelatin and mixtures of proteins derived from decellularized tissues or cast ECM gels around dissolvable templates[17,39,43,51,62]. These results have expanded the range of materials that can be used and demonstrated the ability to incorporate and print live cells. There are also commercially available bioprinters from Organovo (20-22) and EnvisionTEC (7, 23) that have expanded the accessibility of bioprinters beyond the groups that custom build their own systems[41,47,56]. However, the complexity of microstructure and 3D anisotropy that can be created are still limited, often the structures printed are simple square lattices called woodpiles, similar to stacked Lincoln logs, which does not recapitulate the microstructure of real tissues.

As a field, significant improvements are still needed in terms of the ability to directly manufacture using biologically relevant hydrogels, controlling microstructure and anisotropy in

3D, and expanding biological AM research by driving down the cost of entry while increasing quality and fidelity of the printing process. Our goal was to specifically address five major challenges including (i) deposition and crosslinking of soft biomaterials and viscous fluids with elastic moduli of <100 kPa, (ii) supporting these soft structures as they are printed so they do not collapse or deform, (iii) depositing the material anisotropically to match the microstructure of real tissue, (iv) removing any support material that is used, and (v) keeping cells alive during this whole process using aqueous environments that are pH, ionic, temperature and sterility controlled within tight tolerances [50,60,68].

Even assuming a method capable of these goals existed or was in the process of being invented, the above would still present a challenge without first attempting to control for cost, machine variation, material variety, software performance, and dependability of protocols. Iteration in any rapid prototyping process can quickly become expensive without careful selection of material use constraints. We selected materials and the methods for handling them that preserved as much consumable resources as possible while still allowing rapid and inexpensive iteration. We chose machines that accept interchangeable dialects of Gcode machine instruction sets and modified them to accept one set of materials in the 3D printing process. We show that it is possible to reliably produce effective printing results using a variety of different softwares – namely all major packages used for consumer and enthusiast FDM. Reliable protocols were established through brute force iterative elimination of stray confounding factors. A rock-solid hardware foundation for meeting the above five challenges was constructed and outlined in Chapter 2 of this dissertation. Material, software, and protocol choices form part of the discussion in this chapter.

Additionally, we decided to meet a challenge that was not inherently part of "printing" gels in 3D – creating biomimetic protein hydrogel constructs that retain their geometry through handling and various strains applied during culture. Any object made from endogenous hydrogels such as collagen and fibrin possesses inherent fragility. On top of that, 3D printed objects are weaker than monolithic equivalents. Therefore, additively manufacturing fragile materials results in objects that are delicate even by tissue engineering standards – most objects cannot be handled outside of a fluid solution because they collapse under their own weight. To get around this problem, it's possible to cast some materials in a rigid, sacrificial material for transport or handling. We explored a similar theme of preserving soft structures with stiff encapsulation by utilizing a secondary, stiffer alginate hydrogel ink to reinforce collagen hydrogel structures in any given print. We show that these multi-material, multi-component constructs survive handling and culture conditions without suffering deformation. We can even remove the secondary alginate extrusions without disturbing the collagen. Our approach borrows heavily from printing multiple materials in FDM; therefore, we show a simple, fool-proof method for creating these "stabilized" constructs using open FDM software tools.

We demonstrate the additive manufacturing of complex 3D biological structures using soft, protein, and polysaccharide hydrogels that are challenging or impossible to create using traditional fabrication approaches. These structures are built by embedding the printed hydrogel within a secondary hydrogel slurry that serves as a temporary, thermoreversible and biocompatible support. This process, termed freeform reversible embedding of suspended hydrogels (FRESH), enables 3D printing of hydrated materials with an elastic modulus <200 kPa including alginate, collagen, and fibrin, based on CAD models of 3D optical, CT, and MRI imaging

data at a resolution of ~200 µm. Proof-of-concept structures include femurs, branched coronary arteries, trabeculated embryonic hearts, adult human hearts, mammary ductal epithelia, and human brains that are anatomically accurate, mechanically robust, and recreate complex 3D internal and external architectures with high-fidelity and at low cost.

3.3 Materials & Methods

3.3.1 Creation of FRESH and Gelatin Slurries

As part of my Master's degree, FRESH was invented to solve printing of fluid gels in 3D. The process went as such: several different non-Newtonian fluids were tested for their ability to prop up a submerged extrusion of alginate hydrogel and whether or not that hydrogel could be additively fused to subsequent extrusions. The tested fluids included gelatin foams, hydrated gelatin powder (slurry), and a gelatin slurry produced by physically forcing gelatin gels through small orifices. It was quickly evident that a slurry of gelatin gels was the best answer, so various means to create these gels were explored.

To create the gelatin slurry support bath, 150 mL of 4.5% w/v Gelatin (Type A, Thermo Fisher Scientific) in 11 mM $CaCl_2$ (Sigma-Aldrich) was mixed into a solution and then gelled for 12 hrs at 4°C in a 500 mL mason jar (Ball Inc.). Next, 350 mL of 11 mM $CaCl_2$ at 4°C was added to the jar and its contents were blended (at "pulse" speed) for a period of 30 to 120 s on a consumer-grade blender (Osterizer MFG) (Figure 3.1A). Then, the blended gelatin slurry was loaded into 50 mL conical tubes (Figure 3.1B) and centrifuged at 4,200 RPM for 2 min, causing slurry particles to settle out of suspension (Figure 3.1C). Supernatant was removed and replaced with 11 mM $CaCl_2$ at 4°C. The slurry was vortexed back into suspension and centrifuged again. This process was

repeated until no bubbles were observed at the top of the supernatant, which indicated most of the soluble gelatin was removed. At this point, gelatin slurries could be stored at 4°C. For FRESH printing, the slurry was poured into a Petri dish or container large enough to hold the object to be printed (Figure 3.1D). Any excess fluid was removed from the gelatin slurry support bath using Kimwipes (Kimberly-Clark), which produced a slurry material that behaved as a Bingham plastic. All 3D printing was performed using gelatin blended for 120 s.

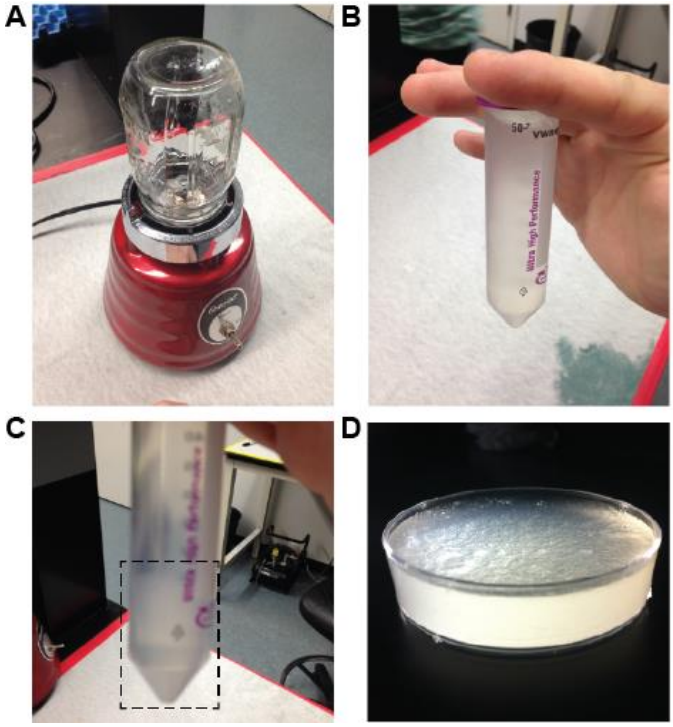

Figure 3.1 Preparation of a blended gelatin slurry support bath. (A) The blender with a 500 mL mason jar attached, which is used to create the microparticulate slurries from solid gelatin blocks. **(B)** A 50 mL centrifuge filled with the blended gelatin slurry before suspended particles are separated from the supernatant by centrifugation. **(C)** The blended gelatin solution after centrifugation showing settled gelatin slurry at bottom and supernatant on top. **(D)** A 35 mm petri dish filled with the gelatin slurry for use in FRESH printing, showing the bath after the supernatant has been removed and excess water has been wicked off using Kim wipes.

To measure the effect of blend time on gelatin particle size, the gelatin was blended for periods of time of 30, 45, 60, 75, 90, 105, 120 s. Blend times of greater than 120 s were not used

because the gelatin particles began to dissolve entirely into solution. For each blend time analyzed, 500 µL of slurry was removed and diluted to 10 mL with 11 mM CaCl2 and 0.1% w/v black food coloring (McCormick & Co.). Then, 140 µL of each diluted sample was mounted on a coverslip and imaged with a digital camera (D7000 SLR, Nikon) mounted on a stereomicroscope with oblique illumination (SMZ1000, Nikon). For each image, ImageJ (National Institutes of Health) was used to enhance contrast, convert to LAB color space, and apply a lightness threshold. ImageJ was then was used to count particles and measure their Feret diameters, areas, and circumferences using the "analyze particle" function[64]. Linear regression of particle diameter as a function of time was performed using SigmaPlot 11 (Systat Software, Inc.).

To measure the rheological properties of the gelatin slurry support bath, the gelatin was blended for 120 s and then prepared as described for the FRESH 3D printing process. The slurry was loaded onto a Gemini 200 Rheometer with a 40 mm, 4° cone (Malvern) and analyzed in frequency sweep from 0.001 to 100 Hz at 150 µm separation and 25°C. The storage (G') and loss (G'') moduli were measured and recorded in Microsoft Excel and plotted using SigmaPlot 11.

In order to create slurries with lower polydispersity, smaller particles, and higher overall performance in FRESH, coacervation of gelatin particles from ethanol-water solutions was used. A solution of 2% w/v gelatin type B (Sigma) and 0.25% w/v F127 Pluronic (Sigma) in 1:1 EtOH:dH_2O was warmed to 40°C, allowing all gelatin and Pluronic to dissolve. The pH of the solution was then adjusted to ~5.65 before removing heat and allowing to cool to room temperature under 500 rpm stirring using an overhead stirrer fitted with a Rushton Turbine. Special care was taken to avoid stirring air into the solution. Approximately 8 hours later, the coacervate was removed from the mixing vessel and centrifuged at 2 minutes under 175 xg.

Supernatant was removed, and the coacervate pellet was resuspended in dH_2O. Then, centrifugation for 2 minutes at 225 xg followed by resuspension of the pellet in 1X PBS with 25 mM Na-HEPES. Then, centrifugation for 2 minutes at 450 xg followed by resuspension in more 1X PBS with 25 mM HEPES. This last step is repeated three times. Final centrifugation was 5 minutes at 750 xg, and the supernatant was discarded before the resulting slurry was dispensed into containers for FRESH printing.

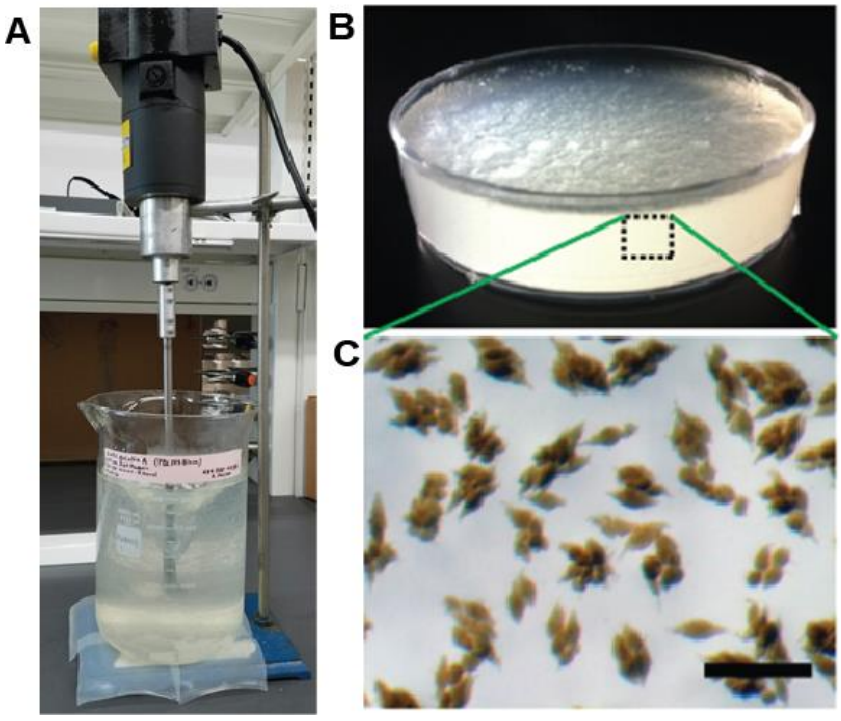

Figure 3.2 Preparation of a coacervate gelatin slurry support bath. (A) An overhead stirrer is used to maintain a 40°C mixture of gelatin solution and ethanol until it cools to room temperature **(B)** The slurry that results from the coacervation has a nearly identical appearance to previous, physically blended slurries. **(C)** Slurry particles possess a spindle geometry when viewed under magnification. Scale bar: 100 µm.

3.3.2 Identifying Differences Between FDM and FRESH

Early on when 3D printing using FRESH, it was decided to try and follow the theoretical framework utilized for plastic 3D printers. The theory outlines that a given volume of plastic was

required to create an extrusion occupying a programmed path. This volume was approximated per the path traveled by the extruder in any given extrusion, and it was written into the Gcode as distance along an E axis. Thus, a given distance of plastic filament was extruded in the E axis to push the necessary volume of plastic for the intended extrusion on the print. Since the firmwares on our printers were modified to actuate millimeters of a Replistruder's leadscrew instead of millimeters of plastic filament, we had to make some changes to account for the difference between a 7 mm diameter syringe plunger and a 1.75 mm plastic filament. We wanted the printers to think they were still pushing plastic filament. Luckily, slicing software packages offer the ability to enter a fixed filament diameter which is then used to calculate the E axis distance necessary to extrude a given volume of plastic. Therefore, we simply entered the diameter of our syringe plunger, and the software accounted for the difference.

Once it was discovered that we could operate our printers under the constraints of desktop FDM by the clever simplification detailed above, we set about attempting various geometries looking for failure modes. By definition, no overhang exists in FRESH printing, as all printed structures are, in theory, supported by the yield-stress behavior of the support material. Instead of trying to print delicate structures that befuddle desktop FDM, we first attempted to print monolithic objects with carefully designed aspects intended to illuminate the possible failure modes suspected for FRESH.

3.3.3 The FRESH 3D Printing Process

As summarized below in Figure 3.3, STL files were processed by Slic3r (slic3r.org), MatterControl (mattercontrol.com), Cura (ultimaker.com/en/products/cura-software),

Simplify3D (simplify3d.com), Skeinforge (fabmetheus.crsndoo.com), or KISSlicer (kisslicer.com) software and sliced into 60 - 80 µm thick layers to generate G-code instructions for the 3D printer. G-code instruction sets were sent to printers using ReplicatorG (replicat.org), Pronterface (pronterface.com), Repetier Host (repetier.com), SD card, Simplify3D, MatterControl, or the Duet Web Interface (github.com/chrishamm/DuetWebControl). Practically all of these softwares utilize the same drivers provided by the Arduino Foundation (arduino.com) to communicate with the 3D printers, which are all built upon Atmel processors (atmel.com).

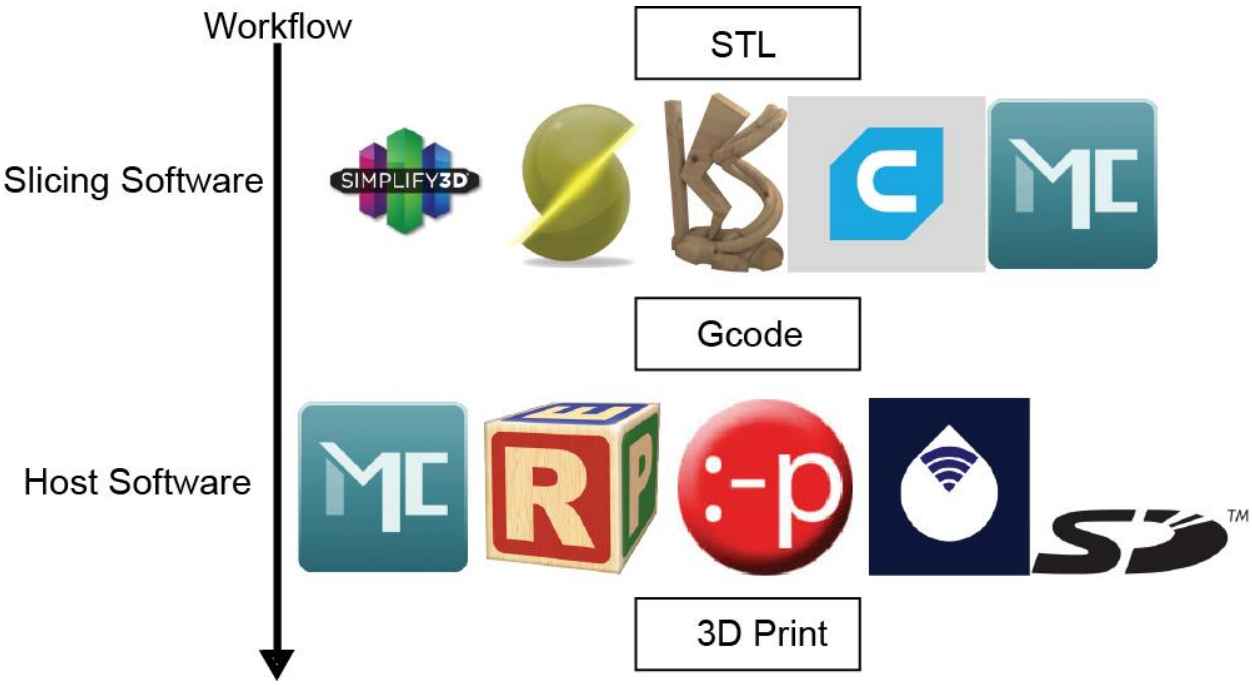

Figure 3.3 Digital Workflow for Processing STL Files into 3D Prints. Files start as STL, are sent to slicing softwares which turn them into Gcode. Gcode is then sent via host softwares to a 3D printer which in turn creates the 3D Print.

To perform FRESH printing, hydrogel precursor inks were first drawn into a 2.5 mL syringe (model 1001 Gastight Syringe, Hamilton Company) with a 150 µm-ID ½ in long stainless steel deposition tip needle (McMaster-Carr) used as the nozzle. The syringe was then mounted into the syringe pump extruder on the 3D printer (Figure 3.3.1). A petri dish or similar container large

enough to hold the part to be printed was filled with the gelatin slurry support bath and manually placed on the build platform, and the container was held in place using a thin layer of silicone grease. The tip of the syringe needle was positioned at the center of the support bath in X and Y and near the bottom of the bath in Z before executing the G-code instructions. Scaffolds were printed at 20°C over a period of 1 min to 4 hours depending on the size and complexity of the printed construct as well as the ink used. For cellularized constructs, sterility was maintained by printing in a biosafety cabinet. In order to liquefy the support bath and release a print after FRESH, embedded constructs were heated to 37°C directly on the printer's platform, placed on a dry bath, or placed inside an incubator. Once the gelatin was melted, alginate prints were rinsed with 11mM CaCl2 and stored at 4°C. Once the gelatin was melted for collagen and fibrin prints, the objects were rinsed with 1X PBS and stored at 4°C. For multi-component ECM prints seeded with cells (discussed in Chapter 4), scaffolds were rinsed with the appropriate culture medium based on the incorporated cell types and incubated at 37°C before seeding.

Multi-material constructs detailed in section 4.3 and consisting of two separate files, were loaded into Slic3r and processed for printing. The outer blocks of each print were printed from alginate extrusions roughly 150 µm in width, and the inner funnel-with-drumstick shapes were printed from 80 µm-wide collagen type I extrusions. After these multi-material prints were completed, they were dissected, and collagen portions of the prints were removed using forceps.

3.3.4 Design and Testing of Benchmark Geometries with Slicing Softwares

A benchmark solid featuring a hollow interior with sharp corners, narrow pillars, and a traditional "overhang" with a flat roof was designed. This shape was called the Elliptical Window

Calibration or EWC. Print perimeters were varied between none and 10. The infill percent was varied between 0 and 100%. Based on observations and the identified "crowning artifact" discussed in Section 3.4, we then tried to print various layer heights with various flow rate modifiers. Layer height varied between 30 and 50% of the nozzle diameter. Then, flow tweak was adjusted between 0.4 and 1.0, effectively allowing for as little as 40% and as much as 100% of the theoretical value for extrusion necessary to render a given extrusion.

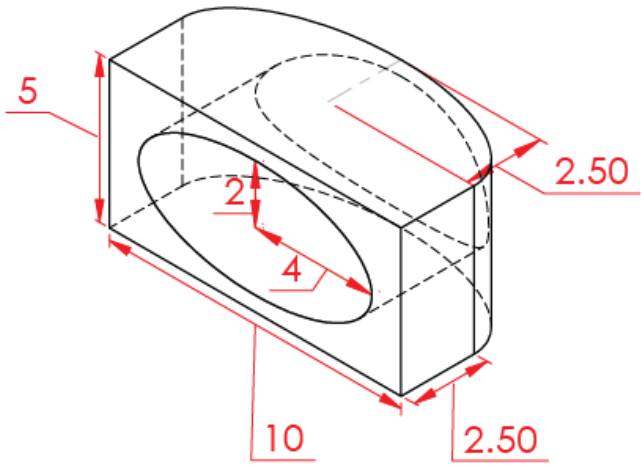

Figure 3.4 Elliptical Window Calibration. The Elliptical Window Calibration pictured here with dimensions in mm is the most commonly used file for benchmarking FRESH printing. The10 mm wide by 5 mm long by 5 mm tall print features a 2 x 4 mm elliptical hole cut through its front face. Additionally, the back face is beveled with a 2.5 x 5 mm elliptical fillet on each side.

After the EWC benchmark was utilized to identify several working settings, a separate benchmark incorporating more complex and desirable features (for bioprinting) was created to test the abilities of slicing software packages. Before designing this second benchmark, brainstorming was used to assemble artifacts present in FDM prints as well as those unique to FRESH. The artifacts chosen were: crowning, narrow corners, vertical points, thin walls, infill gaps, diffusion of gelling ink, unfused layers, oozing of extruders, and mechanical resonance in a printer. The resulting benchmark called the snail calibration, detailed below in Figure 3.8 , was

utilized to compare various slicing software packages in a kind of torture test intended to highlight the failings of each package. Each software package was set up with what were approximately equivalent settings, and the resulting Gcode output from each package was loaded into Repetier Host software for visualization and comparison. The softwares were set to render the Snail Calibration with 1 perimeter, and 70% infill using 60 µm layers.

3.3.5 Formulation of Inks for FRESH Printing

To prepare fluorescently-labeled alginate for 3D printing, a solution of 2.0% w/v sodium alginate (FMC Biopolymer), 0.02% w/v 6-aminofluorescein (FITC, Sigma), 0.022% w/v 1-Ethyl-3-(3Dimethylaminopropyl)carbodiimide (EDC, Sigma) and 0.025% w/v Sulfo-N-Hydroxysuccinimide (NHS, Sigma) in distilled water was prepared and stirred for 48 hrs at 20°C. Unreacted FITC was removed from FITC-labeled alginate by five consecutive 12 hrs dialysis shifts against 2% w/v sodium alginate at 4°C in dialysis cassettes (Slide-A-Lyzer 3.5k MWCO, Thermo Fisher). After dialysis, 100 µL of FITC-labeled alginate was added to 10 mL solution of 4% w/v sodium alginate, 0.4% w/v hyaluronic acid (Sigma), and 0.1% w/v black food coloring (for visualization during printing) to create a fluorescently labeled alginate ink. Alginate inks used in dual material prints described later were exclusively 4% w/v in dH_2O. Fluorescent alginate prints were imaged using a Leica SP5 multiphoton microscope with a 10x (NA = 0.4) objective and a 25x (NA=0.95) water immersion objective. Higher magnification images were obtained using a Zeiss LSM700 confocal microscope with a 63x (NA = 1.4) oil immersion objective. Bi-material prints and arterial tree prints were imaged using a Nikon AZ-C2 macro confocal microscope with a 1x (NA = 0.1)

objective. 3D image stacks were deconvolved with AutoQuant X3 and processed with Imaris 7.5 (Bitplane Inc.).

To prepare fibrinogen for 3D printing of fibrin constructs, a solution of 10 mg/mL fibrinogen (VWR), 0.5% w/v hyaluronic acid (Sigma), 1% w/v bovine serum albumin (Sigma), 10 mM sodium-HEPES (Sigma), and 1X PBS (VWR) was prepared and loaded into a syringe for printing. To ensure crosslinking of the fibrinogen into fibrin once printed in the support bath, the baths were supplemented with 0.1 U/mL thrombin (VWR). Fibrinogen prints were released from bath material by incubation at 37°C for at least 1 hour.

For some instances of 3D printing of collagen, rat tail collagen type I (BD Biosciences) at concentrations ranging from 8.94 to 9.64 mg/mL in 0.02 N acetic acid was used as received without further modification. To ensure crosslinking of collagen into a gel following extrusion, the support bath was supplemented with 10 mM HEPES to maintain a pH of ~7.4 and neutralize the acetic acid. After printing, scaffolds were incubated at 37°C for at least 1 hour to further crosslink the collagen and melt the support bath. In other cases, LifeInk 200 (Bovine Collagen type I; Advanced Biomatrix) was diluted from 35 mg/mL to 24 mg/mL in a 0.04 N Acetic Acid solution and used in place of rat tail collagen, and the bath was supplemented with 25 mM Na-HEPES.

3.3.6 Cell Culture and Fluorescent Staining for Testing Cytocompatibility of FRESH

All reagents were purchased from Life Technologies unless otherwise specified. The MC3T3-E1.4 fibroblast cell line and prints containing MC3T3 cells (CRL-2593, ATCC) were cultured in α-MEM supplemented with 10% fetal bovine serum (FBS, Gibco Labs), penicillin (100 units/mL),

and streptomycin (100 µg/mL). The C2C12 myoblast cell line and prints containing C2C12 cells (CRL-1722, ATCC) were cultured at 37°C under 5% CO2 in Dulbecco's Modified Eagle Medium supplemented with 10% v/v FBS, 1% v/v L-glutamine (200 mM), penicillin (100 units/mL), and streptomycin (100 µg/mL), based on published methods (3).

Cell viability after FRESH printing was assessed by performing a LIVE/DEAD assay (Life Technologies) on prints containing C2C12 cells. Each print was first washed with Opti-MEM media containing 2% FBS and 2% 10,000-unit penicillin-streptomycin solution and incubated at 37°C under 5% CO2 for 30 min. The prints were then removed from the incubator, rinsed with 1X PBS, incubated in 2 mL of PBS with 2 µL of calcein AM and 4 µL of ethidium homodimer per sample for 30 min and then imaged on a Zeiss LSM 700 confocal microscope. The number of live and dead cells in each of 5 images per 3 independent samples were counted and the percent viability was calculated by dividing the number of live cells by the number of total cells per image.

Prints containing cells were cultured for up to 7 days and analyzed at 1 and 7 day time points to verify cell survival and growth. After 1 and 7 days of culture, printed sheets were rinsed with 1X PBS (supplemented with 0.625 mM MgCl2 and 0.109 mM CaCl2) at 37°C, fixed in 4% w/v formaldehyde (Polysciences, Inc.) for 15 min, and then washed 3 times in 1X PBS. Fixed prints were incubated for 12 hrs in a 1:200 dilution of DAPI (Life Technologies) and 3:200 dilution of Phalloidin conjugated to Alexa-Flour 488 (Life Technologies). Prints were then washed three times in PBS and mounted with Prolong Gold antifade reagent (Life Technologies) between a microscope glass slide and a N1.5 glass cover slip. The mounted samples were stored at room temperature and protected from light for 12 hrs to allow the Prolong reagent to cure. Prints were imaged using a Leica SP5 multiphoton microscope with a 10x (NA = 0.4) objective and a 25x

(NA=0.95) water immersion objective. 3D image stacks were deconvolved with AutoQuant X3 and processed with Imaris 7.5.

3.3.7 Perfusion of 3D printed Coronary Arterial Tree

To evaluate whether the 3D printed arterial tree was manifold, it was mounted in a custom-made 3D printed perfusion fixture (Figure 3.5). A solution of 11 mM CaCl2 (Sigma) and 0.1 % w/v black food coloring was injected into the root of the tree using a standard 3 mL syringe (BD Biosciences) with a 150 µm-ID 0.5 in needle and the tip at the end of each branch was cut off to permit outflow. Perfusion was captured with a digital camera (D7000 SLR, Nikon) mounted on a stereomicroscope with oblique illumination (SMZ1000, Nikon).

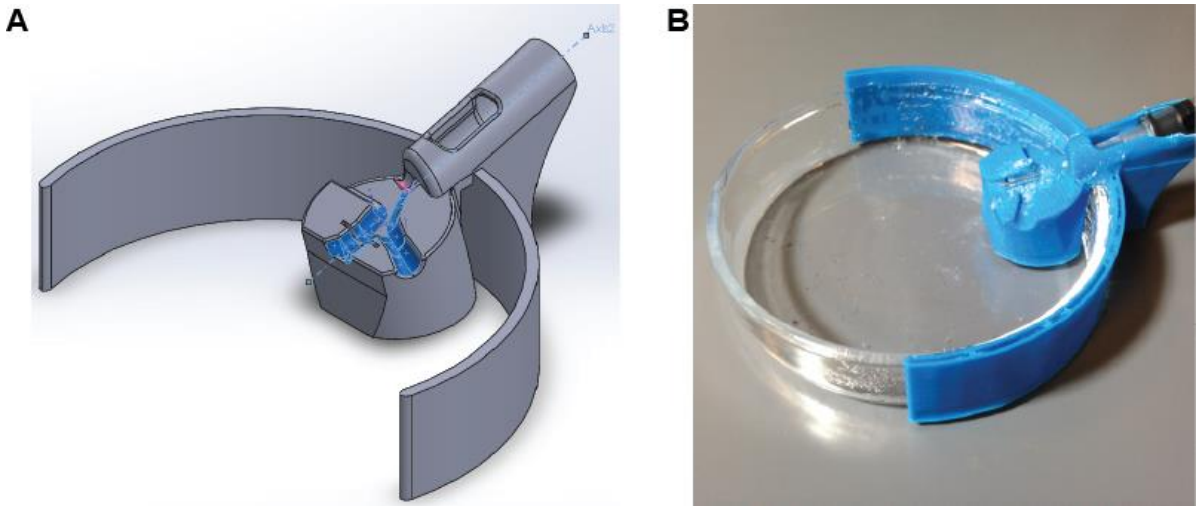

Figure 3.5 A 3D printed perfusion fixture for a FRESH-printed right coronary arterial tree. (A) A 3D CAD model of the perfusion fixture with the arterial saddle (recessed grooves) shown in blue. **(B)** An example of the perfusion fixture 3D printed using PLA and positioned on a Petri dish. The syringe tip used for perfusion into the trunk of the arterial tree is visible on the right

3.3.8 Software Processing of Image Data into 3D Printable Files

Digital 3D models for FRESH prints were created using 3D imaging data or designed using SolidWorks software (Dassault Systèmes). The files for the human femur, human heart, and coronary artery tree were downloaded from the BodyParts3D database[53]. The model of the human brain was provided under creative commons licensing by Andy Millns (Inition Co). The 3D digital models were opened in MeshLab (http://meshlab.sourceforge.net/) to be exported in the STL file format. For the 3D model of the coronary artery tree, only the outer surface was provided by the BodyParts3D database, so the arterial tree was resampled to create a smaller daughter surface with inverted normals. When both surfaces were combined, a hollow model with internal and external surfaces with a wall thickness of ~1 mm resulted, which was exported as an STL file for printing.

The 3D model of the embryonic chick heart was generated from 3D optical imaging data of a fluorescently labeled 5-day-old heart. To do this, White Leghorn chicken fertilized eggs were incubated at 37°C and 50% humidity for 5 days. Then the embryo (Hamburger-Hamilton Stage 27-28 (4)) was explanted and the heart (ventricles, atria and outflow tract) was dissected and fixed for 15 min in PBS with calcium, magnesium and 4% formaldehyde. After washing in PBS, the heart was blocked and permeabilized for 2 hrs at 37°C in PBS with 0.1% Triton X-100 and 5% goat serum. Two steps of immunostaining were carried out overnight at 4°C. The first stain used dilutions of 1:200 DAPI, 3:100 Phalloidin conjugated to Alexa Fluor 633 (Life Technologies) and 1:100 anti-fibronectin primary antibody (mouse, Sigma-Aldrich). After extensive washing in PBS, the samples were stained with a 1:100 dilution of goat anti-mouse secondary antibody conjugated to Alexa Fluor 546 (Life Technologies). Samples were then washed and dehydrated

by immersion in successive solutions of PBS with an increasing concentration of isopropyl alcohol as described previously[69]. Finally, the samples were cleared by transferring to a solution of 1:2 benzyl alcohol to benzyl benzoate (BABB) to match the refractive index of the tissue. The transparent sample was mounted in BABB and imaged with a Nikon AZ-C2 macro confocal microscope with a 5x objective (0.45 NA).

The 3D image stack was deconvolved using AutoQuant X3 and processed with Imaris 7.5, MATLAB (MathWorks), and ImageJ. The DAPI, actin, and fibronectin channels were merged to obtain an image with simultaneously well-defined trabeculae and outer wall of the heart. A detailed mask of the heart showing the trabeculae was created by segmenting the averaged signals using a high-pass threshold. A rough mask showing the bulk of the heart was obtained using a low-pass threshold. Next, the Imaris "Distance Transform" XTension was used on the bulk mask to create a closed shell of the outer wall of the heart. The high detail mask and the mask of the closed shell were combined to get a complex model of the heart with detailed trabeculae and a completely closed outer wall. The final model was smoothed and segmented using Imaris to preserve a level of detail adequate for 3D printing. A 3D solid object was created by exporting the smoothed model as an STL file using the Imaris XT module and the "Surfaces to STL" Xtension for MATLAB.

3.3.9 Multi-Material and Reinforced FRESH

STL files of target structures were imported into 3D Builder (Microsoft), "settled", centered at (X = 0, Y = 0), measured in X, Y, and Z, and exported as binary STL. Solidworks was used to generate a rectangular prism STL file with the same dimensions in X, Y, and Z as the

settled STL file of the target structure. Then, both STL files were imported into Meshlab, and the complex structure file had its surface normals inverted. The resulting stack of layers was collapsed to one layer, and the single layer was exported as a binary STL representing the area around the target structure to be made of sparse mesh extrusion.

To generate the Gcode for printing a multi-material reinforced FRESH print, both the target and mesh STL's were imported in Slic3r as separate "parts" with separately assigned extruders. The settings utilized for each solid as well as for the printer and inks are outlined in Appendix B.

Printing multiple materials required that the idling extruder nozzle be submerged in a solution to prevent the nozzle from drying and clogging. Petri dishes (100 mm, VWR) were filled with solutions of 0.1% w/v Pluronic F127 and placed to either side of the printing container on the print platform. The printing container was filled with a support material having a fluid phase of 11 mM $CaCl_2$ and 25 mM Na-HEPES solution. Nozzles were aligned per the protocol in section 2.3.7 of this document. Printing was initiated by uploading the Gcode to the Duet based printer using its web interface and selecting that Gcode for execution.

3.4 Results & Discussion

3.4.1 FRESH Required Calibration of Select Settings

The following settings (Table 3.4.1) were found to reliably print EWC's using 4% w/v alginate in a support bath created using physical comminution or blending. These settings were derived from hundreds of EWC prints executed using ReplicatorG and Skeinforge 3D printing softwares.

Variable name	Value
layer height	0.06 mm
extrusion width	0.15 mm
feed rate	23 mm/s
infill %	35 %
% infill/perimeter overlap	55 %
# of perimeters	2
z lift	0.15 mm
travel feed rate	200 mm/s
combing	Yes
order of paths	Inset perimeters > External perimeter > Infill
retraction	0.075 mm
flow rate multiplier	0.6

Table 3.1Settings used to print EWC's reliably. For all printers used during the calibration processes at the beginning of understanding FRESH, these settings represented the mean values with which EWC's were reliably printed. Variables had various nomenclatures, but the names and values used in this table are representative for a successful print using Slic3r v1.2.9 software.

EWC's printed using these settings appeared to retain their external profile with both sharp and rounded corners being easily visible. The interior of the EWC was not crossed by ooze-related "stringing" artifacts common to plastic 3D prints and often seen in FRESH prints not utilizing retraction (shown in Figure 3.7A). The top and bottom of the EWC appeared to have equal vertical thickness, indicating that the flow rate over the course of the print did not significantly vary. The side pillars of the EWC were fused and indicated sufficient extrusion amounts for small features without suffering from extruder clogging which frequently occurs in regions utilizing frequent start-stop extrusion motions. Examples of failed and successful EWC prints are visible in Figure3.7B-C.

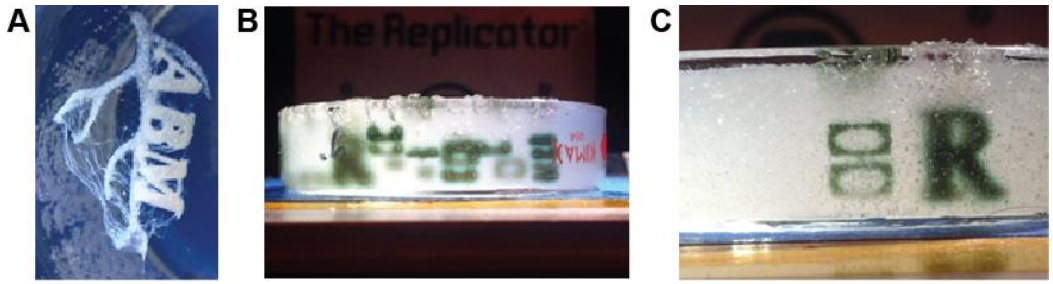

Figure 3.6 Calibration of FRESH printing and retraction settings. (A) A print of a right coronary artery and letters "ABM" showing abundant stringing between the tips of artery branches, an artifact associated with poor retraction settings **(B)** An example of failed EWC prints in a Petri dish filled with support, many of which are due to poor retraction settings. **(C)** An example of two successful EWC prints shown next to a Times New Roman R.

Additional calibration shapes used in printing were the bifurcated tube and the Times New Roman R, both of which are shown in Figure 3.7. Each of these calibration files served a set of specified goals when calibrating machine performance. The bifurcated tube and the Times New Roman R required correct flow rate multiplier and feed rates to be clearly resolved.

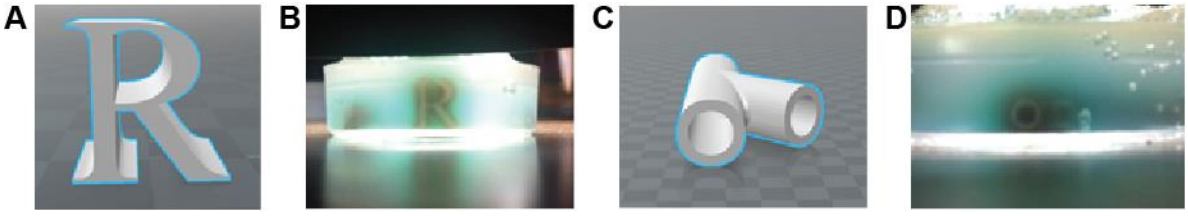

Figure 3.7 The Times New Roman R and the Bifurcated Tube. (A) A 10 mm high Times New Roman R acts as a calibration for FRESH print speeds. **(B)** An example of a successful Times New Roman R print in a petri dish filled with slurry **(C)** A 10 mm long bifurcated tube serves as a calibration for FRESH extrusion rates. **(D)** An example bifurcated tube shown still embedded in slurry

The settings detailed in Table 3.1 served as a foundation on top of which profiles for FRESH printing were created in softwares such as Slic3r, Cura, KISSlicer, and Simplify3D. These softwares were then pit against one another to produce the best possible "pathing" choices evident in the Gcode outputs. To effectively vet the abilities of different softwares to produce a good bioprinting outcome, the Snail Calibration shown in Figure 3.8 was designed and used as the benchmark solid across all slicing softwares. The Snail Calibration was designed as a

bifurcated tube of 3mm outer diameter with an internal diameter of 2 mm and having its trunk looped 360° in a 6.5° spiral. The entire looped bifurcation is embedded in a cylindrical solid of 10 mm outer diameter with a central hole of 4 mm featuring another cylinder of 2 mm at its center. The bifurcation is 35°, and each branch is 2 mm in internal diameter. The Gcodes are shown in Figure 3.8B-3.8F.

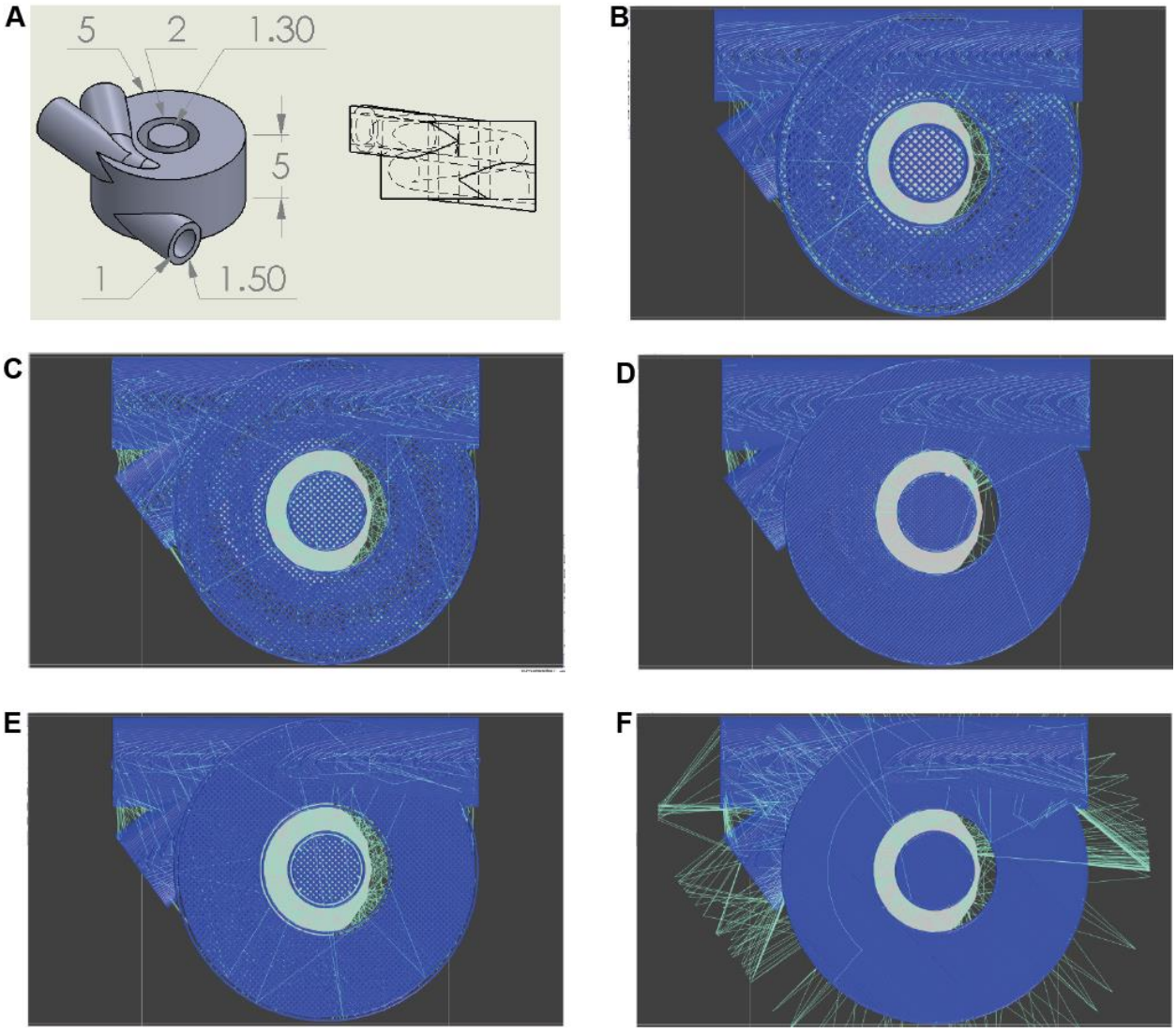

Figure 3.8 Using the snail calibration to vet slicing softwares for ability to avoid perimeter traversal. (A) A schematic of the snail calibration shape showing relative dimensions in mm **(B)** The snail calibration print rendered as Gcode in Simplify3D **(C)** KISSlicer **(D)** Slic3r **(E)** Cura **(F)** Slic3r with "avoid crossing perimeters" enabled. Blue represents extrusion, teal represents travel without extrusion.

Slicing outcomes for the Snail Calibration were judged based on the amount of non-extrusion "traveling" and how much of that traveling traversed print perimeters. It was found that Simplify3D offered the most intelligent pathing, taking into account the shortest travel paths between any two regions of a print while also avoiding unnecessary crossing of perimeters. However, Simplify3D requires a paid license to use, and thus it was not favored as an open source

solution. KISSlicer is not capable of generating the "tool-change" Gcode necessary to properly swap extruders during multi-material prints. Cura and Slic3r were both capable of generating complex travel paths that avoid crossing perimeters, but neither of them were as intelligent as Simplify3D in avoiding unnecessary redundancies when generating infill. Recently, Slic3r's algorithm responsible for avoiding perimeter traversal was overhauled to be context-aware for an entire layer, and this means that the ability to avoid perimeters using the shortest possible number of avoidance moves has recently become available. Previously, the perimeter avoidance was chaotic, appearing like Figure 3.8F. Slic3r is also unique in its support of modifier and part meshes, both of which allow hierarchical assignment of different print settings to different regions of a given print. Being able to subdivide a print into regions occupied by separate mesh files allows the user to orchestrate complex layouts containing myriad combinations of settings in one print. It is this feature that makes Slic3r superlative for multi-material printing. Given Slic3r's forward-thinking development community and the fact that it has always offered the richest feature set of all printing software packages, Slic3r was chosen as the preferred software for FRESH printing. In some cases, other softwares, especially Skeinforge and KISSlicer, were used, but these exceptions were rare and typically occurred before the most recent version of Slic3r was available.

3.4.2 FRESH Printing is Biocompatible and Capable of Complex Geometries

FRESH was used to print complex biological structures based on medical imaging data to demonstrate the capability to fabricate complex geometries. Further, we wanted to validate that prints were mechanically robust and could be formed from multiple types of protein and

polysaccharide hydrogels. First, a human femur from CT data (Figure 3.10A) was scaled down to a length of ~35 mm and a minimum diameter of ~2 mm and FRESH printed in alginate (Figure 3.10B). Applying uniaxial strain showed that the femur could undergo ~40% strain and recover elastically (Figure 3.10C), validating there was mechanical fusion between the printed alginate layers. Further, the femur could be bent in half and elastically recover, and when strained to failure fractured at an oblique angle to the long-axis of the bone, confirming that failure was not due to layer delamination.

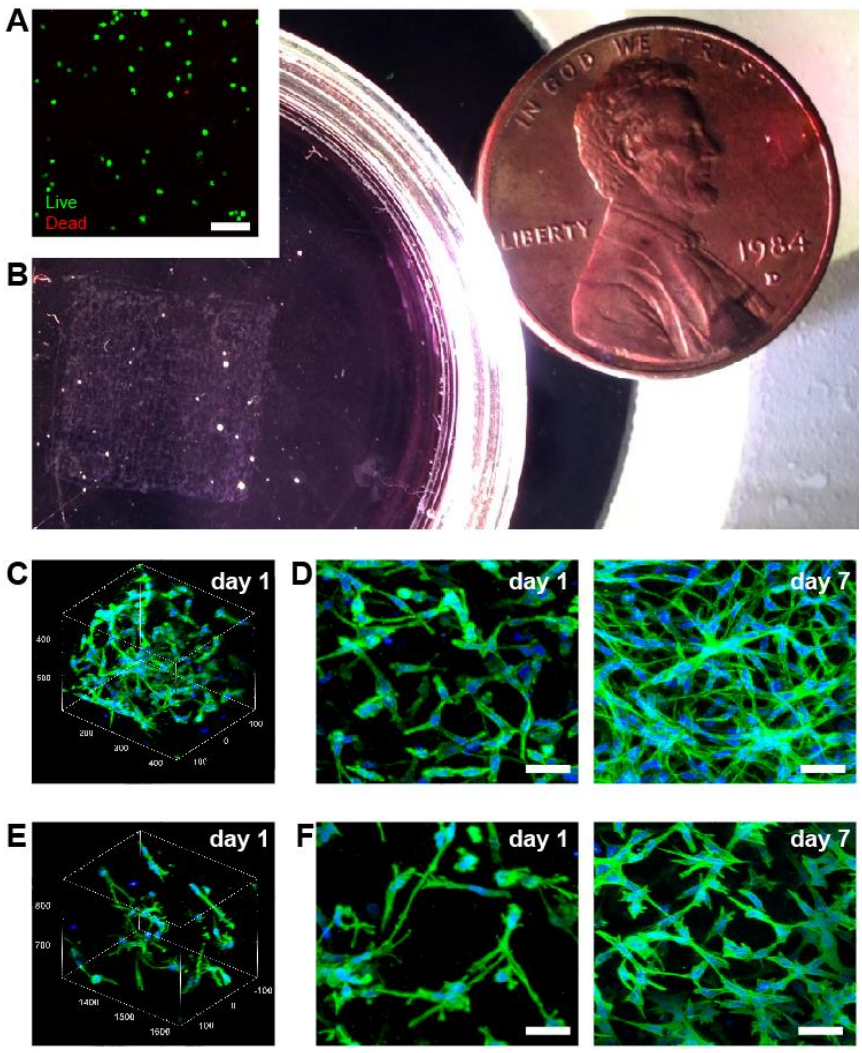

Figure 3.9 3D printed sheets of cells and ECM. (A) Representative live (green) and dead (red) staining of C2C12 cells in 3D printed sheets of multi-component ECM gel 2 hours post fabrication. Scale bar is 100 µm**. (B)** Brightfield image of a printed cell sheet with dimensions of 1 cm square and approximately 200 µm thick**. (C)** 3D image of C2C12 myoblasts and **(E)** MC3T3 fibroblasts in printed sheets after 24 hrs incubation demonstrating homogenous distribution of cells throughout. **(D)** Maximum intensity projections of confocal microscope images of MC3T3 fibroblasts and **(F)** C2C12 myoblasts in FRESH printed constructs at 1 and 7 day time points demonstrating that cells spread and proliferate in 3D. Scale bars are 50 µm.

Shown in Figure 3.9, sheets of C2C12 myoblasts suspended in a mixture of fibrinogen, collagen type I, and Matrigel® were printed at 20°C under sterile conditions and showed 99.7% viability by LIVE/DEAD staining. Multiday studies using C2C12 myoblasts and MC3T3 fibroblasts showed that cells were well distributed in 3D, and over a 7-day culture period formed a high-

density cellular network. These examples demonstrate that FRESH can 3D print mechanically robust parts with high fidelity, high repeatability from a range of ECM hydrogels including collagen, fibrin, and Matrigel® and with embedded cells.

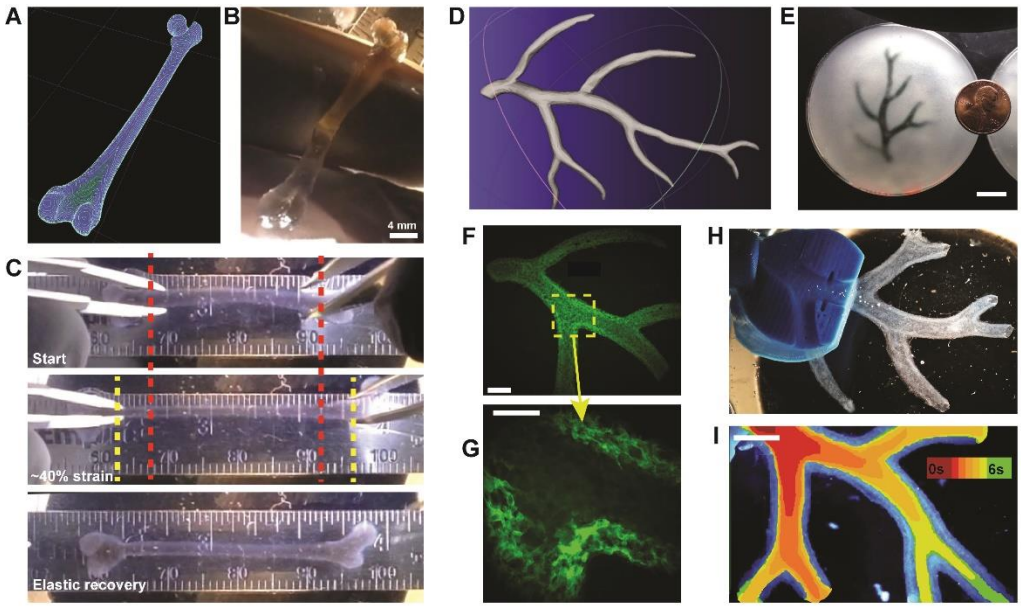

Figure 3.10 FRESH printed objects can display functional properties such as plasticity or perfusability. **(A)** A model of a human artery is scaled down and processed into machine code for FRESH printing. Scale = 100 µm. **(B)** The hydrogel femur closely resembles the model used to print it. Scale = 100 µm **(C)** The femur can be strained in tension and observed to undergo plastic deformation **(D)** A model of a human coronary artery derived from MRI data is processed before printing **(E)** The embedded artery ready for release and imaging Scale bars = 50 µm. **(F)** The artery's fluorescence clearly demonstrates its fidelity to the model. **(G)** A confocal image of the inside of the artery shows the intact lumen of the print. **(H)** The artery is seated in a perfusion mount, and **(I)** black food coloring is pumped through to visualize the interior of the artery.

Next, we evaluated the ability to fabricate a more complex, perfusable structure using MRI data of part of the right coronary artery vascular tree and creating a hollow lumen with a wall thickness of <1 mm (Figure 3.10D). This was FRESH printed to scale with an overall length from trunk to tip of 5 cm and contained multiple bifurcations with 3D tortuosity (Figure 3.10E). Arterial trees printed using fluorescent alginate confirmed that the internal lumens and bifurcations were well formed (Figure 3.10F) and that a wall thickness of <1 mm and lumen

diameters of 1 to 3 mm were achieved (Figure 3.10G). A custom fixture to hold the arterial tree was 3D printed in PLA (Figure 3.10H) and used to perfuse the print. Black dye pumped through the arterial tree confirmed it was patent, manifold, and that hydrogel density was sufficient to prevent diffusion through the wall (Figure 3.10I). Similar to the mechanical testing of the femur (Figure 3.10C), the minimal diffusion through the arterial wall confirmed that the alginate layers were well fused together forming a solid structure. Morphometric analysis, shown in Figure 3.11, of bifurcation angles and distance measurements between various points of the arterial tree demonstrated measurements that mostly deviated less than 10% from their intended values.

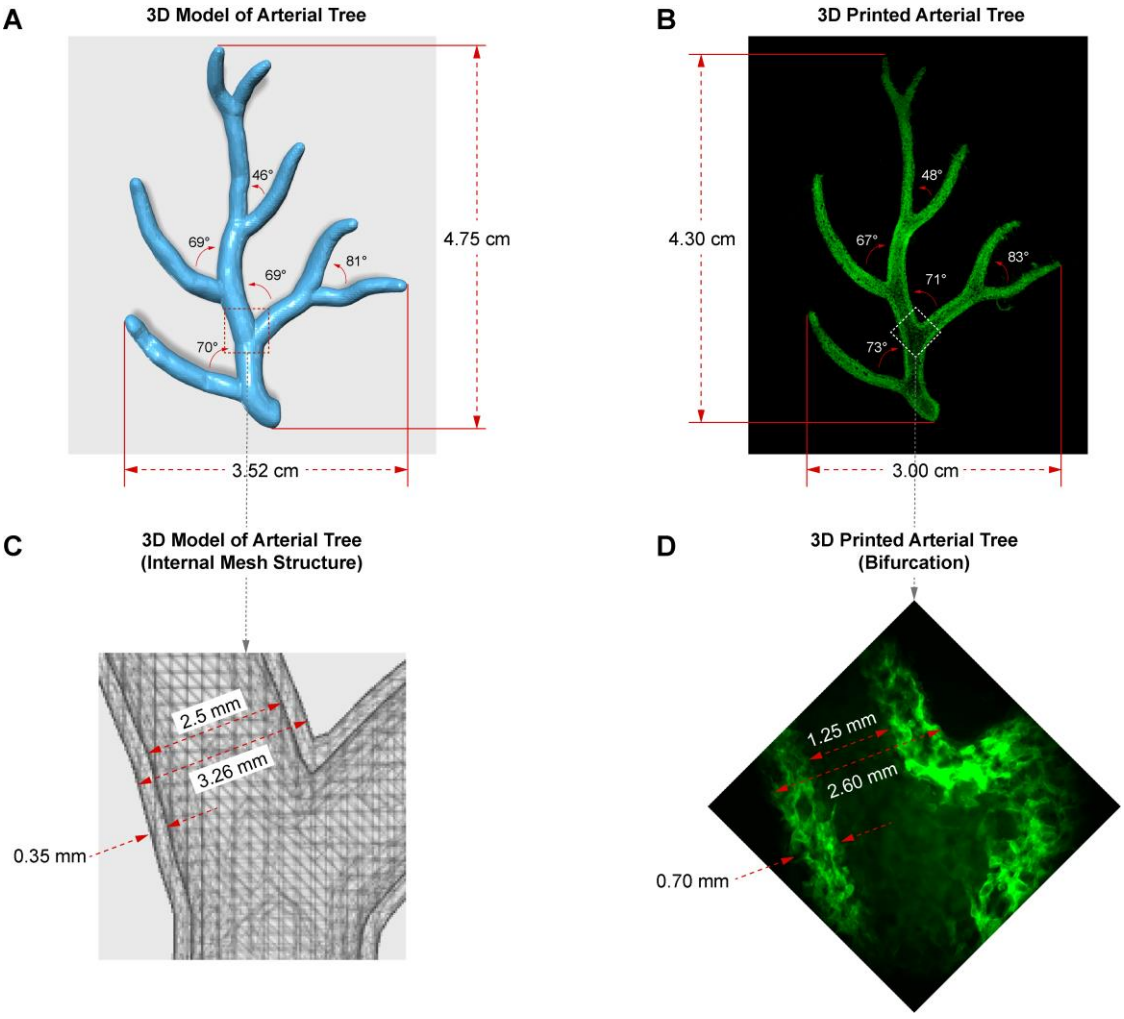

Figure 3.11 A comparison of the 3D model and 3D printed arterial tree to assess print fidelity. (A) A top-down view of the 3D STL model of the arterial tree used in these studies with overall length, width and branching angles quantified. **(B)** A representative, top-down view of the arterial tree 3D printed using fluorescently labeled alginate and imaged using the macro-confocal microscope. Note that the length, width and branching angles are quantified and are in close agreement to those of the original STL file in (A). Because the printed structure is soft and flexible, it is difficult to determine if the dimensional variability (<15%) is due to deformation in the print or printing inaccuracy. **(C)** A zoomed in view of the highlighted region in (A) showing the internal wall and lumen dimensions of the 3D model at the 2nd bifurcation**. (D)** A zoomed in view of the highlighted region in (B) showing the internal wall and lumen dimensions of the 3D printed arterial tree at the 2nd bifurcation. Note that the wall thickness of the 3D printed artery has been purposely increased to increase mechanical integrity, which has resulted in a narrower lumen and a decreased vessel diameter due to the parameters used to generate the G-code.

Finally, we evaluated the ability to FRESH print 3D biological structures with complex internal and external architectures that would be extremely challenging or impossible to create using traditional fabrication techniques. First, we selected a day 5 embryonic chick heart (Figure 3.12A) because of the complex internal trabeculations. We fixed and stained the heart for cell nuclei, F-actin and fibronectin and generated a 3D optical image using confocal microscopy (Figure 3.12B). The 3D optical image was then thresholded, segmented and converted into a solid model for 3D printing (Figure 3.12C). The diameter of the actual embryonic heart (~1 mm) was scaled up by an order-of-magnitude (~1 cm) to better match the resolution of the printer, and it was FRESH printed using fluorescently labeled alginate. The printed heart was then imaged using a multiphoton microscope to generate a cross-section through the structure (Figure 3.12D) showing internal trabeculation comparable to that in the model (Figure 3.12C). A darkfield image of the whole heart provided further validation of print fidelity and the ability to fabricate complex internal structures on the sub-millimeter length scale (Figure 3.12E). To create complex surface structures, we used an MRI image of the human brain (Figure 3.12F) because of the intricate folds in the cortical tissues. A high-resolution view of the 3D brain model shows the surface in detail (Figure 3.12G). While the embryonic heart was scaled up in size, the human brain was scaled down to 3 cm in length to evaluate the resolution limits of the printer and reduce print times. The human brain was 3D printed using alginate and different regions including the frontal and temporal lobes of the cortex and the cerebellum were clearly defined (Figure 3.12H). Visualization of the brain surface was enhanced with black dye and revealed structures that

matched in detail the major white matter folds in the 3D model (Figure 3.12I). Both the 3D printed embryonic heart and brain clearly demonstrate the unique ability of FRESH to print hydrogels with complex internal and external structures at high fidelity.

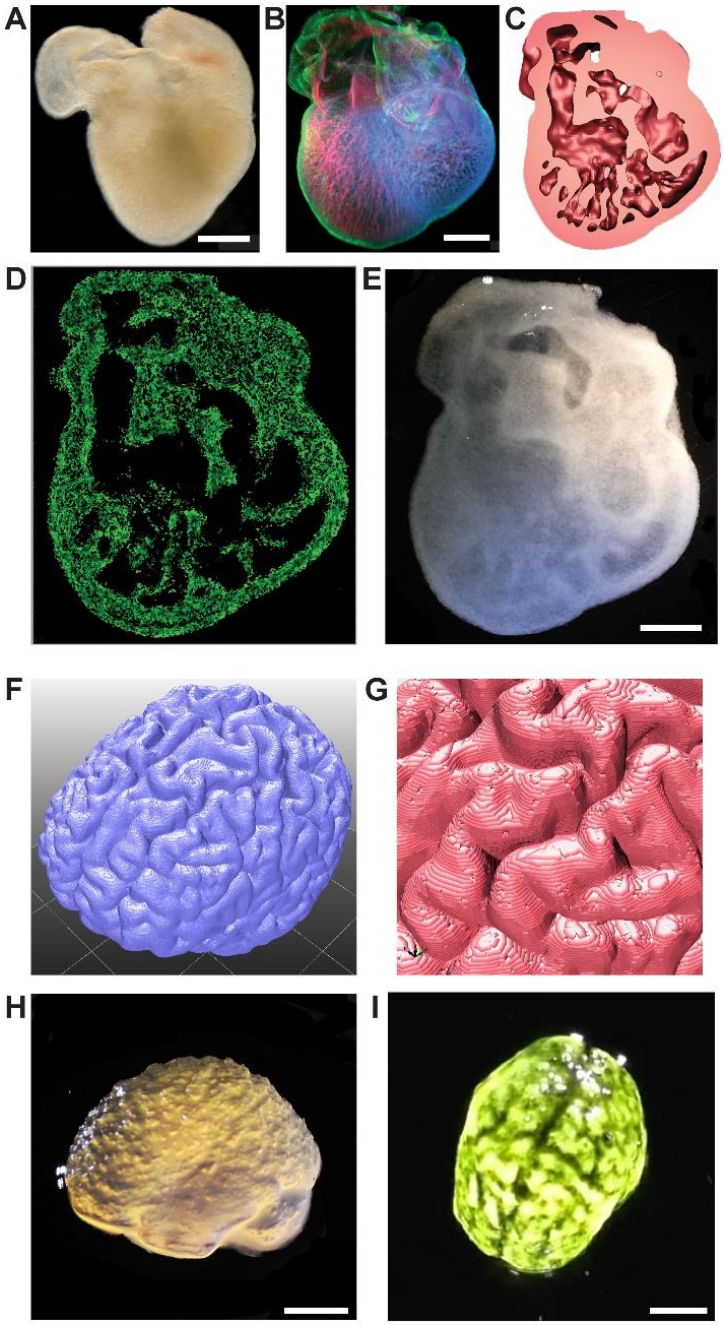

Figure 3.12 Objects with complicated topographies are easily reproduced as FRESH prints. (A) An explanted embryonic chicken heart is **(B)** stained for Fibronectin (green), DNA (blue), and Actin (red) and imaged to produce a **(C)** 3D model that can be FRESH printed. The printed heart is imaged in fluorescence **(D)** and brightfield **(E)** to reveal internal structures that are present in the model generated from imaging data. **(F)** The human brain, as modeled from MRI data, can be processed for FRESH printing. **(G)** A close-up of the processed brain model clearly shows the resulting object will possess a complex surface. **(H)** At first, the printed brain seems to lack the geometries shown in (F) and (G), but addition of a dye to the outside of the print **(I)** provides visual evidence for the presence of sulci and gyri in the printed brain.

After many subsequent iterations of the Replistruder and the invention of scalable methods for producing fine particulate slurries, it was possible to generate not only higher detail prints, but also larger prints. Therefore, we set out to print an entire human heart utilizing data from MRI. The same dataset used for the right coronary artery branch included an entire human heart with

carefully cleaned sections available for selection or printing as a whole. We scaled the heart to 30% of its original size, and then we processed the file for a print using a 150 µm needle and 60 µm layers. The slurry used for this print was a coacervate slurry. Approximately 2.5 mL of 24 mg/mL type I bovine collagen was used to print the heart. The print is shown in Figure 3.13. The heart contained levels of detail that are beyond the means of desktop FDM and included all structures present in the file. Pectinate muscle structures are visible in Figure 3.13B. This printed heart is a freeform print of a soft material and currently represents the pinnacle of bioprinting ability for endogenous ECM. While the shape of the heart is not enough to sufficiently drive (potentially included) cells toward a functional organ, the next logical step would be introduction of sub-mm structures for controlling such behavior.

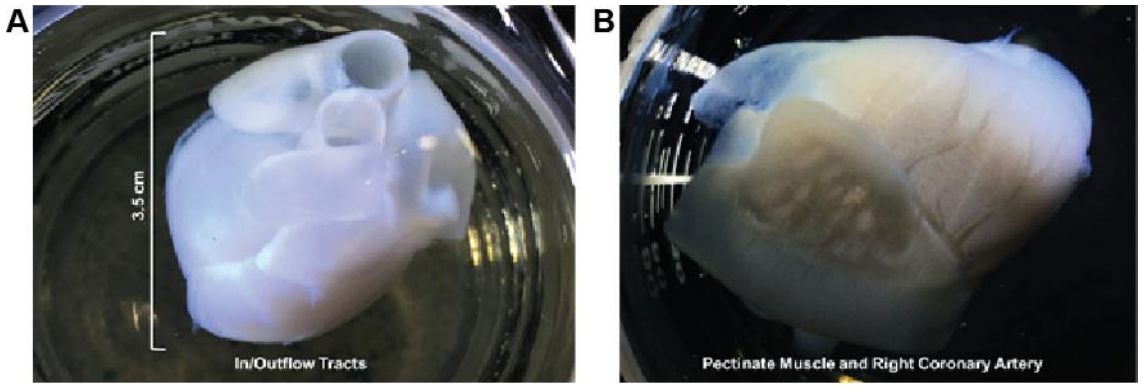

Figure 3.13 Human adult heart FRESH printed from collagen I. (A) The top view of the heart shows the patency of the inflow and outflow tracts **(B)** The right side of the heart shows the right coronary artery, the coronary sinus, and the pectinate muscle visible through the semi-transparent auricle.

3.4.3 Failure Modes for FRESH & The Crowning Artifact

FRESH experiences a variety of failure modes that are unique among printing methods. Since extrusion occurs in a slurry and not in air, extruded fluid must displace slurry during the movement of the needle. If the slurry is too stiff, the extruded fluid will flow up around the

needle. If the slurry is too thin, the extrusion will clump on the end of the needle. It is rare for a slurry to be too thin. Instead, most failures in FRESH occur when the slurry is too stiff. Extruded fluid that is unable to displace slurry will move to the momentarily liquefied region of slurry surrounding the needle, effectively boring its way up above the current layer being printed. In cases where this ink gels quickly, this can result in a sock-like buildup of ink around the needle, effectively blocking further extrusion. In other cases, this gelling fluid is left behind by the needle and gradually accumulates above the plane of extrusion for multiple subsequent layers. The result in any case is the buildup of ink above the intended layers. Since this buildup is most likely to occur above regions that require more ink, and the perimeter of any given print is generally considered to be slightly statistically denser in ink, there appears to be a "crown" of ink around the top perimeter of a print. This "crowning" artifact (Figure 3.14) can occur in lower levels of the print and become masked by solid structures printed above these levels, but it is generally the case that the topmost layer will have a "haze" or "crown" above it.

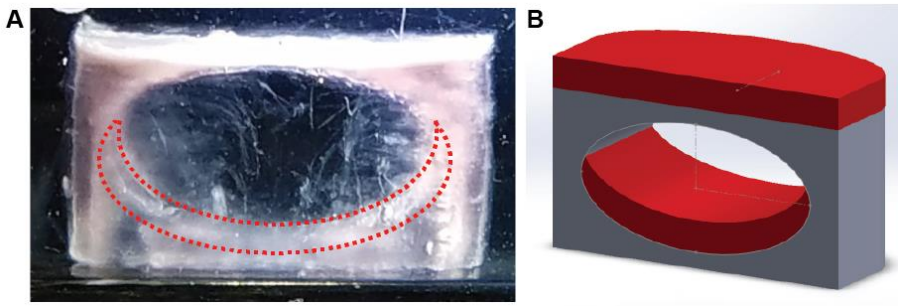

Figure 3.14 Crowning artifact in an EWC print. (A) Suspected crowning artifact is shown in dashed line on a 10 mm x 5 mm EWC print. **(B)** Regions likely to produce crowning artifacts (red) on an EWC (grey).

Perfect FRESH prints come out without a crown, but it is difficult to accomplish this using a blended slurry. As particle size is enlarged in a slurry, the chance that any given extrusion will deform around a large particle and end up in a plane above the current extrusion activity is larger.

On the other hand, as a finer slurry is used, the fluid extrusion more easily displaces particles or viscously fingers into the slurry, avoiding the tendency to branch upward toward the liquefied region surrounding the needle.

During the calibration of a new kind of ink, it is important to figure out the necessary amount of ink extrusion (as a ratio to the ideal extrusion volume used in plastic FDM) to avoid problems like crowning. Extruding too much ink for a given solid can just as easily result in crowning as a stiff slurry. In theory, however, once the correct amount of ink extrusion is figured out, crowning should only be attributable to the slurry. When two fluids of different viscosities meet at an unstable interface, viscous fingering results. Since fluid inks (low viscosity) often viscously finger outward into slurries (high viscosity), branching and flowing around particles, print extrusions occupy a much larger effective volume than the idealized flattened cylinder model used for plastic FDM. Different amounts of viscous fingering dictated by ink gelation kinetics and rheology result in inks with different relative volumes. In the case of alginate, the flow rate multiplier must be adjusted down from 1.0 to 0.6. Alginate tends to quickly viscously finger due in part to its nearly-immediate gelation in a slurry containing a small amount of calcium ions. The boundary of the gelled alginate and the incoming alginate solution is unstable during the extrusion process, so breaks in the boundary lead to further growth of the boundary in a branching manner that is exacerbated by the heterogeneous nature of particulate slurries. For slower gelling fluids, such as collagen type I solutions, a flow rate multiplier of 1.0 is used, because the collagen extrusion is capable of displacing slurry during printing and readily flows as a viscous fluid before later gelling in the bath. It is possible to under-extrude a material, but this mode of

failure has not been seen in some time – more than 2 years, and its appearance is attributable to negligence in cleaning needles or a hardware problem such as a disconnected extruder motor.

Collagen and other slow-gelling inks are prone to diffusion in the slurry. This phenomenon is visible as a diffuse haze surrounding collagen FRESH prints, and the only current solution to this is more aggressive methods of gelation in the print bath. Efforts to curb this diffusion include the use of NaOH, Proton Sponge (Sigma), and post-treatment crosslinking chemicals such as riboflavin, transglutaminase, and glutaraldehyde.

Now that the failure modes of FRESH are understood well enough to indicate problems with materials used in the system, it is possible to utilize these problems to improve the entire process. Hundreds of prints have been discarded due to these failure modes, but they have provided insight toward better settings and material processing protocols. These failures have only brought us closer to our end goal of being able to expertly print ECM.

3.4.4 Multi-Material Prints Offer Synergistic Performance Gains Over Single Material Prints

Rings of collagen printed without a reinforcement such as a surrounding gel are not handleable. Most unmodified collagen hydrogel 3D prints cannot be lifted out of solution without introducing permanent deformation, and this is because the collagen hydrogel is too weak to support itself outside of solution. It was thought that including a rigid hydrogel such as alginate alongside the collagen would provide a reinforcement that would fuse to and sustain the collagen's geometry out of solution. A ring of printed collagen hydrogel supported by a printed alginate mesh shown in Figure 3.15A was shown to not only remained fused at the border of the two hydrogels but also maintain correct dimensions even after being transported in air multiple

times. The largest dimensional deviation from the file was found at the sides of the alginate mesh, which were supposed to be 8mm but turned out closer to 8.25mm. The collagen ring was supposed to have an internal diameter of 4.4 mm and an outer diameter of 6 mm. In Figure 3.15B, the measurements for the edge of the alginate mesh, and the internal and external diameters of the collagen ring are shown. In another example, collagen sections which were manually plucked from their alginate mesh counterparts shown in Figure 3.15C brought with them portions of alginate mesh during dissection, as seen in Figure 3.15D. The fusion between the alginate and collagen portions of these multi-material prints is thought to be responsible for maintaining collagen geometry during handling. Furthermore, a multi-material collagen and alginate print of a scaled-up developing mammary duct epithelium survived a drop to the lab floor (Figure 3.15E). After it was recovered and imaged, it was shown to be intact and encased in alginate fibers clearly visible in Figure 3.15F. Further investigation into the maintenance of collagen geometry under handling forces is needed and will likely include material testing of multi-material prints. Since collagen by itself is a fragile material incapable of being delicately printed in a manner that bears its weight outside of solution, this method of reinforcing collagen with alginate presents a promising solution for creating and allowing the manipulation of complex collagen components. What's more, the collagen can be isolated from the alginate without damage by submersion in a calcium chelating bath, which results in dissolution of the alginate mesh and complete release of the collagen component, as shown in Figure 3.15G. In cell culture, discussed in section 4.3.3, it was seen that these constructs displayed the compaction of collagen constructs when seeded with cells, while maintaining overall geometric fidelity. Due to the presence of the alginate mesh,

it is noted that these constructs could be easily handled, seeded, cultured, and fixed without every touching or interfering with the collagen component.

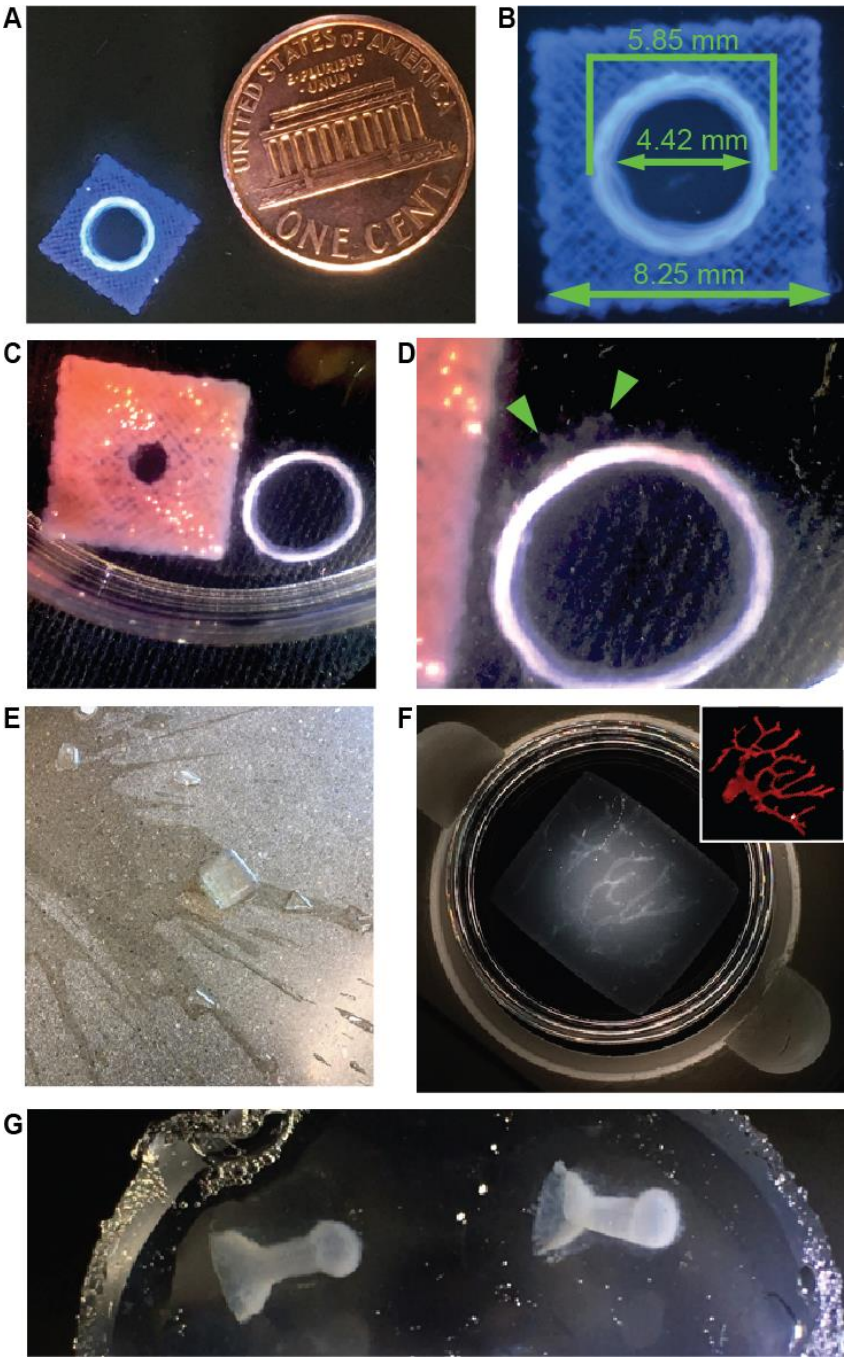

Figure 3.15 Stiff hydrogel components protect fragile hydrogel components in multi-material prints. (A) A multi-material print showing an inner ring of collagen hydrogel surrounded by alginate hydrogel stained with Alcian Blue. U.S. penny for scale. **(B)** The measured construct shows dimensions consistent with the intended diameters. **(C)** A dissected multi-material print showing collagen ring on right and alginate mesh on left in pink **(D)** The removed collagen ring shows alginate fibers that were fused to the collagen and could not be separated, proving fusion of the gels. **(E)** A multi-material print is shown on the floor of a lab after having fallen several feet along with shards of its parent beaker. **(F)** The print in (E) recovered and under dark field illumination, showing maintenance of the fragile collagen component inside the print's interior. Inset is the file for the collagen component. **(G)** Collagen-based 3D printed tissues **removed from alginate threads**

In comparison to other techniques utilizing fluid inks, FRESH is faster, capable of printing more materials, and it can do so while allowing for complete release of a print from an embedding medium. Table 3.2 shown below summarizes the differences.

			Direct Write	Carbopol Bath	Self Heal Bath	FRESH
		Overhangs	no	yes	yes	yes
		Speed (mm/s)	5	10	10	80
		Medium	air	carbopol	gel	gelatin slurry
		Isotonic Chemistry	dry	no	yes	yes
		Damageless	yes	no	no	yes
Fluid Inks	ECM Gels	Collagen	no	yes	yes	yes
		Matrigel	no	yes	yes	yes
		Fibrin	no	yes	yes	yes
	Cells		yes	yes	yes	yes
	Thixotropic/ Yield-Stress Fluids	Slurries	yes	yes	yes	yes
		Resins	yes	yes	yes	yes
		Alginate-CaSO4	yes	yes	yes	yes
		Poloxamer Gels	yes	yes	yes	yes
	Ionic Gels	Alginate	no	no	yes	yes
		Cellulose	no	no	yes	yes
	Photopolymer	Acrylates	yes	yes	yes	yes

Table 3.2. Comparison of FRESH to other fluid printing techniques. Direct write printing is representative of FDM of fluids and many other techniques not limited to Jennifer Lewis' group at Harvard[37]. Carbopol bath denotes methods used in Angelini's group at Florida[5]. Self-healing gels is a technique used by Jason Burdick's group[29]. Finally, FRESH is our technique and is used by many labs across the globe. *carbopol baths can support cells physically but many sensitive cells will die in carbopol baths in short periods of time (<1 hr).

3.5 Conclusion

In this chapter, we discussed the novel FRESH printing method and its application toward various demonstrative examples of 3D bioprinting hydrogels. We covered the initial conception of FRESH, the generation of its requisite support materials, understanding its modes of failure, and later optimizing it for performance. Then, we applied FRESH toward fabrication of complex

anatomical forms described by open datasets. Some of these constructs contained cells and possessed nominal viability of 99.7%, and some of the constructs were functionally perfused with fluid. Finally, multi-material prints were created in demonstration of synergistic material combinations. Overall, FRESH is the first method for 3D printing a wide array of hydrogel materials that is now used by many in our lab and in labs across the world. With FRESH, it has become possible to prototype complex hydrogel constructs as easily as one 3D prints thermoplastic, and by using the same software.

Chapter 4 3D Printing Parametric and Biomimetic Mammary Gland Epithelium Models to Generate Heterogeneous Composition and Spatially Varied Epithelial Monolayers

4.1 Abstract

Being able to fabricate any geometry we desire from combinations of unmodified ECM allows us to design tissues with architecture that mimics in vivo conditions. In this chapter, we apply the hardware, software, and FRESH method seen and thoroughly tested in chapter 3 toward additive manufacturing of a set of complex biomimetic multi-material hydrogel scaffolds suited for tissue culture. First, to design our scaffolds, we analyze data sets to draw necessary conclusions about in vivo architecture. Then, we demonstrate FRESH printing of heterogeneous constructs containing multiple different hydrogels. Finally, we seed and culture such constructs to illustrate their stability under the forces and chemistry of cell behavior. Printed constructs display maintenance of overall geometry for at least one week in culture. We demonstrate the 3D programming of synergistic mechanical behaviors between two separate hydrogels combined in a single additively manufactured object. Not only do we maintain architecture through culture, but we passively program the combination of hydrogels to resist deformation without interfering with the endogenous chemistry of the chosen hydrogels or the genetics of seeded cells.

4.2 Introduction

A collagen hydrogel containing cells will often compact over time due to the adhesion, proliferation, and remodeling of the cells. If this process is unregulated, many constructs will compact to a dense state containing a necrotic core. Many engineered tissues consist of a cellular gel that is compacted around a mandrel or series of rigid posts meant to align internal cells based on the stresses inside the gel[27,42]. In an unconstrained tubular construct, compaction would manifest as initial closure of the internal lumen and eventual fusion into a dense mass. It is therefore reasonable to expect an engineered branching construct such as a ductal epithelium to compact into a denser, dysfunctional state with necrotic regions and partial lumen closure. While it may be possible to formulate a collagenous, cellular hydrogel ink that does not compact in culture, the requirements for this are likely beyond the scope of this project. Instead, it should be easier to embed the collagen construct inside a sparse net of rigid alginate hydrogel extrusions (Figure 4.1A). Forces that normally deform the collagen hydrogel would instead be forced to work against the alginate mesh that surrounds the construct. The alginate would be included in the print as a separate ink in an additional extruder, and the mesh would be generated as a sparse infill pattern normally seen in the interior of 3D prints. As explained in Section 3.4.4, dual-extrusion of collagenous hydrogel and alginate ink is a relatively simple process and relies on a dual extruder that has already been designed and implemented for several multi-material prints. Testing this approach of immobilizing one printed material within another would likely require a simplified geometry such as a vertical tube of collagen gel to be printed in alginate mesh (Figure 4.1C). Measuring the dimensions of the tube could be accomplished as with the gauging of print accuracy using calibration prints – micrographs could be compared with known digital

dimensions. If, by using this approach, we can fabricate a cellular collagenous tube coated in epithelium and maintain its geometry while in culture, it may be possible to then create a complete epithelial tree.

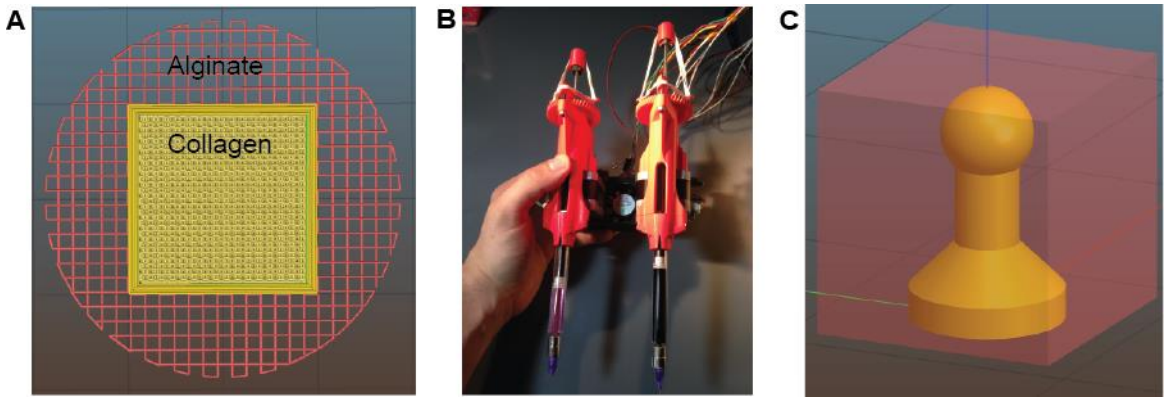

Figure 4.1 Utilizing Dual Extrusion to Reinforce Soft Hydrogels with Rigid Hydrogel Mesh. **(A)** A soft collagen hydrogel mass is 3D printed alongside a sparse net of a more rigid alginate hydrogel. **(B)** Two steppers power a pair of syringe pump extruders with collagen and alginate hydrogel inks. **(C)** A hollow tube is printed from a soft hydrogel inside an alginate mesh to preserve its shape during handling or culture.

Replicating the in vivo environment in vitro means engineering constructs to closely mimic the appearance of in vivo equivalents. The microscopic geometry of tissues is often more complex and dynamic than we can hope to recreate with any current technology, but macroscopic features are easily replicable using 3D printing[9]. We can process imaging data (Figure 4.2A) from optical projection tomography (OPT) of whole-mount tissue samples, and, through software analysis, model the tissue as a 3D printable solid (Figure 4.2B). By printing an entire ductal epithelium modeled from imaging data, we can ensure that the internal features of the epithelium such as the bifurcations within the branching tree are geometrically representative of native tissues (Figure 4.2C). Furthermore, we can easily change our printed epithelium to a different model derived from a different set of imaging data or parametrically alter it to suit our needs.

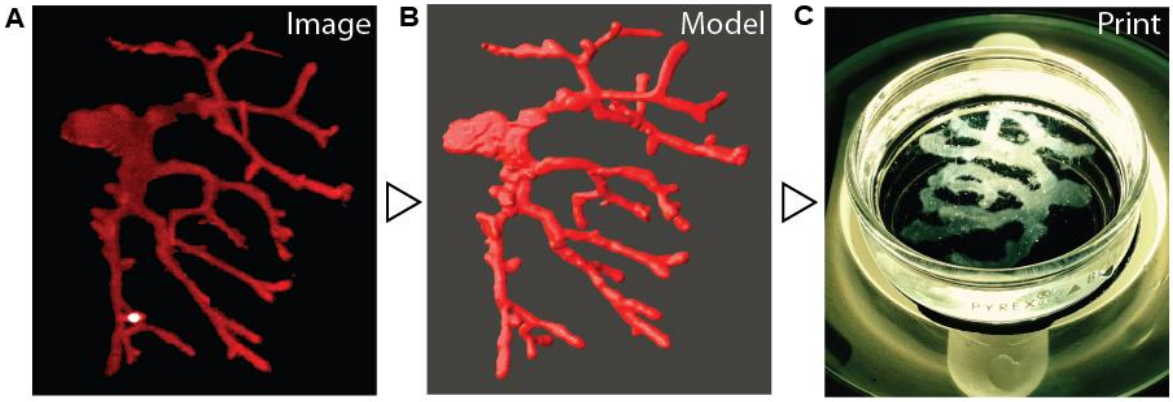

Figure 4.2 Imaging, modeling, and 3D printing a ductal epithelial tree. (A) A ductal epithelium tree is imaged using OPT or some other 3D scanning method. **(B)** A model of the ductal epithelium is generated from the imaging data. **(C)** A solid representation of the external geometry of the model is FRESH printed from a hydrogel shown in darkfield illumination.

Since it has been found that ductal epithelium possesses 4 distinct developmental morphologies which are intimately associated with the 3 most commonly used mouse strains in breast cancer research, it is important to be able to vary the chosen geometry of the epithelium and obtain similar levels of accuracy across different morphologies[28]. Verifying said accuracy of the 3D prints involves imaging them using a technique such as OPT or confocal microscopy, for the data obtained from such processes can be used to directly compare the output of the 3D printer with the input file's dimensions. 3D printing an accurate model of the ductal epithelium to culture epithelium will allow researchers to closely simulate the in vivo environment for DCIS and potentially even study the in situ-to-invasive transition without using a host organism. The opportunity to probe the behavior of DCIS in an environment that is both biomimetic and entirely customizable would prove an invaluable tool for understanding which instances of DCIS deserve intervention. Indeed, the printed epithelial model could be generated from imaging data for a specific patient with DCIS, and then a coring needle biopsy could be used to seed the construct with both the patient's epithelial cells and the suspect lesion. Growing the lesion outside the

patient would allow doctors to identify necessary treatment routines and targeted therapies without assuming the worst-case pre-malignant scenario which is a prevalent assumption among current patients. We believe such an approach as that detailed herein will allow any researcher with an open source 3d printer to fashion complex tissues from collagenous biomaterials and cells, and the implications of that are far beyond the realm of cancer research.

In this chapter, we seek to demonstrate the application of technologies thus far discussed in chapters 2 and 3 toward fabrication of a clinically relevant tissue model for cancer research. We start by tackling conversion of complex image data stacks of epithelial tissues into 3D meshes that can be processed and 3D printed at numerous sizes and shapes. Next, we draw from these structures a fundamental morphology and parametrically incorporate it into a representative parametric "module" designed in CAD. This module can be edited to account for any design shortcomings while still reflecting the necessary aspects of in vivo complexity. After we demonstrate the rapid prototyping of this solid using the methodology demonstrated in chapter 3, we incorporate epithelial cell populations into the construct and culture the resulting tissues for up to 1 week – enough time for seeded cells to form an epithelial monolayer. We show that these monolayers reflect the intended design shown in the CAD file and are stable over at least 1 week of culture, effectively making them rapidly prototyped epithelia with the ability to be quickly redesigned to suit the need of a given application. The tissues adopt a final geometry that is present in the first stage of fabrication while containing soft hydrogels that are prone to compaction and plastic deformation. Herein we demonstrate application of multi-component, multi-material prints that sustain programmed geometry utilizing only inert, internal supports that do not interfere with tissue function *in vitro*.

The flexibility of the application described in this chapter is such that it would, in theory, allow anyone to prototype delicate branching structures out of any soft hydrogel, with or without cells and without the fear of cells compacting away any complex geometry. Finally, to test this hypothesis, we push our hardware to its limit by printing an entire ductal epithelium tree at approximately 200% in vivo scale using collagen type I and demonstrate its fidelity to the imaging data from whence it came. The implications present in this effort are monstrous for 3D bioprinting. That a single individual utilizing off-the-shelf hardware, software, and materials can fabricate a construct that is greater in 3-dimensional complexity than anything thus far "bioprinted" in collagen or equivalent hydrogels is enough to induce disruptive communications between varying research institutions. When the total cost of the system and materials is quoted at sub-$1000, this research becomes affordable to every interested party and justifiably more profound.

4.3 Materials & Methods

4.3.1 Processing Tomographic Data of Ductal Epithelia into a Model Suited for 3DP

A stack of a mammary ductal epithelium imaged using Optical Projection Tomography was imported into Seg3D 4.2 (National Institutes of Health). The data, consisting of a stack of BMP images, was imported as a data volume and Gaussian smoothed to improve connectivity between regions and remove noise. Then, the data volume was used to generate an isovolume/isosurface representing a thresholded set of voxels with Seg3D's own smoothing used to connect the voxels. Then, the isosurface was exported to ImageVis3D (National Institutes of Health). There, the file was exported as a binary STL. The binary STL file was imported into

Meshlab and processed with a HC Laplacian Smoothing algorithm to remove the artifact of inter-tile stitching present in the data. Then, the largest connected surface representing the entire ductal epithelium was selected and cut-pasted into a new file. The resulting file was exported as a binary STL and opened in 3D Builder (Microsoft). 3D Builder's settle operation was used to arrange the file with as little z height as possible. Then the file was centered at X = 0, Y = 0, and it was exported as a binary STL representing the processed ductal epithelium and the "collagen" component of a multi-material reinforced print. The X, Y, and Z dimensions of the file were measured, and a rectangular solid with these measurements was created in Solidworks and exported as a binary STL. The binary STL was imported alongside the processed ductal epithelium STL in Meshlab as two layers of a given workspace. The processed ductal epithelium was normal-inverted, and the resulting set of layers was collapsed into one layer. Then the stacked surface layers were exported as a single binary STL. This file could be used as the "alginate" component of any multi-material reinforced print and perfectly complemented the initial "collagen" component's geometry.

4.3.2 Designing a Parametric Mammary Gland Terminal End Bud Model

To avoid the challenges of perfusion seeding and still enable distribution of cells throughout a construct with a sealed lumen, it was decided to try and seed constructs using a gravity-driven fluidic distribution system included in the mammary construct geometry. Mammary constructs, referred to by their two main iterations MK1 and MK2 had the same fundamental collagen component design of a funnel that fed into a tube "duct" which terminated in a spherical "bud". It was assumed that the funnel could be held up above the surface of cell

culture media and used as a receptacle for a cell suspension and allow cell suspension to flow down into the rest of the construct through the walls of the duct and bud. It was hypothesized that, were it not possible to seed the sides of the duct and bud using this approach, then the construct could be seeded in waves, and the construct could be rested on its side to allow for each wave of cells in to coat the sides of the duct and bud. To allow for introduction of the cell suspension to the funnel and for resting of the construct on its side, the alginate mesh reinforcement was designed as a cube centered on and surrounding the collagen component.

Part of the design process for the mammary constructs revolved around the capabilities of the 3D printing softwares and the Duet printer. Since the smallest diameter needles we could utilize were 80 µm, we decided to design the collagen components to feature wall thicknesses in multiples of 80 µm. The interior lumen of the duct was the smallest feature of this print with an initial diameter of 200 µm in generation 1 (MK1), but this value was increased to nearly 1 mm in generation 2 (MK2). The resulting design features are shown in Figure 4.3. The size of the reinforcing alginate component was increased from 4 mm in X and Y to 8 mm to allow for easier handling of the entire construct.

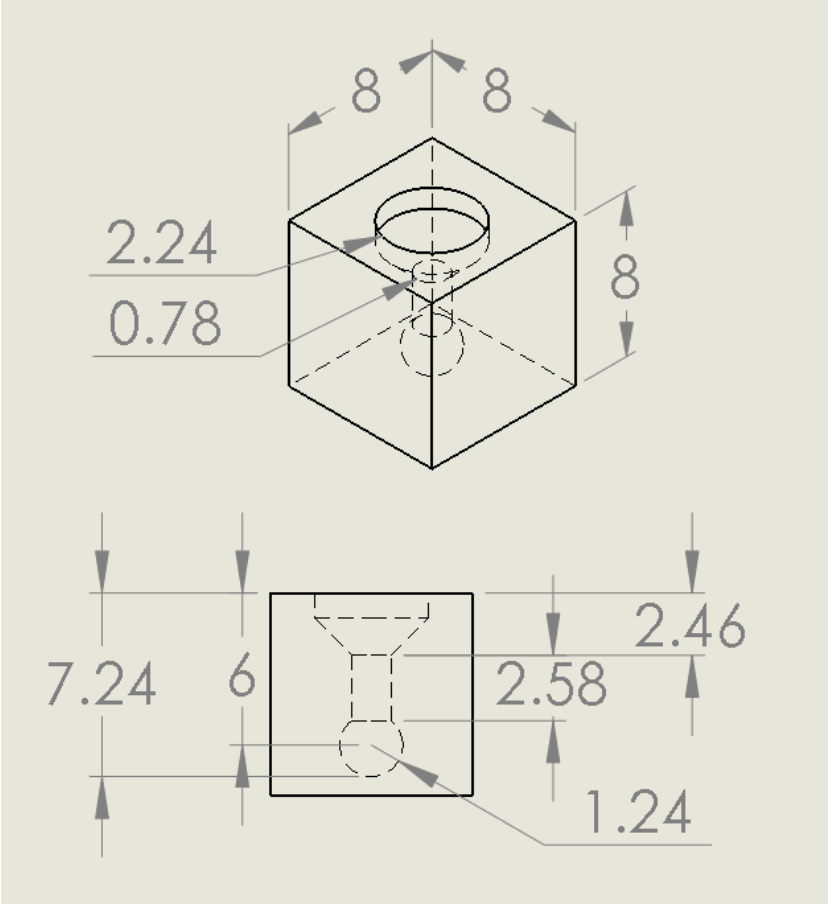

Figure 4.3 The MK2 parametric mammary duct module. The MK2 module features a vertical tube with a bulbous end and a funneled top. The dimensions of the construct were chosen based on what the printer was known to be capable of rendering in collagen type I.

4.3.3 Optimization of Multi-Material Printing for Model Tissues

The collagen component for a given model was imported into Slic3r, and, then, the accompanying alginate component was imported as a "part" of the original collagen component by utilizing the Slic3r mesh editing menu. The collagen component was specified as using the first extruder and the alginate component the second. The alginate component was then assigned setting modifiers shown in Table 4.1 below.

Variable Name	Value for Collagen	Value for Alginate
Extrusion width	0.08 mm	0.15 mm
Infill %	100%	40%
Perimeters	3	0
Speed of Infill	5 mm/s	23 mm/s
Infill Perimeter Overlap	0%	55%
Infill Pattern	Concentric & Rectilinear	Rectilinear

Table 4.1 Setting modifiers used for separate components of MK2. These settings are the primary variables required when separately processing different alginate and collagen components of a multi-material print in Slic3r.

To print two materials, the first and second Replistruders in the duet printer were loaded with a 100 µL syringe of collagen featuring an 80 µm needle and a 2.5 mL syringe of alginate featuring a 150 µm needle. The Replistruders were aligned to their 58.5 mm X offset per the method in section 2.3.6. Then, when Gcode was generated in Slic3r, the following tool change Gcode was inserted at every point in the Gcode where a switch between Replistruders took place:

"T[next_extruder]
M302 P1
G91
G1 Z20
G90"

The above Gcode segment provided the machine with the command to move up 20 mm in Z relative to its current position before switching to another extruder.

The 80 µm needle on the collagen syringe was so long and thin that it was subject to deflection during printing, resulting in poor rendering of machine movements by the extruder. Any vertical tubes printed by this needle ended up fused shut, and sharp corners were rounded. The solution to this was to laser-cut a larger needle to use as a brace. A ½ in long 250 µm needle was laser cut, filled with uncured epoxy, slid onto the 80 µm needle, and baked at 65°C for 2 hours.

It can be challenging to fill a container with just enough support bath to print a multi-material construct without wasting material and ultimately introducing bubbles into the slurry (and the print). Custom containers shown in Figure 4.4 were designed and 3D printed for each multi-material construct. A MakerBot Replicator 2X was used to prototype the containers in PLA plastic. These containers could be filled with slurry from side ports included in their designs. Plungers from 60 mL BD Plastic disposable syringes were inserted into 50 mL Falcon centrifuge tubes filled with compacted slurry, and the bottom tips of the centrifuge tubes were sliced off using razor blades. The resulting improvised syringes of slurry could then be used to inject slurry into the custom print containers. The top surface of the slurry could be flattened using a straightedge object to scrape excess slurry across the top opening of the container. These print containers could be secured to the printer's platform using silicone grease.

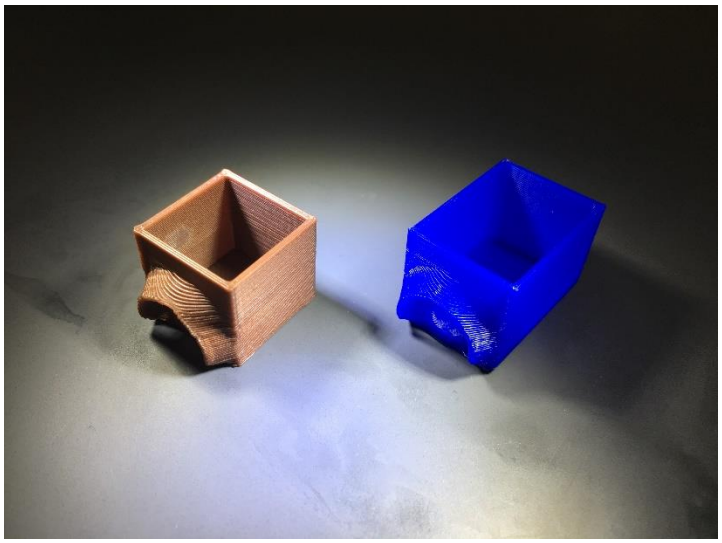

Figure 4.4 Print containers for parametric and biomimetic mammary duct models. These 3D printed containers were created to save on support bath material and guarantee the correct height of container for hosting FRESH prints of the MK2 and the biomimetic mammary duct modules.

4.3.4 Preparation of Constructs for Cell Culture

MK2's were thoroughly washed in warm 70 mM $CaCl_2$ with 25 mM Na-HEPES for at least 24 hours before submersion into 70 mM $CaCl_2$ with 25mM Na-HEPES and 50% v/v Ethanol. MK2's in this 50% Ethanol solution were then allowed to sit for 24 hours at 4°C. On the day of seeding and initiating culture, constructs were removed from this ethanol solution and placed into warm 70 mM $CaCl_2$ with 25mM Na-HEPES. After resting in this fluid for at least 30 minutes, the constructs were washed with fresh 70 mM $CaCl_2$ with 25mM Na-HEPES before being placed into cell media supplemented with 10 mM $CaCl_2$.

4.3.5 Seeding, Culturing Epithelial Cells Inside Constructs

ATCC MCF7 (HTB-22) and ATCC MCF 10A (CRL-10317) cells were transfected with pHIV-ZSGreen lentivirus and flow sorted to select for transfected cells. Resulting cells were cultured per ATCC guidelines. Constructs were washed in sterile-filtered 20°C 1% $CaCl_2$ with 25 mM Na-HEPES. Constructs were then soaked in 20°C sterile-filtered ATCC media, supplemented with 10 mM $CaCl_2$ and 200 µg/mL Penicillin-Streptomycin for 10 minutes. Then constructs were placed in a 6-well plate with one construct per well. Supplemented media was added to each well until half of the construct was submerged (approx. 3 mL). Cells were suspended in supplemented media at 1 x 10^6 cells/mL. 50 µL of cells suspension was pipetted directly into the center of the funnel portion of each construct. For half of the constructs, they were turned onto one of their 4 sides and allowed to rest there for 20 minutes at 37°C. Then, the seeding was repeated followed by 4 more resting periods until each construct was seeded on each side. Constructs were quickly imaged on an Olympus IX83 fluorescence microscope to ensure cells were in the

constructs. One construct of the three for each cell type that was not rotated during seeding was seeded with 200,000 cells in the upright position. All constructs were finally returned to their upright conditions and placed in 37°C culture for 7 days, with regular media exchange. After 7 days, media was aspirated from each well before fixation.

4.3.6 Fixation, Imaging, and Release of Cultured Tissue Model from Alginate

Cultured MK2's were rinsed with 1X PBS (supplemented with 0.625 mM $MgCl_2$ and 10 mM $CaCl_2$) at 37°C, fixed in 4% w/v formaldehyde with 10 mM $CaCl_2$ (Polysciences, Inc.) for 15 min, and then washed 3 times in 11 mM $CaCl_2$ with 25 mM Na-HEPES. The fixed MK2 was imaged with a Nikon AZ-C2 macro confocal microscope with a 5x objective (0.45 NA) and a Leica SP5 multiphoton microscope with a 10x (NA = 0.4) objective and a 25x (NA=0.95) water immersion objective. 3D image stacks were deconvolved with AutoQuant X3 and processed with Imaris 7.5.

In cases where the collagen and cells were obscured by alginate threads, it was possible to remove the alginate by washing a fixed MK2 in a 100 mM Na-Citrate buffer solution for 12 hours. Then, the construct could be embedded in 10% w/v Gelatin A and sectioned. The resulting collagen component with attached interior cells was then accessible by the microscopes. After removal of alginate threads, we acquired 3D z-stacks using reflectance imaging of collagen I at 435 nm with a Leica SP5 multiphoton microscope and a 25x water objective (NA = 0.95). Using ImageJ, we measured the thickness of the collagen I hydrogels in cross-section.

4.4 Results & Discussion

4.4.1 Physical Deflection of and Slicer Handling of Small Diameter Needles

It was found that all software packages capable of performing multi-material printing were capable of rendering the MK1 and MK2 constructs, yet only Slic3r could generate a reinforcing network of alginate fibers surrounding a collagen component without introducing extraneous filaments at the perimeter of the alginate component. It was challenging to trick Slic3r to render the tube of material forming the "duct" of the MK1 and MK2. The most difficult aspect of this challenge was producing a wall of collagen material with uniform thickness across the entire length of the construct. Ideally, before it was realized that needle deflection was causing misalignment of collagen extrusions, it was thought that concentric rings of collagen would best render the wall of the construct. As seen in Figure 4.5A, Cura was not able to generate such a pattern for the construct, despite its settings being optimized. Slic3r was able to generate concentric rings shown in Figure 4.5B, but such a pattern suffered from needle deflection and ended up causing fusion/closure of the duct seen in Figure 4.5C.

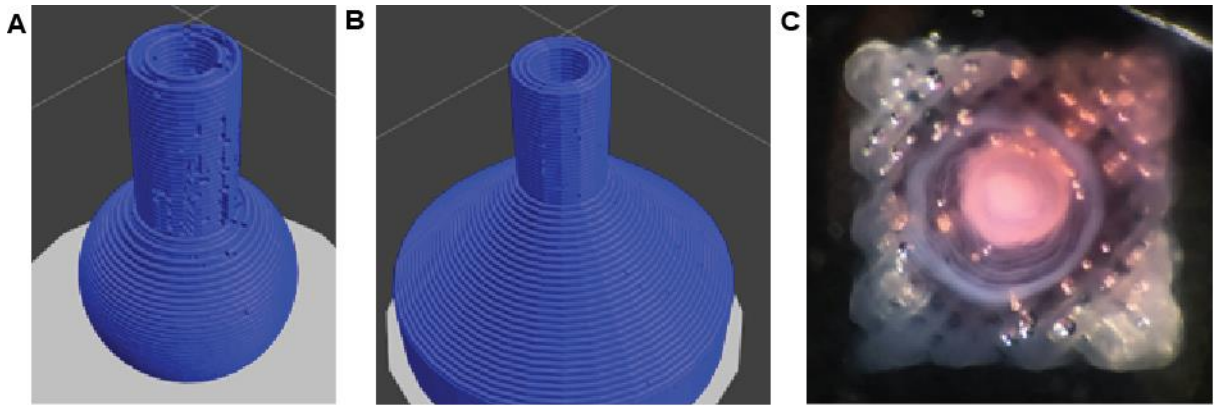

Figure 4.5 Troubleshooting slicer processing of MK2 mammary duct module. (A) Cura software was not able to process the MK2 duct section into concentric circular paths. **(B)** Slic3r could process the MK2 duct section into concentric circular paths. **(C)** Due to the deflection of the needle used to extrude the collagen component in this MK2, the collagen duct was closed after printing. The total width of the construct is 8 mm.

Mitigating deflection of a small-diameter, 1 in long needle is a complex problem to solve. During printing of an MK1 or MK2, the needle was encountering the slurry's yield stress and was not able to exert a force large enough to overcome it until, like a spring, it developed a large enough internal strain – the deflection. Without physically altering the needle, it was thought that the Gcode instructions could be geometrically "hacked" to encourage the needle to more easily slide through the slurry. Typically, yield-stress fluids such as Bingham Plastics and Herschel-Bulkley models allow for the yield stress to dip if the fluid experiences a harmonic force. This effect is attributable to physical vibrations interfering with the bonds associated with the yield stress of the material. For the regions of the MK2 construct that were the most prone to needle deflection, it was though that a fine rectilinear raster pattern like that shown in Figure 4.6 could be used to "jostle" the support and allow the needle to more easily progress. When this was applied to a couple of test prints of the MK2, it was found to be unsuccessful in resolving closure of the duct. Therefore, it was necessary to physically reinforce the needle.

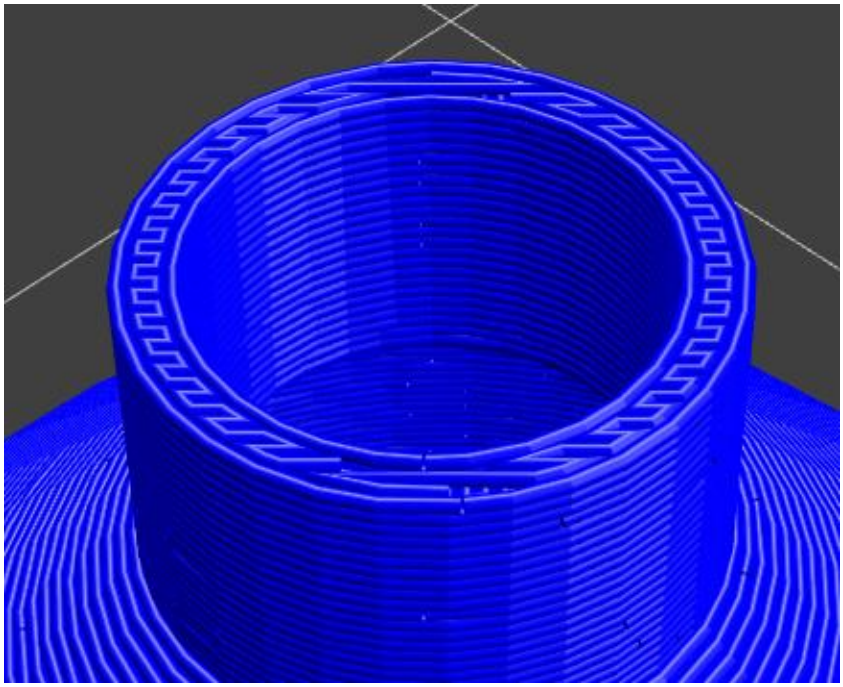

Figure 4.6 Utilization of rectilinear pathing in slicing software to offset needle deflection. The duct section of MK2 constructs could be "filled" with paths that are not concentric circles but instead rectilinear rastering that weakens the support material during a FRESH print and allows for a needle to more easily push between the support material particles.

The 80 µm needle shown in Figure 4.7A was much stiffer after being reinforced (Figure 4.7B), and this allowed it to render structures like that in Figure 4.3 but without closure of the duct (Figure 4.7C). Such a fused duct would not allow a seeding suspension of cells to enter the interior of the construct. This fusion is attributable to delayed tracking or lagging of the needle's tip with respect to the syringe/extruder body, causing it to follow a smaller circular path. The unreinforced needle was thin- and long-enough to deflect during its passage through slurry while printing. Deflection and lagging, common before the reinforcement of the needle, would cause all movements of the extruder to misrepresent the intentions of the Gcode. Because this deflection is present regardless of the strength of nozzle material used, it is important to minimize this phenomenon by selecting a nozzle material/construction that is as stiff as possible.

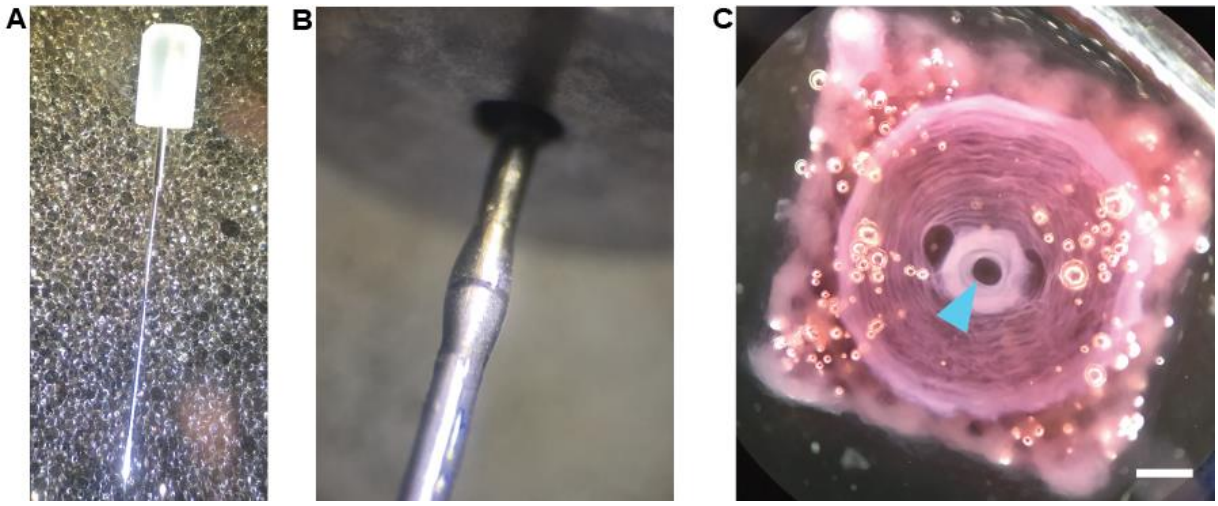

Figure 4.7 Physically reinforced needle produces better print outcome. (A) An un-reinforced 80 µm needle supplied by Hamilton for their GasTight® line of syringes with removable needle compression fittings. The glass ferrule is visible at the top, along with the slightly thicker section of metal just below the ferrule. The bottom of this needle is very flexible compared to standard luer-lock disposable deposition tips available from a large variety of suppliers. **(B)** A 250 µm needle removed from a luer fitting is slid over the 80 µm needle until it contacts the thicker metal near the glass ferrule in (A) and epoxied in place. Epoxy is visible as a bulge of clear material near the seam of the 80 µm needle (top) and the length of 250 µm needle (bottom) **(C)** The resulting MK2 print performed with a reinforced 80 µm needle shows an open duct when looking from above, and the overall diameter of collagen paths is larger due the improved tracking of the 80 µm needle. Scale bar is 1 mm.

After the collagen extruder's needle was reinforced, MK2 constructs created in a coacervate slurry possessed perfectly concentric circular extrusions of collagen, with little to no deflection or lagging of the extrusion visible. This quality of output is largely attributable to both the extra-fine texture of the coacervate, which has monodisperse, microscopic particles and the attention paid to alignment of separate extruder needles pre-print. The exterior of MK1 and MK2 constructs possessed a square profile with the 90° crosshatch pattern of alginate mesh. The rim of the funnel nearly always possessed a diameter within 1% of the intended value. Initial data shows that the internal diameter of the duct falls within approximately 2% of its intended value. The same data indicates that when the prints were released, post-culture, they were found to

possess buds that were always within 2% of the intended diameter of the file used to print them. Additional experimentation is still required to produce a statistically significant body of data.

As the diameter of a given print "feature" shrinks, the difficulty in rendering it increases until it is merely a point of extrusion without any outline or infill definition. Below a given size, it is impossible for a fixed diameter extruder to render. Most of this difficulty is due to the lack of responsiveness in a given 3D printer's hardware. The steppers used to drive a printer are generally operating under $1/16^{th}$ microstepping and are capable of only 10-15 µm movements using a significantly diminished peak torque. When rendering tiny features, printers often struggle to overcome the forces of static and kinetic friction associated with low cost sintered bronze bearings riding on stainless steel rods. Stronger motors can be substituted, but stronger motors often cause vibrations in the motion systems unless they are driven by very expensive interpolating chopper drivers such as Trinamic® IC's. This challenge of actuation mechanism design extends to the syringe pump as well, and, while the Replistruder iterations are designed to work with extremely small movements, they are not perfect. Even after accounting for the flexibility of the Replistruder, it is necessary to design as many fail-safes into the printer as possible. The ability of the Replistruder to utilize a 100 µL syringe was a key factor in contributing to the success of MK2 prints, despite the challenges associated with thin needles. Additionally, the ability of the firmware used on the Duet printer to support on-the-fly changes in acceleration, motor current, and values for instantaneous velocity change made the optimization of printer performance significantly smoother than any other machine in our experience.

The most challenging features for a given print are those that are essentially small punctate extrusions with little to no "filament"-like qualities to them. For any hardware, these

kinds of features are an excellent benchmark of extrusion control. As such, a perfect storm for any printer would essentially be a set of punctate extrusions. Trying to extrude such a small volume of ink that the result is a point of material rather than a filamentous extrusion pushes the hardware to be perfectly responsive in stopping and starting extrusion without accidentally jamming the nozzle with solidified ink. This use of an extruder like the Replistruder is counter to its design and is often reserved for jetting systems. In theory, any printer is capable of doing this, but a test like this often causes minor performance factors such as ink gas content and transmission friction to pile up and obscure operation.

We pushed our 3D printers to their conceivable limits by fabricating 200% scale ductal trees from collagen type I, collectively referred to as "MK4". The files used to generate these trees were processed through several iterations of workflow that eventually resulted in a continuous, manifold mesh without visible tiling artifacts, stacking artifacts, or floating solids shown below in Figure 4.8A. The file was scaled to 200% to allow the Replistruder to render a significant portion of the construct using a filamentous extrusion shown in the Gcode in Figure 4.8B rather than as punctate depositions.

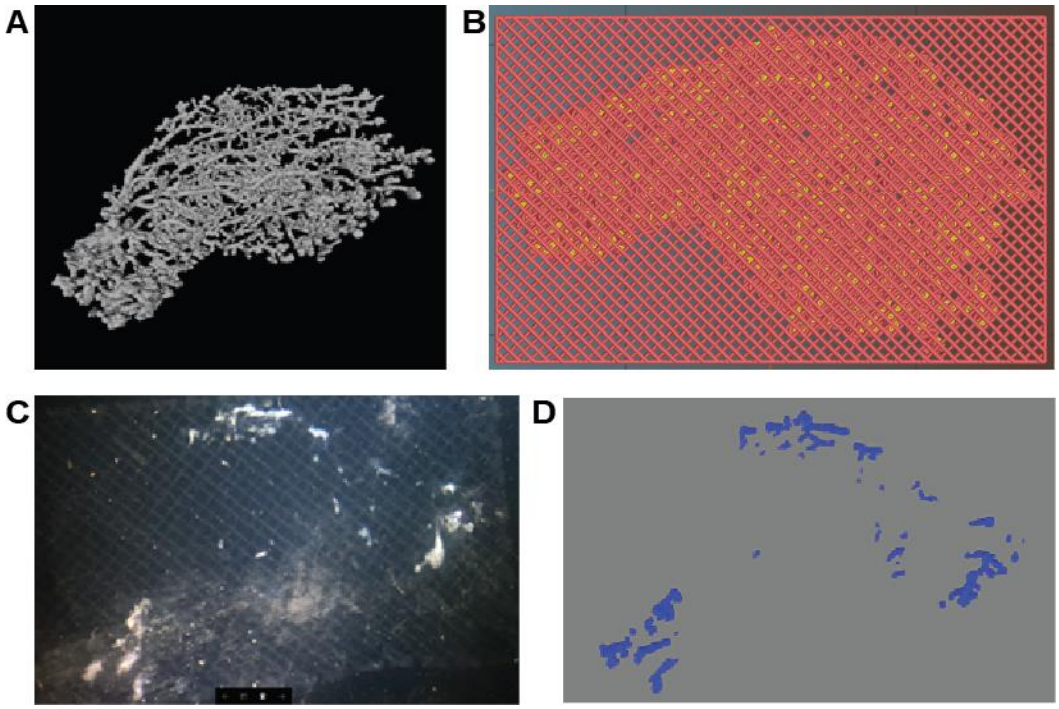

Figure 4.8 Producing Gcode for and troubleshooting a biomimetic mammary duct module. **(A)** A 6 wk. old KK/hlJ mammary duct is imaged and turned into this STL mesh representing the single largest connected surface which is, in turn, representative of the entire ductal tree. **(B)** Example Slic3r Gcode processing of (A), showing Collagen in yellow and alginate in red. **(C)** Printing the first 8 layers of the Gcode in (B) shows poor replication of collagen structures, which should appear like **(D)** The Gcode for the first 8 layers of collagen extrusion.

Executing the first few layers of the above Gcode using the settings that worked best for the MK2 resulted in collagen extrusions shown below in Figure 4.8C that did not resemble the Gcode portion sent to the printer (Figure 4.8D). The poor quality of collagen extrusion shown in Figure 4.8C was attributed to subtle vibrations of the extruder tips along the Z axis during movement in the XY plane. These vibrations were thought to be caused by the formation and disappearance of moments on the extruder during faster movements. To account for this and other challenges presented by this print – namely, the Duet printer's imprecise fabrication and operation along with the ludicrous amount of detail required for this print, it was decided to slow down the acceleration and instantaneous speed change settings to roughly half of their normal values. Additionally, the motors were provided with lower amounts of current to "smooth" out

movements. Finally, the density of the alginate mesh support was increased from the 20% used in the MK2 to 40%, providing much more support for collagen extrusions after release from the FRESH support bath. Slower machine movements along with denser alginate mesh improved print quality substantially, resulting in the print shown in Figure 4.9A. This MK4 developing mammary duct model represents a world-first level of complexity generated using a bioprinter with multiple endogenous ECM components. It is believed that no other method or machine can print this construct without significant adaptation, and yet the estimated cost of the entire system with materials is less than any commercially available bioprinting system. The MK4 print took approximately 2 hours to finish. Even at this slow rate, this print was printed faster than any commercial bioprinter could manage. A map of the printed construct generated using reflectance imaging tile scanning showed that features throughout the model were preserved in the output, shown below in Figure 4.9B & 4.9C. Distances measured between fiduciary regions of the file and print, shown highlighted with red stars in Figure 4.9B, indicated that the print underwent a roughly 4% shrinkage from its starting size. However, the shrinkage between fiduciary regions does not vary across at least one print. Repetition of these measurements are needed to confirm the maintenance of fidelity between file and print. Close-ups (Figure 4.9D) of

the bottom left of the Gcode and the print's reflectance image in Figure 4.9 show that there is apparent visual fidelity between the Gcode and the print at areas of high detail.

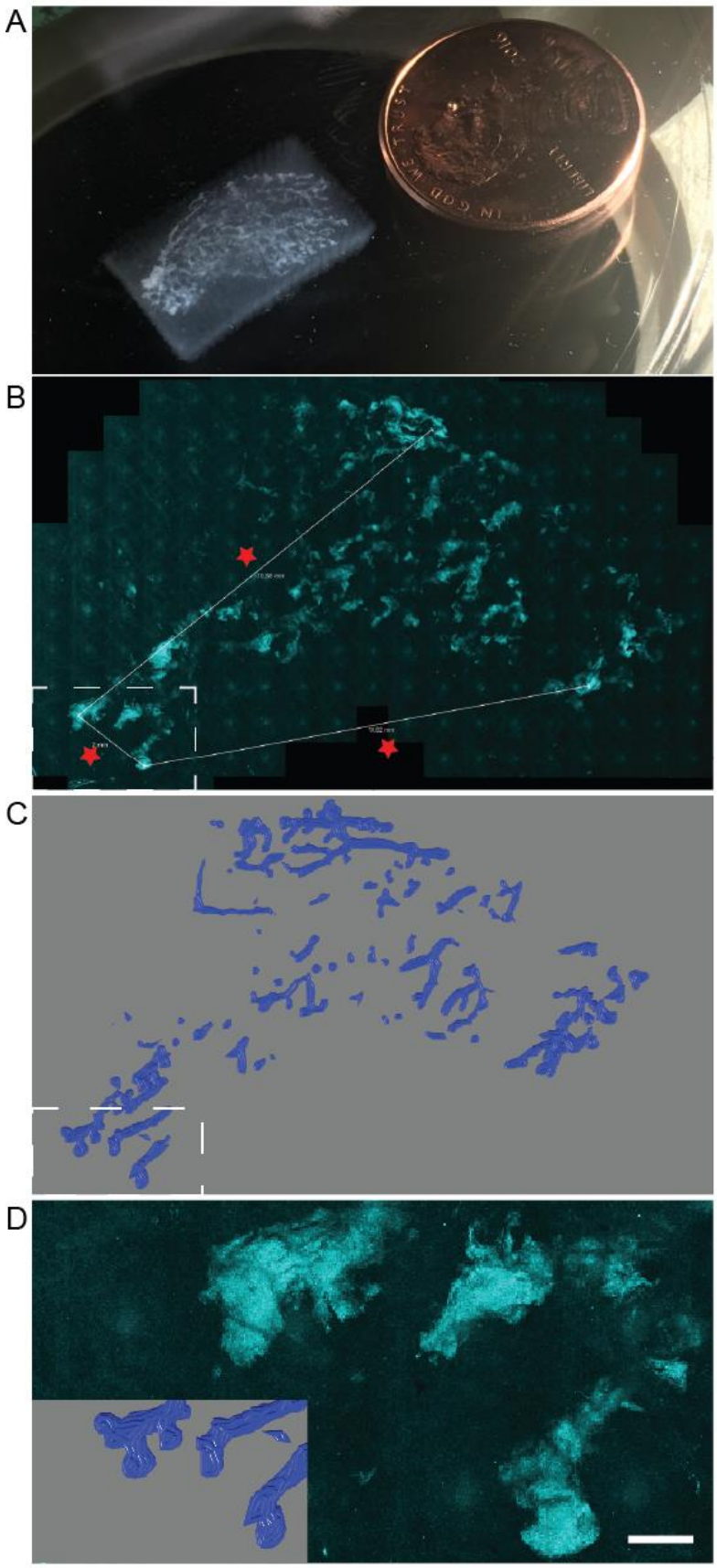

Figure 4.9 Biomimetic mammary duct print. (A) Shown submerged is the fully printed biomimetic collagen and alginate print of the file shown in Figure 4.8. The U.S. penny for scale shows that the print is faithful to the size of its file – 19 mm x 12 mm x 4 mm. **(B)** A max intensity projection of a reflectance tile scan shows that the print maintains fidelity in the first 12 layers of the print. The dashed box indicates an area shown in (D) Red stars indicate measured distances between fiduciary regions of the object. **(C)** Gcode of the first few layers of the print, showing the print maintains fidelity. Dashed box indicates area shown in **(D)** Close-up of the bottom left of (B & C) for comparison. Scale bar is 250 µm.

A printed construct such as the MK2 duct or the MK4 tree could serve as a complex starting

point for fabricating a complete model of duct development and potentially cancer *in vitro*. The walls of a construct such as this are thin enough (≤ 200 µm) that nutrient transport would not require vascularization. To fully utilize this model, many different support systems including perfusion culture and the endocrine effects of associated cell populations and stromal matrices would need to be incorporated. Even considering the challenges ahead, this model presents a complete solution to the mesoscale geometric complexity of branching epithelial networks.

4.4.2 Seeded Multi-material Constructs Possess an Internal Layer of Cells and an Open Lumen

It wasn't known if the method of gravity seeding the constructs would result in the formation of a monolayer of cells on the inside surface of the collagen component. Fluorescent images of cells seeded into the constructs showed that cells did not always reach the duct and the end bud. It is thought that, occasionally, gelatin solution from the melting of the FRESH support bath does not entirely clear the duct and bud during post processing. In cases where gelatin may remain in the throat of the duct, it could prevent cell solution from entering the construct due to its viscosity. This blockage of cell suspension results in the seeded cells populating only the top portion of the duct and the funnel, as shown in Figure 4.10A. MCF7 cells expressing GFP are shown completely covering the surface of the funnel in Figure 4.10B.

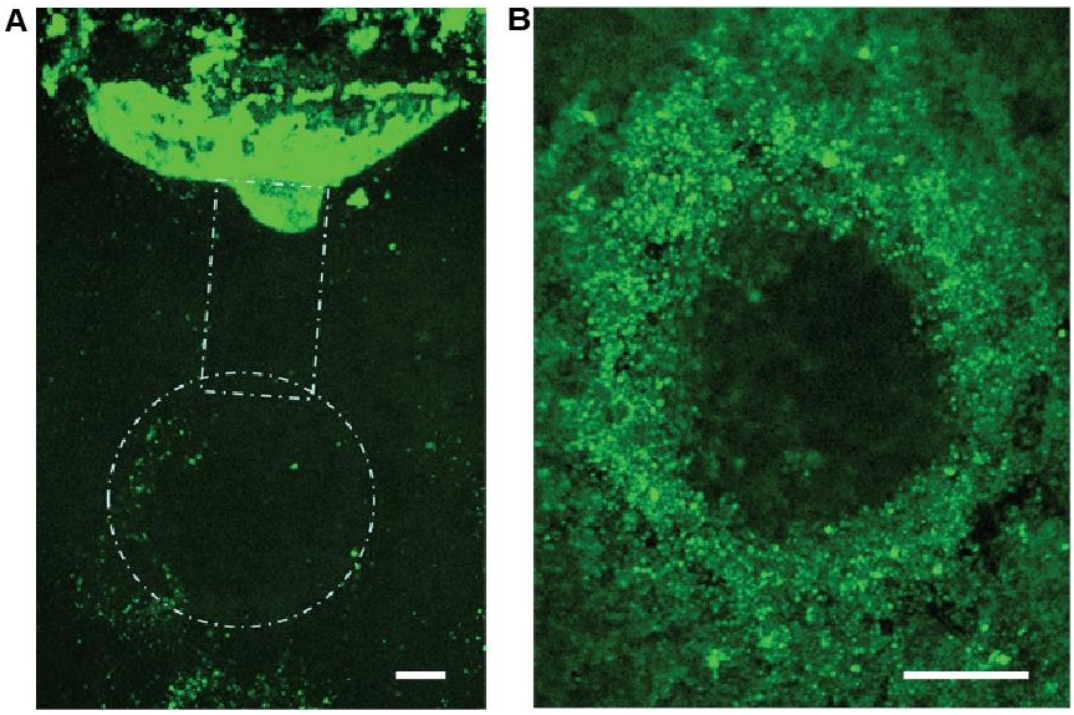

Figure 4.10 Seeding MK2 constructs can fail if the central tube of the construct is blocked with molten gelatin. (A) After a week of culture, MCF7 cells expressing GFP are shown to crowd the entrance to the MK2 construct, the rest of which is shown outlined in white dotted lines. It is thought that the cell suspension used to seed this construct could not enter the central tube and the terminal bud due to gelatin or excess hydrogel blocking the central tube. **(B)** A view from the top of the MK2 showing MCF7 cells adhered and growing in clusters around the entrance to the central tube. Scale bars are 1 mm.

In constructs seeded with MCF7 cells, fluorescence of cells was punctate and indicative of cells not covering the entire collagen surface inside the construct. Instead, cells grew in clusters, and the population of cells lining the duct and mouth of the funnel appeared rough, not possessing a smooth lumenal surface, as seen in Figure 4.10B. In cultures of MCF10A cells, cell spreading on the constructs was much more pronounced, and cells formed a much smoother lumen shown in Figure 4.11.

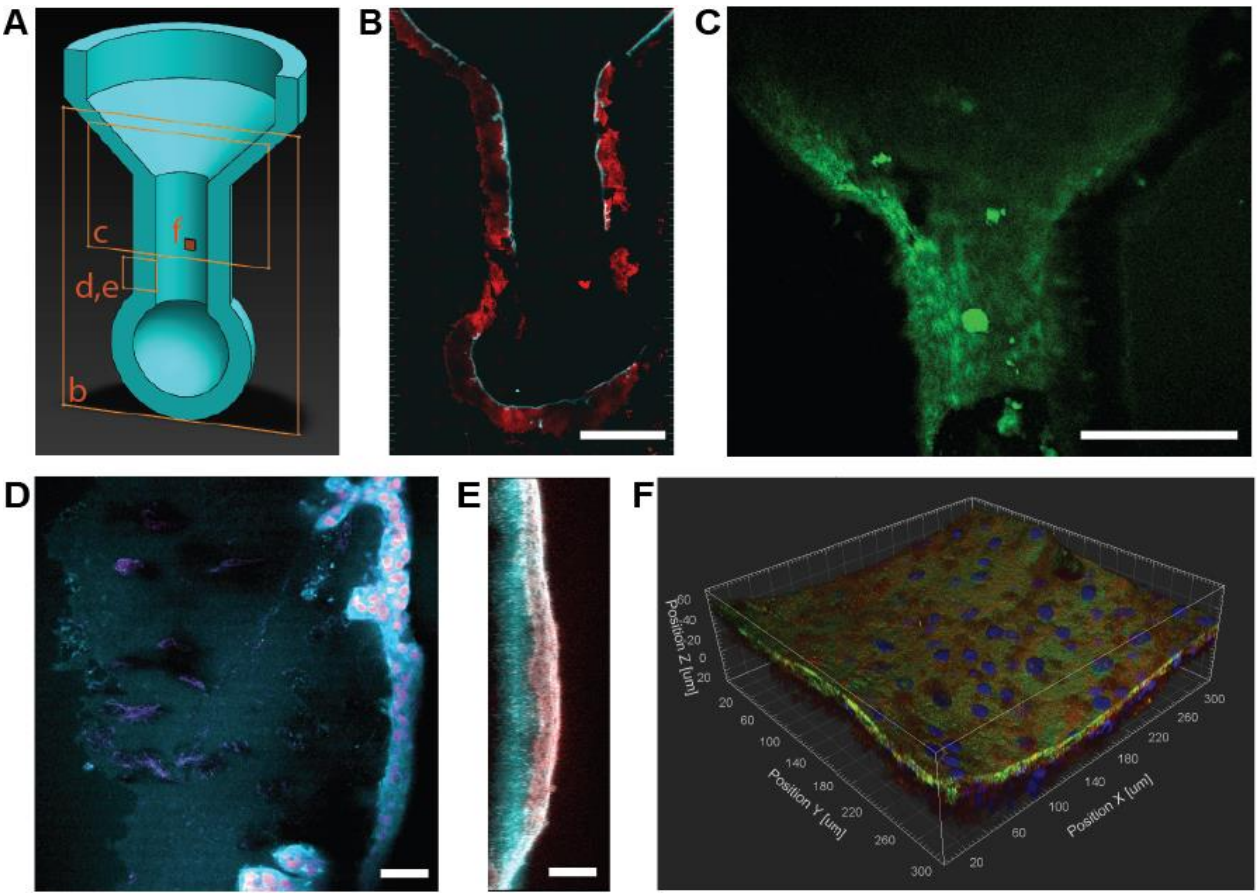

Figure 4.11 An epithelium of MCF10a cells coats the interior surface of a MK2. (A) The MK2 shown with a cutaway to illustrate the regions imaged and shown in (B-F) **(B)** Collagen reflectance shown in red and GFP expression of MCF10a cells shown in cyan demonstrates the presence of a thin, continuous epithelium situated at the inside border of printed collagen hydrogel. **(C)** A max intensity projection of the MK2 shown in (A) which displays a coating of GFP-expressing MCF10A cells on the internal surface of the collagen. For (A) and (B) Scale bars are 1 mm. **(D)** Cyan actin (phalloidin) fluorescence with nuclei (DAPI) shown in magenta. The epithelium shows evidence of invading the collagen layers, as is shown by appendages of the epithelium extending from the lumenal side (right) into the collagen. The exterior border of collagen is visible on the left of the image as a slight cyan fluorescence coming from overlap of the eosin fluorescence with actin fluorescence. Scale bar is 100 µm. **(E)** Another view of the epithelium showing cyan protein stain (eosin) and magenta actin (phalloidin) fluorescence with a clear boundary between cells and underlying collagen. Scale bar is 100 µm. **(F)** An isometric view of a z-stack of MK2 epithelium showing green actin (phalloidin), blue nuclei (DAPI), and red protein (eosin) fluorescence.

The number of cells required to get adequate coverage of the collagen surfaces inside the construct was quite substantial – 50,000 cells per construct. MCF10A's expressing GFP were visibly covering the interior of the duct and bud, shown in Figure 4.11B & C. Gravity

seeding constructs did not result in cells lining the top side of the bud, which is to be expected since settling cells will not have access to this portion of the construct. Interestingly, however, cells populated every other interior surface including the vertical walls of the duct tube. During culture, it may have been possible for cells to spread through defects to the outer surface, but no significant fluorescence was seen on collagen component exteriors. However, it is evident in Figure 4.11D that MCF10A cells are invading the collagen wall and are capable of smoothing the chaotic surface of the collagen which is slightly visible as a fuzzy cyan border on the left side of the image. In Figure 4.11E, the border between cells and collagen is clearly visible, but this was not the case for the entire construct. A representative picture of epithelium on the interior surface, shown in Figure 4.11F, indicates that the cells form a smooth, multi-layered surface of cells regardless of the underlying collagen. Many iterations of seeding and MK2 design/print process were utilized to arrive at the current results. It is believed that the current seeding method will only benefit from higher cell numbers, and future plans include many replicates for the sake of obtaining statistically powerful insights on the nature of these rapidly prototyped tissues.

4.4.3 Constructs Retain their Geometry Through Culture

One concern regarding these constructs was whether the cells would compact the collagen component and cause a loss of structure. In all cases, constructs showed some degree of delamination between the alginate and collagen sections of the constructs visible at the rim of the funnel (Figure 4.12), regardless of cell type used. It is thought that this disconnection was the result of the collagen-alginate connection being particularly weak at the rim of the funnel. In

future iterations of the construct, it would be straightforward to completely embed the rim of the construct into the surrounding alginate mesh fibers, thereby preventing it from disconnecting. To investigate the effects of cells on the interior dimensions of the collagen component, it will be necessary to repeat these experiments and utilize a tomographic imaging approach to resolve internal architecture. This is already being pursued in collaboration with Prof. Darryl Hadsell's group at Baylor College.

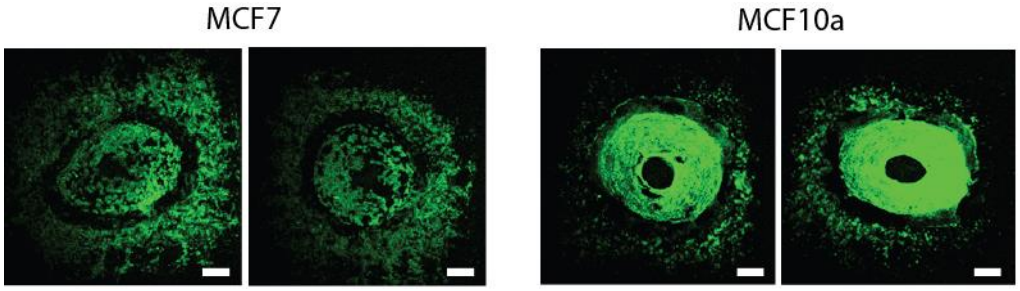

Figure 4.12 Delamination of collagen is consistent across constructs seeded and cultured for a week. MK2 constructs shown on the left were cultured with MCF7 cells, and constructs on the left were cultured with MCF10a cells. In all constructs, a gap of cells was visible around the top rim of collagen, indicating that the collagen was originally there but pulled away under the action of cells. Otherwise, we would expect to see cells scattered around the edge of the rim on all regions of top-side alginate. Scale bars are 1 mm.

4.5 Conclusion

It was hoped that cell solution dumped into the funnel of a construct would perfuse the construct and exit through pores or defects present in the collagen component, leaving behind cells much like dirt remains in a filter after mud passes through. According to the results in this chapter, this appears to be the case, as cells line most the interior surfaces without occupying the exterior. Additionally, it was hoped that the geometry of the construct would remain preserved through the passive action of surrounding alginate mesh. It appears that the construct retained its geometry for at least one week in culture. Whether this maintenance of fidelity is

possible during longer culture is not certain and would require further experimentation. Finally, we showed that it is possible to push our hardware to produce mesoscale branching epithelial tree models using this multi-material gel reinforcement approach. It can be concluded that creating an extraordinarily complex, parametric, and branching network of collagen tubes seeded with cells is possible using FRESH and open source hardware/software. Moreover, it is possible to culture these constructs for at least a week while retaining geometric fidelity. These conclusions set the stage for further fabrication of complex multi-material prints with more than just two materials, potentially allowing the selective placement of cells and different endogenous ECM components throughout a given construct.

Chapter 5 Summary and Future Directions

5.1 Summary

The primary goal of this effort was to investigate the potential of FRESH as a method for rendering complex scaffolds from soft hydrogel materials frequently used in tissue engineering. Herein, we have described various methods for converting complex 3D data to ECM hydrogel with unparalleled fidelity. For the field of bioprinting, this thesis establishes a path by which one can assemble one or more hydrogels into complex forms. For tissue engineering, this thesis contains the knowledge necessary to freeform arrange gelling cell suspensions without geometric constraint. Finally, in the scope of additive manufacturing, the results contained in this work are a series of world firsts necessary to begin innovating the 3D printing processes for gels.

In Chapter 2, it was shown that common FDM 3D printers can be modified to utilize fluid extrusion without compromising in control. Most importantly, the behavior of modified 3D printers was consistent with FDM theory, and this allowed us to rely on them for 3D printing fluids without developing a separate understanding for an unexpected, brand-new paradigm. Through a mastery of FDM, we were able to optimize the designs of various components of the modified machines to best fit our needs for responsiveness and ease-of-use while retaining the most convenient aspects of these machines – their compatibility and flexibility inherited from open source software and hardware ecosystems. In turn, our designs were reconnected to the open source repositories, allowing anyone with a sufficient understanding of 3D printer modification to adopt our methods.

In Chapter 3, a new method for printing gels, FRESH, was combined with the creations in Chapter 2 to fabricate scaffolds with levels of complexity hereto unforeseen in 3D bioprinting. First, the FRESH method is analyzed for failure modes using a variety of prints that are designed to test the critical faculties of bioprinting hydrogels. Optimization of the FRESH method follows, allowing us to print the benchmark Elliptical Window Calibration print and set the stage for printing biological shapes. Then, scale models of a human femur, heart, brain, an embryonic heart, and a branch of an arterial tree were fabricated from the gold-standard tissue engineering materials Collagen type I, Alginate, Fibrin, Matrigel®, and Hyaluronic Acid. Function of the arterial tree is proven using perfusion, and viability of cells in printed constructs is shown to be 99.7%, comparable to cell culture. Finally, multiple materials are combined in multi-component prints to demonstrate the synergistic effects offered by novel ink combinations over monolithic composition. Before these prints, there was no known example of 3D bioprinting or any other method that was conducive to 3D printing manifold hydrogel structures with organic curvatures representative of their in vivo counterparts. Given the first step taken in adopting the functions of tissues is often mimicry, recapitulating the forms of biological function is paramount in engineering tissues that survive outside their complete organism. The implications of a lone method that allows for complete geometric freedom in assembling gels are grand – they imply this work forms a bedrock for future engineering of complex tissues. To our knowledge, there is no other way to program biological matter with biomimetic complexity without utilizing the FRESH method of additive manufacturing.

Chapter 4 establishes FRESH's potential to create tissues on top of the efforts in Chapter 3 to characterize its principle strengths and weaknesses. First, a mimetic model of a developing

epithelial tree is generated from 3D imaging data, and a parametric model of a mammary duct is generated in CAD. Together, these two models represent the short and long-term goals of bioprinting using fragile ECM gels. The parametric model MK2 demonstrates that 3D printed collagen type I maintains its programmed geometry over a week of culture and allows for the formation of a cell monolayer mimicking the parametric design. Regarding the long-term capabilities of FRESH, the mimetic model MK4 constitutes an entire scale ductal tree printed from collagen with features that are nigh-impossible to fabricate on any available bioprinting system using any method. In the MK2, alginate fibers that maintain the collagen component's geometry over the course of cell culture and fixation are removed and allow the entirety of the construct to be sectioned and imaged. In the MK4, alginate fibers maintain the extremely fragile collagen tree during handling and imaging – a feat otherwise impossible without some sort of included embedding medium such as agarose or collagen. The speed, precision, and ease-of-use of this method of modeling complex tissue geometry in collagen, alginate, and cells allows us to practically approach tissue rapid prototyping (as evidenced by the multiple iterations of MK1 and MK2 tissue design) for the first time ever in the history of tissue engineering.

The contents of this thesis offer a roadmap for low-cost rapid prototyping of tissues in a laboratory setting; furthermore, they encourage dissemination using open source hardwares, softwares, and data.

5.2 Future Directions

In the process of executing the contents of this thesis, I have come to understand several important limitations of FRESH and its application toward modeling mammary ductal epithelium.

I have thus sought to establish key experiments, which, if undertaken, would address these limitations by providing insight or complete solutions. If these limitations were addressed, then tissue prototyping of MK2 and MK4 constructs would stand alone as a publishable body of work in a high impact journal.

First and foremost, among the problems not addressed in this thesis are the limitations of the hardware used in FRESH. Aside from the Replistruder, which represents a highly-optimized design for FDM fabrication using syringes, the 3D printers including MakerBots, Printrbots, and a custom Duet-based system utilize linear motion systems that are appropriately engineered to shuttle a finite-mass extruder payload in XY motion with a fixed level of accuracy and precision. The modified Replistruder extruders, when mounted on the extruder carriages of these printers, often increase the payload mass to a value that stresses the acceleration, jerk, and vibration limits of the host machine. A printer could have its skeleton reinforced with stiffer components and stronger motors to account for this increase in payload. The simplest method of accomplishing this reinforcement would require thicker rods and carriage brackets in the linear systems of the Duet printer. Second to this would be an increase in motor current and 1/256 interpolation of $1/16^{th}$ microstepping by adoption of more modern stepper driver IC's on the motherboard. The result would hypothetically result in fewer motion artifacts and allow for prints of objects like the MK4 ductal tree at speeds typically reserved for prints such as the MK2. Resolution would theoretically approach 2.5 µm movements with an unknown precision. Ball bearings substituted for the stock bronze bushings would further increase the operational limits of the system by eliminating play, chatter, and stiction along the XY axes. Strengthening the entire printer would result not only in better actuation but also the capacity for more than two extruders. which are

already supported by the electronics utilized in the Duet printer. This "upgrade" to the current hardware platform used for multi-material prints is possible with the acquisition of a set of replacement linear rods, associated ball bearings, and a Duet WiFi motherboard (features higher-current stepper drivers with 1/256th interpolation; duet3d.com). Installation of these components on the Duet based printer would require a few custom-designed parts, but, given the history of modifying 3D printers in our lab, it would likely not prove very difficult to accomplish. This upgrade may, in fact, be necessary to produce data for the MK4 ductal tree that is polished enough for a publication.

The secondary limitation I would address is the difficulty in manufacturing the support material used in FRESH printing. The support material is the key to the FRESH method's success, but consistently fabricating large volumes of sterile, fine, monodisperse gelatin particulate slurries using coacervation is currently out of our reach. Coacervate slurries are translucent to opaque, and this lack of transparency hinders gauging of the FRESH printing process. Fabricating a more transparent slurry is possible using a few experimental methods of altering coacervation conditions, but these other versions of coacervation are more sensitive to subtle variations in temperature, pH, and other reaction conditions. To standardize our slurry manufacturing and processing, it would be necessary to invest in better equipment for carefully controlling and measuring the reaction conditions during coacervation. We could feasibly invest in an inline mixer, a pH probe, a thermocouple, and a large, insulated vat to set up a batch reactor capable of carefully controlling the variables necessary to produce a transparent and sterile coacervate.

Making a more realistic duct for study of DCIS invasion in culture will require the ability to generate high-resolution heterogeneous collagen structures. Tumor associated collagen

signatures such as TACS – 3, where dense collagen fibers are seen to radiate from the central tumor body, are considered hallmarks of tumor invasiveness. Incorporating these collagen signatures into a realistic duct module for culture of DCIS would require a higher resolution system capable of generating sub-100 µm-long fibrils with less than 20 µm width – effectively, a 20 µm nozzle would be needed. These high aspect ratio collagen fibrils could be situated around the duct in a fashion mimicking TACS – 3. This "abnormal" construct with heterogenous collagen shown in would contrast with the current "normal" duct design which features nearly homogenous collagen arranged as a perimeter to the duct's lumen.

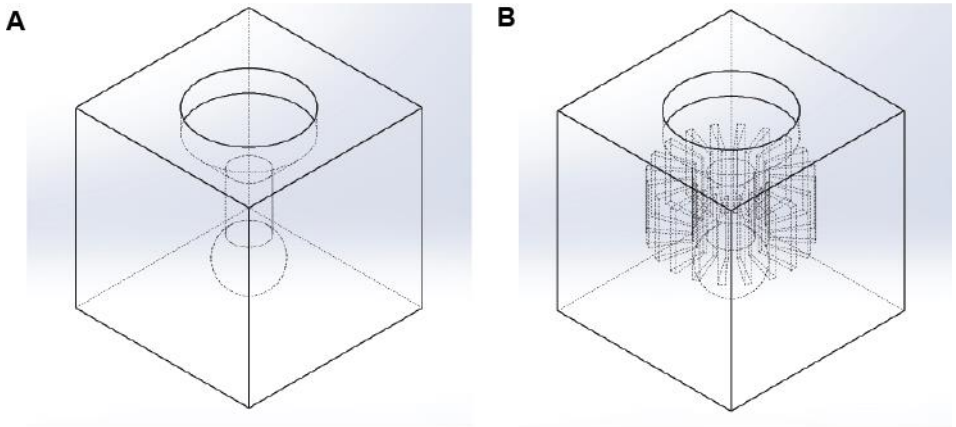

Figure 5.1Normal vs. Abnormal Mammary Duct Module MK2 (A) Normal MK2 module has collagen situated as shown in previous diagrams/figures – as a central tube with a funnel leading through a ductal tube to a dead end bud. **(B)** The abnormal MK2 has collagen oriented radially to the body of the duct, potentially allowing for or encouraging invasion of any included DCIS cells out of the duct.

Working with better hardware and a transparent, sterile slurry would allow us to quickly address the third primary limitation of this work – the duration of cell culture. MK2 constructs cultured for a week showed subtle delaminations between components of the constructs. To fix this, it will be necessary to further iterate the MK2 duct model to include more adhesion between collagen and alginate components. MK3 constructs can then be cultured with various populations of mammary epithelial cells for periods longer than a week to test if collagen delamination is

effectively resisted by the newer generation of construct. If monolayers of epithelial cells are generated and retained in each geometry for long enough, it would make the MK3 a suitable candidate for modeling the ductal epithelium *in vitro*. Such a model would constitute a first – a rapidly prototyped tissue, designed for and produced by FRESH printing and capable of mimicking a tissue that currently relies on animal models for drug testing and cancer modeling. Taking our MK3 tissue one step further, we could introduce an invasive carcinoma into the lumen of the tissue and monitor its interaction with the MK3. To my knowledge, demonstrating "invasion" in a truly three-dimensional 3D bioprinted tissue would be groundbreaking. It would then be a logical extension of our efforts to compound the simple geometry of the MK3 into a more complex construct such as the MK4 ductal tree.

References:

1. Allred, D. C. Ductal carcinoma in situ: Terminology, classification, and natural history. *J. Natl. Cancer Inst. - Monogr.* 134–138, 2010.doi:10.1093/jncimonographs/lgq035
2. Baxter, N. N., B. a Virnig, S. B. Durham, and T. M. Tuttle. Trends in the treatment of ductal carcinoma in situ of the breast. *J. Natl. Cancer Inst.* 96:443–448, 2004.
3. Bhatia, S. K., and S. Sharma. 3D-printed prosthetics roll off the presses. *Chem. Eng. Prog.* 110:28–33, 2014.
4. Bhatia, S. N., and D. E. Ingber. Microfluidic organs-on-chips. *Nat. Biotechnol.* 32:760–772, 2014.
5. Bhattacharjee, T., S. M. Zehnder, K. G. Rowe, S. Jain, R. M. Nixon, W. G. Sawyer, and T. E. Angelini. Writing in the granular gel medium. *Sci. Adv.* 1:e1500655–e1500655, 2015.
6. Bischel, L. L., D. J. Beebe, and K. E. Sung. Microfluidic model of ductal carcinoma in situ with 3D, organotypic structure. *BMC Cancer* 15:12, 2015.
7. Boghaert, E., D. C. Radisky, and C. M. Nelson. Lattice-Based Model of Ductal Carcinoma In Situ Suggests Rules for Breast Cancer Progression to an Invasive State. 10:, 2014.
8. Cekanova, M., and K. Rathore. Animal models and therapeutic molecular targets of cancer: Utility and limitations. *Drug Des. Devel. Ther.* 8:1911–1922, 2014.
9. Chia, H. N., and B. M. Wu. Recent advances in 3D printing of biomaterials. *J. Biol. Eng.* 9:1–14, 2015.
10. Choi, N. W., M. Cabodi, B. Held, J. P. Gleghorn, L. J. Bonassar, and A. D. Stroock. Microfluidic scaffolds for tissue engineering. *Nat. Mater.* 6:908–15, 2007.
11. Choi, Y., E. Hyun, J. Seo, C. Blundell, H. C. Kim, E. Lee, S. H. Lee, A. Moon, W. K. Moon, and D. Huh. A microengineered pathophysiological model of early-stage breast cancer. *Lab a Chip - Miniaturisation Chem. Biol.* 15:3350–3357, 2015.
12. Claus, E. B., M. Stowe, D. Carter, and T. Holford. The risk of a contralateral breast cancer among women diagnosed with ductal and lobular breast carcinoma in situ: Data from the Connecticut Tumor Registry. *Breast* 12:451–456, 2003.
13. Cocker, R., M. H. Oktay, J. L. Sunkara, and L. G. Koss. Mechanisms of progression of ductal carcinoma in situ of the breast to invasive cancer. A hypothesis. *Med. Hypotheses* 69:57–63, 2007.
14. Cohen, D. L., J. I. Lipton, L. J. Bonassar, and H. Lipson. Additive manufacturing for in situ repair of osteochondral defects. *Biofabrication* 2:35004, 2010.
15. Cohen, D. L., J. I. Lipton, L. J. Bonassar, and H. Lipson. Additive manufacturing for in situ repair of osteochondral defects. *Biofabrication* 2:35004, 2010.
16. Cowell, C. F., B. Weigelt, R. A. Sakr, C. K. Y. Ng, J. Hicks, T. A. King, and J. S. Reis-Filho. Progression from ductal carcinoma in situ to invasive breast cancer: Revisited. *Mol. Oncol.* 7:859–869, 2013.
17. Cui, X., and T. Boland. Human microvasculature fabrication using thermal inkjet printing technology. *Biomaterials* 30:, 2009.
18. Derby, B. Printing and prototyping of tissues and scaffolds. *Science* 338:921–6, 2012.
19. Dhimolea, E., M. V. Maffini, A. M. Soto, and C. Sonnenschein. The role of collagen reorganization on mammary epithelial morphogenesis in a 3D culture model. *Biomaterials* 31:3622–3630, 2010.

20. Duan, B., L. a Hockaday, K. H. Kang, and J. T. Butcher. 3D bioprinting of heterogeneous aortic valve conduits with alginate/gelatin hydrogels. *J. Biomed. Mater. Res. A* 101:1255–64, 2013.
21. Duan, B., E. Kapetanovic, L. a. Hockaday, and J. T. Butcher. Three-dimensional printed trileaflet valve conduits using biological hydrogels and human valve interstitial cells. *Acta Biomater.* 10:1836–1846, 2014.
22. Erbas, B., E. Provenzano, J. Armes, and D. Gertig. The natural history of ductal carcinoma in situ of the breast: A review. *Breast Cancer Res. Treat.* 97:135–144, 2006.
23. Ernster, V. L., J. Barclay, K. Kerlikowske, H. Wilkie, and R. Ballard-Barbash. Mortality among women with ductal carcinoma in situ of the breast in the population-based surveillance, epidemiology and end results program. *Arch Intern Med* 160:953–958, 2000.
24. FDA. FDA 510k Clearance Oxford Medical PEKK. , 2013.at <http://www.accessdata.fda.gov/cdrh_docs/pdf12/K121818.pdf>
25. Feigelson, H. S., N. M. Carroll, S. Weinmann, R. Haque, C.-L. Yu, M. G. Butler, B. Waitzfelder, M. G. Wrenn, A. Capra, E. a McGlynn, and L. a Habel. Treatment patterns for ductal carcinoma in situ from 2000–2010 across six integrated health plans. *Springerplus* 4:4–11, 2015.
26. Fullerton, J. N., G. C. M. Frodsham, and R. M. Day. 3D printing for the many, not the few. *Nat Biotech* 32:1086–1087, 2014.
27. Giraud, M.-N., C. Armbruster, T. Carrel, and H. T. Tevaearai. Current state of the art in myocardial tissue engineering. *Tissue Eng.* 13:1825–36, 2007.
28. Hadsell, D. L., L. A. Hadsell, W. Olea, M. Rijnkels, C. J. Creighton, I. Smyth, K. M. Short, L. L. Cox, and T. C. Cox. In-silico QTL mapping of postpubertal mammary ductal development in the mouse uncovers potential human breast cancer risk loci. *Mamm. Genome* 26:57–79, 2015.
29. Highley, C. B., C. B. Rodell, and J. a. Burdick. Direct 3D Printing of Shear-Thinning Hydrogels into Self-Healing Hydrogels. *Adv. Mater.* n/a-n/a, 2015.doi:10.1002/adma.201501234
30. Hinton, T. J., Q. Jallerat, R. N. Palchesko, J. H. Park, M. S. Grodzicki, H. Shue, M. H. Ramadan, A. R. Hudson, and A. W. Feinberg. Three-dimensional printing of complex biological structures by freeform reversible embedding of suspended hydrogels. , 2015.
31. Ho, C. M. B., S. H. Ng, K. H. H. Li, and Y.-J. Yoon. 3D printed microfluidics for biological applications. *Lab Chip* 15:3627–3637, 2015.
32. Hockaday, L. a, K. H. Kang, N. W. Colangelo, P. Y. C. Cheung, B. Duan, E. Malone, J. Wu, L. N. Girardi, L. J. Bonassar, H. Lipson, C. C. Chu, and J. T. Butcher. Rapid 3D printing of anatomically accurate and mechanically heterogeneous aortic valve hydrogel scaffolds. *Biofabrication* 4:35005, 2012.
33. Hooper, R. C., K. A. Hernandez, T. Boyko, A. Harper, J. Joyce, A. R. Golas, and J. A. Spector. Fabrication and In Vivo Microanastomosis of Vascularized Tissue-Engineered Constructs. 0:1–9, 2014.
34. Huang, G. Y., L. H. Zhou, Q. C. Zhang, Y. M. Chen, W. Sun, F. Xu, and T. J. Lu. Microfluidic hydrogels for tissue engineering. *Biofabrication* 3:12001, 2011.
35. Janakiraman, V., S. Sastry, J. R. Kadambi, and H. Baskaran. Experimental investigation and computational modeling of hydrodynamics in bifurcating microchannels. *Biomed. Microdevices* 10:355–365, 2008.

36. Jiang, K., C. Dong, Y. Xu, and liming wang. Microfluidic-based Biomimetic Models for Life Science Research. *RSC Adv.* 6:26863–26873, 2016.
37. Jones, R., P. Haufe, E. Sells, P. Iravani, V. Olliver, C. Palmer, and A. Bowyer. RepRap – the replicating rapid prototyper. *Robotica* 29:177–191, 2011.
38. Kittrell, F., K. Valdez, H. Elsarraj, Y. Hong, D. Medina, and F. Behbod. Mouse Mammary Intraductal (MIND) Method for Transplantation of Patient Derived Primary DCIS Cells and Cell Lines. *Bio-protocol* 6:e1744, 2016.
39. Kolesky, D. B., R. L. Truby, a S. Gladman, T. a Busbee, K. a Homan, and J. a Lewis. 3D Bioprinting of Vascularized, Heterogeneous Cell-Laden Tissue Constructs. *Adv. Mater.* 1–7, 2014.doi:10.1002/adma.201305506
40. Kukowska-Latallo, J. F. J., K. K. A. Candido, Z. Cao, S. S. Nigavekar, I. J. Majoros, T. P. Thomas, L. P. Balogh, M. K. Khan, and J. R. Baker. Nanoparticle targeting of anticancer drug improves therapeutic response in animal model of human epithelial cancer. *Cancer Res.* 65:5317–5324, 2005.
41. Lee, C. H., S. a Rodeo, L. A. Fortier, C. Lu, C. Erisken, and J. J. Mao. Protein-releasing polymeric scaffolds induce fibrochondrocytic differentiation of endogenous cells for knee meniscus regeneration in sheep. *Sci. Transl. Med.* 6:266ra171, 2014.
42. Legant, W. R., C. S. Chen, and V. Vogel. Force-induced fibronectin assembly and matrix remodeling in a 3D microtissue model of tissue morphogenesis. *Integr. Biol. (Camb).* 4:1164–74, 2012.
43. Ma, X., X. Qu, W. Zhu, Y.-S. Li, S. Yuan, H. Zhang, J. Liu, P. Wang, C. S. E. Lai, F. Zanella, G.-S. Feng, F. Sheikh, S. Chien, and S. Chen. Deterministically patterned biomimetic human iPSC-derived hepatic model via rapid 3D bioprinting. *Proc. Natl. Acad. Sci.* 113:2206–2211, 2016.
44. Malone, E., and H. Lipson. Fab@Home: the personal desktop fabricator kit. *Rapid Prototyp. J.* 13:245–255, 2007.
45. Mannoor, M. S., Z. Jiang, T. James, Y. L. Kong, K. a Malatesta, W. O. Soboyejo, N. Verma, D. H. Gracias, and M. C. McAlpine. 3D printed bionic ears. *Nano Lett.* 13:2634–9, 2013.
46. Mardekian, S. K., A. Bombonati, and J. P. Palazzo. Ductal carcinoma in situ of the breast: The importance of morphologic and molecular interactions. *Hum. Pathol.* 49:114–123, 2015.
47. Marga, F., K. Jakab, C. Khatiwala, B. Shepherd, S. Dorfman, B. Hubbard, S. Colbert, and F. Gabor. Toward engineering functional organ modules by additive manufacturing. *Biofabrication* 4:22001, 2012.
48. Mariotto, A. B., K. Robin Yabroff, Y. Shao, E. J. Feuer, and M. L. Brown. Projections of the cost of cancer care in the United States: 2010-2020. *J. Natl. Cancer Inst.* 103:117–128, 2011.
49. Martin, I. *et al.* Manufacturing challenges in regenerative medicine. *Sci. Transl. Med.* 6:232fs16, 2014.
50. Melchels, F. P. W., M. a. N. Domingos, T. J. Klein, J. Malda, P. J. Bartolo, and D. W. Hutmacher. Additive manufacturing of tissues and organs. *Prog. Polym. Sci.* 37:1079–1104, 2012.
51. Miller, J. S., K. R. Stevens, M. T. Yang, B. M. Baker, D.-H. T. Nguyen, D. M. Cohen, E. Toro, A. a. Chen, P. a. Galie, X. Yu, R. Chaturvedi, S. N. Bhatia, and C. S. Chen. Rapid casting of

patterned vascular networks for perfusable engineered three-dimensional tissues. *Nat. Mater.* 11:1–7, 2012.

52. Miller, J. S., K. R. Stevens, M. T. Yang, B. M. Baker, D. H. Nguyen, D. M. Cohen, E. Toro, A. A. Chen, P. A. Galie, X. Yu, R. Chaturvedi, S. N. Bhatia, and C. S. Chen. Rapid casting of patterned vascular networks for perfusable engineered three-dimensional tissues. *Nat Mater* 11:768–774, 2012.
53. Mitsuhashi, N., K. Fujieda, T. Tamura, S. Kawamoto, T. Takagi, and K. Okubo. BodyParts3D: 3D structure database for anatomical concepts. *Nucleic Acids Res.* 37:D782-5, 2009.
54. Murphy, S. V, and A. Atala. 3D bioprinting of tissues and organs. *Nat Biotech* 32:773–785, 2014.
55. Narod, S. A., J. Iqbal, V. Giannakeas, V. Sopik, and P. Sun. Breast Cancer Mortality After a Diagnosis of Ductal Carcinoma In Situ. *JAMA Oncol.* 1:888–896, 2015.
56. Norotte, C., F. S. Marga, L. E. Niklason, and G. Forgacs. Scaffold-free vascular tissue engineering using bioprinting. *Biomaterials* 30:, 2009.
57. Norotte, C., F. S. Marga, L. E. Niklason, and G. Forgacs. Scaffold-free vascular tissue engineering using bioprinting. *Biomaterials* 30:5910–7, 2009.
58. Osuala, K. O., M. Sameni, S. Shah, N. Aggarwal, M. L. Simonait, O. E. Franco, Y. Hong, S. W. Hayward, F. Behbod, R. R. Mattingly, and B. F. Sloane. Il-6 signaling between ductal carcinoma in situ cells and carcinoma-associated fibroblasts mediates tumor cell growth and migration. *BMC Cancer* 15:584, 2015.
59. Ott, H. C., T. S. Matthiesen, S.-K. Goh, L. D. Black, S. M. Kren, T. I. Netoff, and D. a Taylor. Perfusion-decellularized matrix: using nature's platform to engineer a bioartificial heart. *Nat. Med.* 14:213–221, 2008.
60. Ozbolat, I. T., and Y. Yu. Bioprinting toward organ fabrication: challenges and future trends. *IEEE Trans. Biomed. Eng.* 60:691–9, 2013.
61. Parikh, R. R., B. G. Haffty, D. Lannin, and M. S. Moran. Ductal carcinoma in situ with microinvasion: prognostic implications, long-term outcomes, and role of axillary evaluation. *Int. J. Radiat. Oncol. Biol. Phys.* 82:7–13, 2012.
62. Pati, F., J. Jang, D.-H. Ha, S. Won Kim, J.-W. Rhie, J.-H. Shim, D.-H. Kim, and D.-W. Cho. Printing three-dimensional tissue analogues with decellularized extracellular matrix bioink. *Nat. Commun.* 5:3935, 2014.
63. Provenzano, P. P., K. W. Eliceiri, J. M. Campbell, D. R. Inman, J. G. White, and P. J. Keely. Collagen reorganization at the tumor-stromal interface facilitates local invasion. *BMC Med.* 4:38, 2006.
64. Schneider, C. a, W. S. Rasband, and K. W. Eliceiri. NIH Image to ImageJ: 25 years of image analysis. *Nat. Methods* 9:671–675, 2012.
65. Shah, A. M., H. Jung, and S. Skirboll. Materials used in cranioplasty: a history and analysis. *Neurosurg Focus* 36:E19, 2014.
66. Sung, K. E., X. Su, E. Berthier, C. Pehlke, A. Friedl, and D. J. Beebe. Understanding the Impact of 2D and 3D Fibroblast Cultures on In Vitro Breast Cancer Models. *PLoS One* 8:1–13, 2013.
67. Takeda, Y. S., and Q. Xu. Fabrication of 2D and 3D Constructs From Reconstituted Decellularized Tissue Extracellular Matrices. *J. Biomed. Nanotechnol.* 10:3631–3637, 2014.
68. Tasoglu, S., and U. Demirci. Bioprinting for stem cell research. *Trends Biotechnol.* 31:10–9, 2013.

69. Tumbleston, J. R., D. Shirvanyants, N. Ermoshkin, R. Janusziewicz, A. R. Johnson, D. Kelly, K. Chen, R. Pinschmidt, J. P. Rolland, A. Ermoshkin, E. T. Samulski, and J. M. DeSimone. Continuous liquid interface production of 3D objects. *Science (80-.).* 347:1349, 2015.
70. Valdez, K. E., F. Fang, W. Smith, D. C. Allred, D. Medina, and F. Behbod. Human primary ductal carcinoma in situ (DCIS) subtype-specific pathology is preserved in a mouse intraductal (MIND) xenograft model. 225:565–573, 2012.
71. Watson, C. J. Involution: apoptosis and tissue remodelling that convert the mammary gland from milk factory to a quiescent organ. *Breast Cancer Res.* 8:203, 2006.
72. Yi, B., P. J. Williams, M. Niewolna, Y. Wang, and T. Yoneda. Tumor-derived PDGF-BB plays a critical role in osteosclerotic bone metastasis in an animal model of human breast cancer. *Cancer Res.* 62:917–923, 2002.
73. Zopf, D. A., S. J. Hollister, M. E. Nelson, R. G. Ohye, and G. E. Green. Bioresorbable Airway Splint Created with a Three-Dimensional Printer. *N. Engl. J. Med.* 368:2043–2045, 2013.
74. Transition to invasion in breast cancer: a microfluidic in vitro model enables examination of spatial and temporal effects. 18:1492–1501, 2011.

Appendix A : Publications, Presentations, and Posters

Publications:

D Richards. D Zemlyanoy. R Asrar. Y Chokshi. E Cook. **T Hinton**. X Lu. V Nguyen. N Patel. J Usher. S Vaidyanathan. D Yeung. A Ivanisevic. "DNA Immobilization on GaP(100) Investigated by Kelvin Probe Force Microscopy" The Journal of Physical Chemistry C, 114(36), 2010, pp 15486-15490

T Hinton. Q Jallerat. R Palchesko. JH Park. M Grodzicki. H Shue. M Ramadan. A Hudson. "Three-dimensional printing of complex biological structures by freeform reversible embedding of suspended hydrogels." Science Advances. 23 October 2015

T Hinton. A Hudson. K Pusch. A Lee. A Feinberg. "3D Printing PDMS Elastomer in a Hydrophilic Support Bath via Freeform Reversible Embedding." ACS Biomaterials Science & Engineering. 2(10), 2016, pp 1781-1786

T Hinton. A Lee. A Feinberg. "3D Bioprinting from the Micrometer to Millimeter Length Scales: Size Does Matter" Current Opinion in Biomedical Engineering. 2017

Presentations:

"3D Printing of Complex Scaffolds Using Freeform Reversible Embedding of Suspended Hydrogels (FRESH)" **T Hinton.** A Hudson. A Feinberg. Society for Biomaterials Annual Meeting, Denver, CO, April 2014

"FRESH 3D Prints (Freeform Reversible Embedding of Suspended Hydrogels)" **T Hinton.** A Hudson. A Feinberg. Biomedical Engineering Society Annual Meeting, San Antonio, TX, October 2014

"3D Printing Collagen I using Freeform Reversible Embedding of Suspended Hydrogels (FRESH)" **T Hinton.** A Hudson. A Lee. A Feinberg. RAPID Annual Meeting, Pittsburgh, PA, May 2017

Posters:

"3D Printing of Complex Scaffolds Using Freeform Reversible Embedding of Suspended Hydrogels" **T Hinton.** A Feinberg. TERMIS Annual Meeting, Boston, MA, September 2015

"FRESH 3D Printing: Freeform 3D printing of gels." **T Hinton.** A Hudson. A Feinberg. Technoport Annual Meeting, Trondheim, Norway, March 2016

"3D Printing of Complex Biological Scaffolds Using Soft Hydrogels" **T Hinton.** A Feinberg. Biomedical Engineering Society Annual Meeting, Tampa, FL, October 2015

"3D Printed Elastomer and Hydrogel in Fugitive Carbopol Support" **T Hinton.** A Lee. K Pusch. A Feinberg. World Biomaterials Congress, Montreal, Canada, May 2016.

"Scaffold Created by Freeform Reversible Embedding of Suspended Hydrogels" **T Hinton.** Q Jallerat. A Feinberg. McGowan Institute for Regenerative Medicine Annual Retreat, Nemacolin Woodlands, March 2015

"3D Bioprinting of Organ-Scale Type I Collagen Scaffolds" **T Hinton.** A Lee. A Hudson. A Feinberg. McGowan Institute for Regenerative Medicine Annual Retreat, Nemacolin Woodlands, March 2017

Appendix B : Print Settings Profiles for Slic3r

```
# generated by Slic3r 1.3.0-dev on
avoid_crossing_perimeters = 0
bed_shape = -125x-85,125x-85,125x85,-125x85
bed_temperature = 0
before_layer_gcode =
bottom_solid_layers = 0
bridge_acceleration = 0
bridge_fan_speed = 0
bridge_flow_ratio = 1
bridge_speed = 23
brim_connections_width = 0
brim_width = 0
complete_objects = 0
cooling = 1
default_acceleration = 0
disable_fan_first_layers = 3
dont_support_bridges = 1
duplicate_distance = 6
end_gcode = G92 Z0\nG1 Z10 F500\nG92 Z0\nM84     ; disable motors\n
external_fill_pattern = rectilinear
external_perimeter_extrusion_width = 0.08
external_perimeter_speed = 3
external_perimeters_first = 1
extra_perimeters = 1
extruder_clearance_height = 20
extruder_clearance_radius = 20
extruder_offset = 0x0,-58.5x0
extrusion_axis = E
extrusion_multiplier = 1,0.6
extrusion_width = 0.08
fan_always_on = 0
fan_below_layer_time = 60
filament_colour = #FFFFFF;#FFFFFF
filament_cost = 0,0
filament_density = 0,0
filament_diameter = 1.46,7.285
filament_max_volumetric_speed = 0,0
filament_notes = ;
filament_settings_id =
fill_angle = 45
fill_density = 0%
fill_gaps = 1
fill_pattern = rectilinear
first_layer_acceleration = 0
first_layer_bed_temperature = 0
```

first_layer_extrusion_width = 0.08
first_layer_height = 0.06
first_layer_speed = 100%
first_layer_temperature = 0,0
gap_fill_speed = 23
gcode_arcs = 0
gcode_comments = 0
gcode_flavor = reprap
has_heatbed = 1
infill_acceleration = 0
infill_every_layers = 1
infill_extruder = 1
infill_extrusion_width = 0.08
infill_first = 0
infill_only_where_needed = 0
infill_overlap = 55%
infill_speed = 23
interface_shells = 0
layer_gcode =
layer_height = 0.06
max_fan_speed = 0
max_print_speed = 20
max_volumetric_speed = 0
min_fan_speed = 0
min_print_speed = 3
min_skirt_length = 0
notes =
nozzle_diameter = 0.08,0.15
octoprint_apikey =
octoprint_host =
only_retract_when_crossing_perimeters = 1
ooze_prevention = 0
output_filename_format = [input_filename_base].gcode
overhangs = 0
perimeter_acceleration = 0
perimeter_extruder = 1
perimeter_extrusion_width = 0.08
perimeter_speed = 3
perimeters = 3
post_process =
pressure_advance = 0
print_settings_id =
printer_settings_id =
raft_layers = 0
resolution = 0
retract_before_travel = 1,1
retract_layer_change = 0,0

retract_length = 0.025,0.11
retract_length_toolchange = 0.05,0.075
retract_lift = 0.15,0.4
retract_lift_above = 0,0
retract_lift_below = 0,0
retract_restart_extra = 0,0
retract_restart_extra_toolchange = 0,0
retract_speed = 1,1
seam_position = nearest
serial_port =
serial_speed = 250000
skirt_distance = 6
skirt_height = 1
skirts = 0
slowdown_below_layer_time = 5
small_perimeter_speed = 3
solid_infill_below_area = 0.5
solid_infill_every_layers = 0
solid_infill_extruder = 1
solid_infill_extrusion_width = 0.08
solid_infill_speed = 20
spiral_vase = 0
standby_temperature_delta = -5
start_gcode = G92 X0 Y0 Z0 E0\nT0\nM302 P1\n
support_material = 0
support_material_angle = 0
support_material_contact_distance = 0.2
support_material_enforce_layers = 0
support_material_extruder = 1
support_material_extrusion_width = 0
support_material_interface_extruder = 1
support_material_interface_layers = 3
support_material_interface_spacing = 0
support_material_interface_speed = 100%
support_material_pattern = pillars
support_material_spacing = 2.5
support_material_speed = 23
support_material_threshold = 0
temperature = 0,0
thin_walls = 0
threads = 4
toolchange_gcode = T[next_extruder]\nM302 P1\nG91\nG1 Z20\nG90\n
top_infill_extrusion_width = 0.08
top_solid_infill_speed = 15
top_solid_layers = 0
travel_speed = 200
use_firmware_retraction = 0

use_relative_e_distances = 0
use_volumetric_e = 0
vibration_limit = 0
wipe = 0,0
xy_size_compensation = 0
z_offset = 0

Appendix C : CAD Files of Replistruders and Mounts

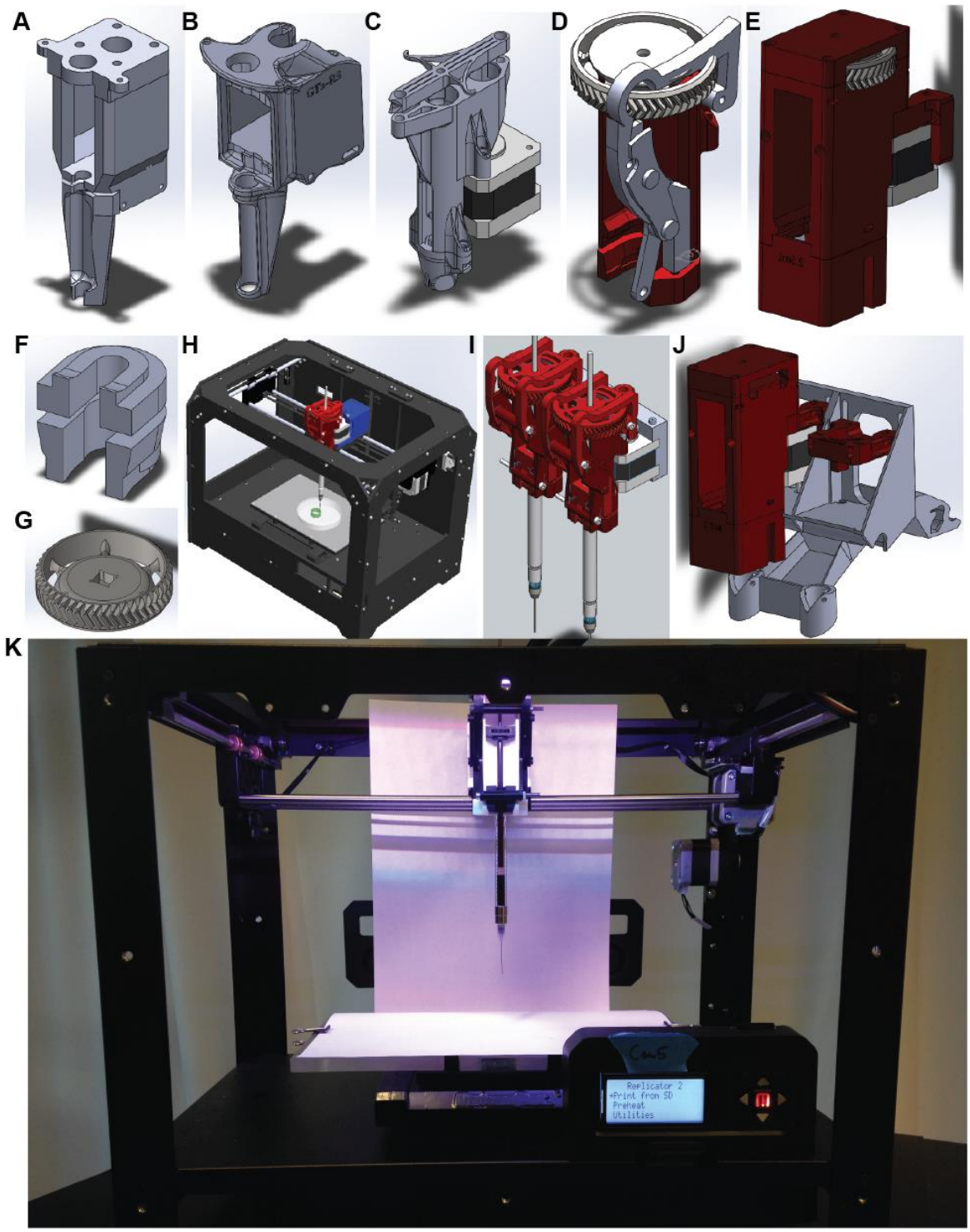

Figure C.1 CAD Files of Replistruders and Mounts (A) Replistruder 1.0 **(B)** Replistruder 2.0 **(C)** Replistruder 3.0 **(D)** Replistruder 4.0 **(E)** Replistruder 5.0 **(F)** Example syringe adapter used in Replistruder 4.0 **(G)** Herringbone gear used to actuate leadscrew in Replistruder 4.0 & 5.0 **(H)** Example of Makerbot Replicator 3D Printer with Replistruder 4.0 mounted on blue plastic printed mount **(I)** Example of dual Replistruder 4.0 mounted **(J)** Example of Replistruder 5.0 mounted on a dual Replistruder mount **(K)** Example of complete hardware system. Replistruder files and dimensions are available at **https://www.youmagine.com/tjhinton/designs**

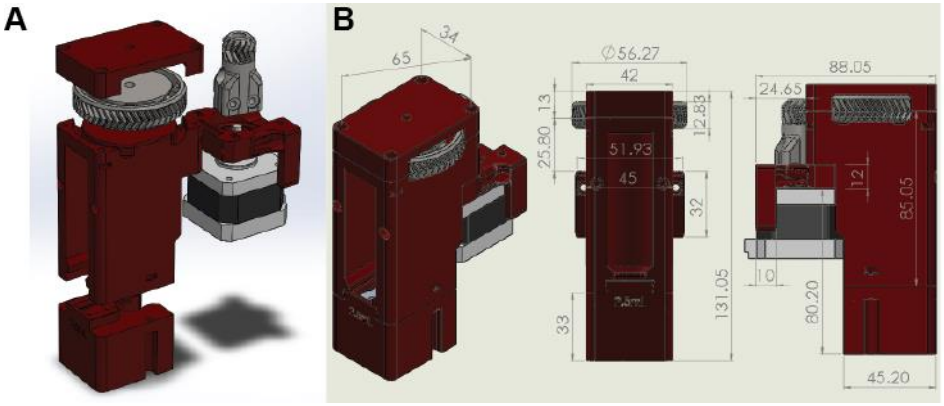

Figure C.2 CAD of Current Replistruder (A) Replistruder 5.0 exploded view **(B)** Replistruder 5.0 dimensions in mm